ENERGETIC OXYGEN AND SULFUR IONS IN THE JOVIAN MAGNETOSPHERE

Thesis by

Neil Gehrels

In Partial Fulfillment of the Requirements
for the Degree of
Doctor of Philosophy

California Institute of Technology

Pasadena, California

1982

(Submitted September 11, 1981)

Acknowledgements

It has been a great pleasure and learning experience to work with my faculty advisor, Dr. Edward Stone. This research project would not have been possible without his guidance and insight. Also, the scientific success of the Voyager mission and of the Cosmic Ray Subsystem are largely a result of Dr. Stone's leadership as the Voyager project scientist and as a CRS co-investigator.

Dr. Rochus Vogt has also had a great influence on my graduate career. I sincerely thank him for his guidance, particularly during my first years at Caltech. I greatly appreciate Dr. Vogt's leadership as the CRS principal investigator, and the opportunities he has provided for me to be involved in the laboratory calibrations of the instrument and in the analysis of the data obtained in the Jovian magnetosphere.

I am indebted to Dr. Jim Trainor, a CRS co-investigator at Goddard Space Flight Center, for his help in this research project, and for his friendship.

Many people at Goddard and Caltech have supported this investigation. Those at Goddard that I particularly wish to thank are Mo Beazley, Don Stilwell, and Dr. Al Schardt. The people at Caltech that I am especially grateful to are Bill Althouse, Randy Burrell, Dr. Dave Chenette, Dr. Alan Cummings, and Dr. Tom Garrard. I am indebted to Dr. Rick Cook for developing many of the analysis techniques and programs used in this thesis to determine the charges and energies of heavy ions detected by the Low Energy Telescopes. I thank Rick and Bill for showing me the ropes concerning accelerator calibrations and laboratory procedures. I am also grateful to Dr. Dick Mewaldt and Dr. Tom Prince for assistance at various stages of my graduate studies.

I greatly appreciate the friendship and help my fellow students in the Space Radiation Laboratory have provided. In particular, I would like to thank Jim Povlis, John Spalding, Keith Krombel, and Jonas Zmuidzinas.

Finally, I am deeply grateful to my parents Liedeke and Tom Gehrels for their encouragement through the years and for exposing me to the excitement of new ideas and travel, and to my wife, Ellen Williams, for making these the best years of my life.

This work was supported in part by NASA under NAGW-200.

Abstract

Observations of 1 to 20 MeV/nuc oxygen, sodium, and sulfur ions in the Jovian magnetosphere are reported. Measurements made by the Cosmic Ray Subsystem on Voyager 1 and 2 are used to calculate abundances and energy spectra in the region from 5 to 20 Jovian radii (R_J). The phase space density of the oxygen ions calculated from the spectra has a positive radial gradient between 6 and 17 R_J, indicating an inward diffusive flow. The diffusion coefficient upper limit at 9 R_J is $\sim 10^{-5}$ s^{-1}. This limit, combined with the analysis of Voyager plasma observations by Siscoe *et al.* [1981], implies an upper limit to the mass loading rate near Io of $\sim 10^{28}$ ions/s.

The energetic oxygen lifetime is within an order of magnitude of the strong pitch-angle diffusion lifetime in this region, with the largest total number of particles lost between 7.5 and 12.5 R_J. It is shown that the losses are not due to geometric absorption by Io, absorption by dust grains, or energy loss in the plasma of the inner magnetosphere, and it is therefore postulated that the primary loss mechanism is pitch-angle scattering into the loss cone.

The power delivered to the Jovian atmosphere by oxygen and sulfur ions with magnetic moments greater than 70 MeV/nuc-G ($E \gtrsim 0.3$ MeV/nuc at 10 R_J), scattered into the loss cone between 6 and 17 R_J, is $\sim 5 \times 10^{12}$ W; a power comparable to the $\sim 1.2 \times 10^{13}$ W required to produce the auroral emission observed by the ultraviolet spectrometer on Voyager [Broadfoot *et al.*, 1981]. The measured dependence of the input power on magnetic moment threshold indicates that additional power is contributed by oxygen and sulfur ions with magnetic moments less than 70 MeV/nuc-G. Since most of the particles are lost between 7.5 and 12.5 R_J, the latitudinal zone in which the most energy is deposited in the atmosphere is $\sim 67°$ to $\sim 71°$.

Table of Contents

Chapter 1

Introduction

Information provided by the Voyager spacecraft during their encounters with Jupiter in 1979 has changed our basic understanding of the particle composition and energetics of the Jovian magnetosphere. Oxygen and sulfur ions are now known to play important roles in all particle populations, from the plasma near Io to the MeV per nucleon (MeV/nuc) ions of the radiation belts.

The source of these ions is the Galilean satellite Io, whose volcanoes eject SO_2 onto its surface and into its atmosphere. Some of the gas that escapes from Io becomes ionized and is picked up by the rapidly rotating magnetic field of Jupiter ($9^h\ 55^m$ period). The energy produced by this acceleration process helps heat the torus of plasma that encircles Jupiter at the orbit of Io, producing intense ultraviolet radiation. As the plasma diffuses outward from the torus, it is pulled into a thin equatorial disk by the centrifugal forces acting on the heavy ions. Once the ions reach the outer magnetosphere, a mechanism that is not yet fully understood further accelerates some of the particles, producing a source of energetic oxygen and sulfur ions. These ions then diffuse away from the region, both outward along open field lines into the Jovian magnetotail producing an oxygen and sulfur wind, and back inward towards Io.

The inwardly diffusing ions gain energy as they move toward stronger magnetic fields, till they acquire energies in excess of an MeV per nucleon. Although they are small in number compared with the ions in the plasma, the total energy they bring into the inner magnetosphere is significant. This thesis concerns observations made of the energetic

oxygen and sulfur ions inside 20 Jovian radii (R_J; 1 $R_J = 7.14 \times 10^4$ km) by the cosmic ray instrument on Voyager 1 and 2. To put these observations in context, we will now briefly discuss the measurements made of the Jovian magnetosphere prior to the Voyager encounters, and describe in more detail the relevant results from Voyager.

In the 1950s Jupiter was discovered to be a source of nonthermal radio emission at both decametric [Burke and Franklin, 1955] and decimetric [Drake and Hvatum, 1959; Berge and Gulkis, 1976] wavelengths. It was found that the decametric radiation is modulated by Io's postion [Bigg, 1964], and postulated that the emission occurs in the ionosphere of Jupiter at the feet of the field lines that pass through the satellite. Equating the observed cutoff frequency of the emission with the local electron gyrofrequency led to an estimate of 7 G for the equatorial surface field strength of Jupiter [Goldreich and Lynden-Bell, 1969]. The decimetric radiation on the other hand was interpreted as synchrotron emission from electrons trapped in a dipolar magnetic field [Field, 1959]. Hence, even before any *in situ* measurements had been made of the Jovian magnetosphere, it was known that the planet had a strong magnetic field, containing trapped energetic electrons.

The first spacecraft to make direct measurements of the Jovian magnetosphere were Pioneer 10 and 11, which flew by Jupiter in 1973 and 1974 respectively. The instruments on the spacecraft include a magnetometer (two on Pioneer 11), a plasma analyzer, an ultraviolet photometer, and four particle detectors covering the energy range from ~100 keV to ~50 MeV for electrons and ions. The results from each instrument can be found in three collections of articles [*Science*, *183*, 301-324, 1974 (Pioneer 10); *Science*, *188*, 445-477, 1975 (Pioneer 11); *J. Geophys. Res.*, *79*, 3487-3694, 1974], with interpretations of these results

and reviews of Jovian research through 1975 contained in the book *Jupiter* [Gehrels, 1976]. In addition, there are four review articles on the Jovian magnetosphere based on Pioneer observations [Coroniti, 1975; Kennel and Coroniti, 1977; Schulz, 1979; Goertz and Thomsen, 1979].

The Pioneer results that pertain to the present discussion can be summarized as follows: The magnetic field is basically dipolar, with an equatorial strength of 4 G and an axis tilted 11° with respect to Jupiter's spin axis. However, in the region outside ~15 R_J, and particularly outside 30 R_J, the field was found to be distorted in the vicinity of the equatorial plane by an additional radial component. The distortion was postulated to be due to a warped current sheet caused by centrifugal forces acting on low energy magnetospheric plasma [Smith *et al.*, 1974; Van Allen *et al.*, 1974].

High intensities of energetic electrons and protons are trapped in the Jovian magnetosphere. Although the measured intensities above a given energy threshold generally increase toward smaller radial distances, the phase space densities of the electrons and protons at constant particle magnetic moment, M, ($M \propto p_\perp^2/B$) were found to decrease inward [McIlwain and Fillius, 1975; Baker and Goertz, 1976; Thomsen *et al.*, 1977]. The phase space density at constant M is the quantity that controls the magnitude and direction of particle diffusion (see e.g. Schulz and Lanzerotti [1974]), so that the observations imply an inward radial diffusion of energetic electrons and protons. Particles conserving their magnetic moments gain energy as they diffuse toward stronger magnetic fields. In the Earth's magnetosphere, for example, this process is the dominant mechanism for producing radiation belt particles [Schulz and Lanzerotti, 1974, and references therein]. However, in the Jovian magnetosphere the combination of large numbers of $\gtrsim$MeV electrons in

the outer magnetosphere [Goertz, 1978] and >50 MeV electrons ($M = 2 \times 10^4$ MeV/G at 3 R_J) in the inner magnetosphere [Fillius and McIlwain, 1974; Coroniti, 1975] requires an additional acceleration mechanism [Sentman *et al.*, 1975; Carbary 1976; Goertz, 1978 with numerical modelling by Borovsky *et al.*, 1981].

Loss mechanisms act on the energetic particles as they diffuse inward. Sharp decreases in electron and proton counting rates at the orbit of Europa, Io, and Amalthea and changes in the pitch-angle distributions across the orbit of Io indicated that some of the particles are absorbed by the Jovian moons [Thomsen, 1979]. There is also strong evidence that additional losses occur in the inner magnetosphere [Barbosa and Coroniti, 1976; Goertz *et al.*, 1979], most likely caused by pitch-angle scattering into the loss cone [Fillius *et al.*, 1976].

The only direct indication of the presence of heavy ions in the magnetosphere from the Pioneer encounters was from the University of Chicago fission cell detector, designed primarily to measure proton intensities but also sensitive to heavier nuclei. Signal characteristics in the inner magnetosphere were inconsistent with a proton dominated response, leading Simpson *et al.* [1974, 1975] to suggest that nuclei with nuclear charge, Z, greater than one were contributing to the counting rate. It has recently been shown using Voyager measurements that it is possible the fission cell was counting mostly oxygen and sulfur ions in the inner magnetosphere [Gehrels *et al.*., 1981]. Also, it is now known that the plasma analyzer on Pioneer 10 was detecting oxygen and sulfur ions near Io [Intriligator and Miller, 1981], although data from the instrument were initially analyzed assuming a proton plasma [Frank *et al.*, 1976].

Conclusive evidence of heavy ions and neutrals in the magnetosphere was provided prior to the Voyager encounters by ground-

based optical observations. In 1972, Brown [1974] observed emission from a cloud of neutral sodium atoms surrounding Io, and it was predicted that sodium plasma and energetic ions would be present in the magnetosphere [Eviatar *et al.*, 1976]. Emissions from singly ionized sulfur were discovered in 1975 [Kupo *et al.*, 1976], and since that time many other neutral and ionized species have been observed, including KI, OI, OII, OIII, SIII, and SIV (see review by Pilcher and Strobel [1981]). Although some consideration was given to the effect heavy ions would have on the magnetosphere [Hill and Michel, 1976], the significant role they play at all energies was not appreciated until the Voyager encounters.

Voyager 1 and 2 encountered the Jovian system in March and July of 1979. The instruments on the spacecraft include a magnetometer, a plasma analyzer, a plasma wave detector (10 Hz - 56 kHz), a planetary radio experiment (1.2 kHz - 41 MHz), an ultraviolet spectrometer, a low energy particle experiment (electrons 14 keV - 10 MeV, ions 30 keV - 150 MeV with elemental identification for $\gtrsim$200 keV), and a cosmic ray experiment (electrons 3$-$100 MeV, protons$-$iron $\sim$1$-\sim$20 MeV/nuc depending on element). There are several collections of articles concerning Voyager results and interpretations [*Science*, *204*, 945-1008, 1979 (Voyager 1); *Science*, *206*, 925-996, 1979 (Voyager 2); *Nature*, *280*, 725-806, 1979; *Geophys. Res. Lett.*, *7*, 1-68, 1980; *J. Geophys. Res.*, *86*, 1981]. The discussion of the results relevant to this thesis will be divided into the following topics: energetic particles, the Io plasma torus, the aurora, and the particle and energy budget.

Energetic particles – In the outer magnetosphere, the composition of ions with Z>2 between 7 and 14 MeV/nuc is similar to that of solar energetic particles [Vogt *et al.*, 1979a,b]. However, inside $\sim$12 R_J,

the composition is dominated by oxygen and sulfur. In the inner region the sulfur to oxygen ratio at constant energy per nucleon is between 0.6 and 0.8. A similar change in composition occurs for ions with energies in the range 0.60 to 1.15 MeV/nuc, except that, in the outer magnetosphere, sulfur is found to be approximately ten times more abundant relative to helium than in solar flare events [Krimigis *et al.*, 1979; Hamilton *et al.*, 1981]. As in the case of energetic electrons and protons observed by Pioneer, the phase space densities of the energetic oxygen ions [Vogt *et al.*, 1979b; Gehrels *et al.*, 1981] and protons [Armstrong *et al.*, 1981] detected by Voyager decrease toward smaller radial distances indicating inward diffusion. Beyond ~150 R_J in the magnetotail, ions with energies of ~100 keV stream outward in the anti-solar direction. This magnetospheric wind is rich in oxygen and sulfur, indicating that Io is the source of the particles.

Io plasma torus – The two most important Voyager discoveries concerning the magnetosphere were the intense Jovian aurora and the torus of hot plasma composed predominantly of oxygen and sulfur ions that encircles Jupiter at the orbit of Io. The source of the ions in the torus is Io's SO_2 atmosphere fed by volcanic activity on the satellite. The torus is divided into two parts, a cold (ion temperatures <1 eV) inner region inside 5.5 R_J with a scale height of ~0.2 R_J from the centrifugal equator, and a hot (ion temperature ~30 eV) outer region between 5.7 and ~7 R_J with a scale height of ~1 R_J [Bagenal and Sullivan, 1981]. (The orbital position of Io is 5.9 R_J.) The ground-based observation of S II lines [Kupo *et al.*, 1976] discussed earlier was of emission from the cold torus. The hot torus emits strongly in the ultraviolet, and was first observed by the ultraviolet instrument on Voyager 1 [Broadfoot *et al.*, 1979]. It has

subsequently been studied in the ultraviolet by Voyager 2 [Sandel *et al.*, 1979] and by the International Ultraviolet Explorer [Moos and Clarke, 1981]. The total rate of radiation energy-loss from the hot torus is estimated to be 3×10^{12} W [Broadfoot *et al.*, 1979; Shemansky, 1980a].

The charge density in the torus due to species with $A/Z^{*} \geq 8$, where A is the atomic mass number and Z^{*} is the ion charge state, (i.e., due to oxygen and sulfur in low ionization states) was directly measured by the plasma instrument [Bagenal and Sullivan, 1981], and was found to be equal within statistics to the electron density inferred from measurements of the electron plasma and upper hybrid frequencies by the planetary radio experiment [Warwick *et al.*, 1979]. The implication is that ions with $A/Z^{*} < 8$ (i.e. hydrogen) are a negligible component of the plasma. The charge density is $>10^{3}$ cm^{-3} between 5.7 and ~7 R_J and has several peaks in this region (see Figure 4.3a of this thesis). The density remains high ($\gtrsim 10^{2}$ cm^{-3}) out to ~9 R_J where the plasma disk begins to form. Plasma wave activity is enhanced inside ~20 R_J and is particularly intense in the region of the hot torus [Scarf *et al.*, 1979; Gurnett *et al.*, 1979; Scarf *et al.*, 1981].

Jovian aurora – Auroral emission (H Ly_{α} and H_2 Lyman and Werner bands) was observed in the Jovian atmosphere at high latitudes near both poles by the ultraviolet spectrometer [Broadfoot *et al.*, 1979; Sandel *et al.*, 1979]. The total power required to produce the observed luminosity is estimated to be 1.2×10^{13} W [Broadfoot *et al.*, 1981] and is presumably supplied by the precipitation of magnetospheric particles. The auroral zone is approximately 6000 km wide from north to south corresponding to ~5° in latitude, and is located between 60° and 80° latitude [Broadfoot *et al.*, 1981]. The location of the equatorward boundary of the zone is generally consistent with the magnetic projection

of the plasma torus onto the atmosphere [Broadfoot *et al.*, 1981], leading to the suggestion that electron precipitation from the torus drives the aurora [Sandel *et al.*, 1979; Thorne and Tsurutani, 1979]. There are, however, large differences in the positions of different aurorae and uncertainties in the positions of all of them due to the low polar viewing angle of the measurements, so that the magnetospheric location of the particle source is not constrained to the torus. Observations of optical auroral emission by the imaging instrument on Voyager [Smith *et al.*, 1979; Cook and Jones, 1981] may be useful in mapping the location and depth of the auroral activity, thereby indicating the energy and type of particle that is causing the emission at various depths and latitudes.

Particle and energy budget – There has been wide interest [Thorne and Tsurutani, 1979; Goertz, 1980; Eviatar and Siscoe, 1980; Shemansky, 1980b; Thorne, 1981; Sullivan and Siscoe, 1981] in determing the source of power that heats the torus ($\sim 3 \times 10^{12}$ W) and produces the auroral activity ($\sim 1.2 \times 10^{13}$ W). A possible energy source is the acceleration of newly ionized oxygen and sulfur ions near Io to corotation speeds by Jupiter's magnetic field. The ions acquire a longitudinal guiding-center velocity equal to the corotation velocity of the magnetic field at Io's orbit, and, assuming no local retardation of the corotation velocity near Io, a gyrospeed equal to the difference between Io's orbit velocity and the corotation velocity. This difference is 56 km/s, so that oxygen and sulfur ions acquire 262 and 524 eV respectively in the corotating frame. Therefore, the rate at which ions must be created and accelerated (the mass loading rate) in order to heat the torus is $\sim 5 \times 10^{28}$ ions/s (assuming two oxygen ions for every sulfur ion due to dissociation of SO_2) and to produce the auroral power is $\sim 2 \times 10^{29}$ ions/s. However, Shemansky [1980b] has shown that excitation of ions during the

ionization process would lead to ultraviolet emissions of specific wavelengths from the ionization region, and that no such emissions were detected in the vicinity of Io. The upper limit to the mass loading rate near Io consistent with no oberved radiation is $\sim 10^{27}$ ions/s. The measurement does not rule out the possibility that ionization occurs in other parts of the torus, away from Io, but there is another constraint that limits this case.

The observed abundances of the different ionization states of sulfur in the hot torus during Voyager 1 encounter require that the ion residence time in the torus is on the order of 100 days [Shemansky, 1980b]. The total number of ions in the hot torus is $\sim 5 \times 10^{34}$ [Sullivan and Siscoe, 1981], so that this analysis gives a mass loading rate on the order of $\sim 6 \times 10^{27}$ ions/s. Although this estimate is not accurate to a factor of two or probably even four, it does suggest that the mass loading rate is no lower than $\sim 10^{27}$ ions/s, and no higher than a few times 10^{28} ions/s. The mass loading rate of 5×10^{28} ions/s required to heat the torus is therefore somewhat high, and the 2×10^{29} ions/s required to power the aurora is certainly unrealistic. This problem is often referred to as the energy crisis of the inner magnetosphere.

A possible solution to the auroral power requirement is to precipitate inwardly diffusing energetic protons [Goertz, 1980] or heavy ions [Thorne, 1981] instead of torus electrons. In this case the auroral energy is supplied by the process that accelerates the energetic particles. Thorne [1981] also points out that some of the secondary electrons created in the atmosphere by heavy ion precipitation could escape back into the magnetosphere and help heat the torus. One of the goals of the present analysis is to determine the amount of power delivered to the Jovian atmosphere by energetic oxygen and sulfur ions lost from the

inner magnetosphere.

This thesis is based on a study of energetic Z>2 ions in the Jovian magnetosphere. In previous reports [Vogt *et al.*, 1979a,b; Gehrels *et al.*, 1981], the elemental composition of the energetic ions, the oxygen energy spectrum, and the phase space density profile between 6 and 17 R_J for 680 MeV/nuc-G oxygen ions were determined. In this report oxygen, sulfur, and sodium energy spectra are obtained, and the phase space density profile is calculated with improved radial resolution for several oxygen magnetic moments. These profiles are used to specify limits on the diffusion coefficient in the inner magnetosphere. The inward diffusive flow rate of particles and energy is then determined and estimates made of the power delivered by the oxygen and sulfur ions to the Jovian atmosphere.

Chapter 2

The Experiment and Data Analysis

2.1 Encounters with Jupiter

The data used in this study were obtained with the Low Energy Telescopes (LETs) of the Cosmic Ray Subsystem (CRS) on board Voyager 1 and 2 during their encounters with Jupiter in 1979. Trajectory and timing information for both encounters are given elsewhere [*Science 204*, 945-1008, 1979; *Science 206*, 925-996, 1979] and will be only summarized here. Figures 2.1 and 2.2 show the spacecraft trajectories with respect to the Jovian magnetosphere and satellites. Typical positions of the bow shock and magnetopause boundaries (see Appendix A for definitions of magnetospheric terms) that delimit the magnetosphere are indicated in Figure 2.1. These positions can, however, vary by as much as ± 30 R_J on a time scale of hours.

From February 28 through March 2, 1979, Voyager 1 crossed the bow shock and magnetopause a number of times as these boundaries convected back and forth past the spacecraft (exact crossing times are given by Lepping *et al.* [1980]). The final entry into the magnetosphere was at 0227 universal time (UT, spacecraft event time) on March 3 at a zenocentric distance of 47 R_J. Closest approach to Jupiter was at 1205 UT on March 5 (day 64 of 1979) at a distance of 4.9 R_J, just inside the orbit of Io (Figure 2.2a). With a periapsis near the orbit of Io, a maximum amount of time was spent observing the satellite and its interaction with the magnetosphere. The spacecraft flew almost directly underneath Io on the outbound crossing of the orbit, allowing the current system in the magnetic flux tube that connects it and Jupiter to be studied. Voyager 1 crossed the magnetopause outbound several times on

Figure 2.1

Voyager 1 (V1) and 2 (V2) trajectories through the Jovian magnetosphere as viewed from the north. Jupiter is at the origin of the coordinate system. Typical bow shock and magnetopause positions are shown.

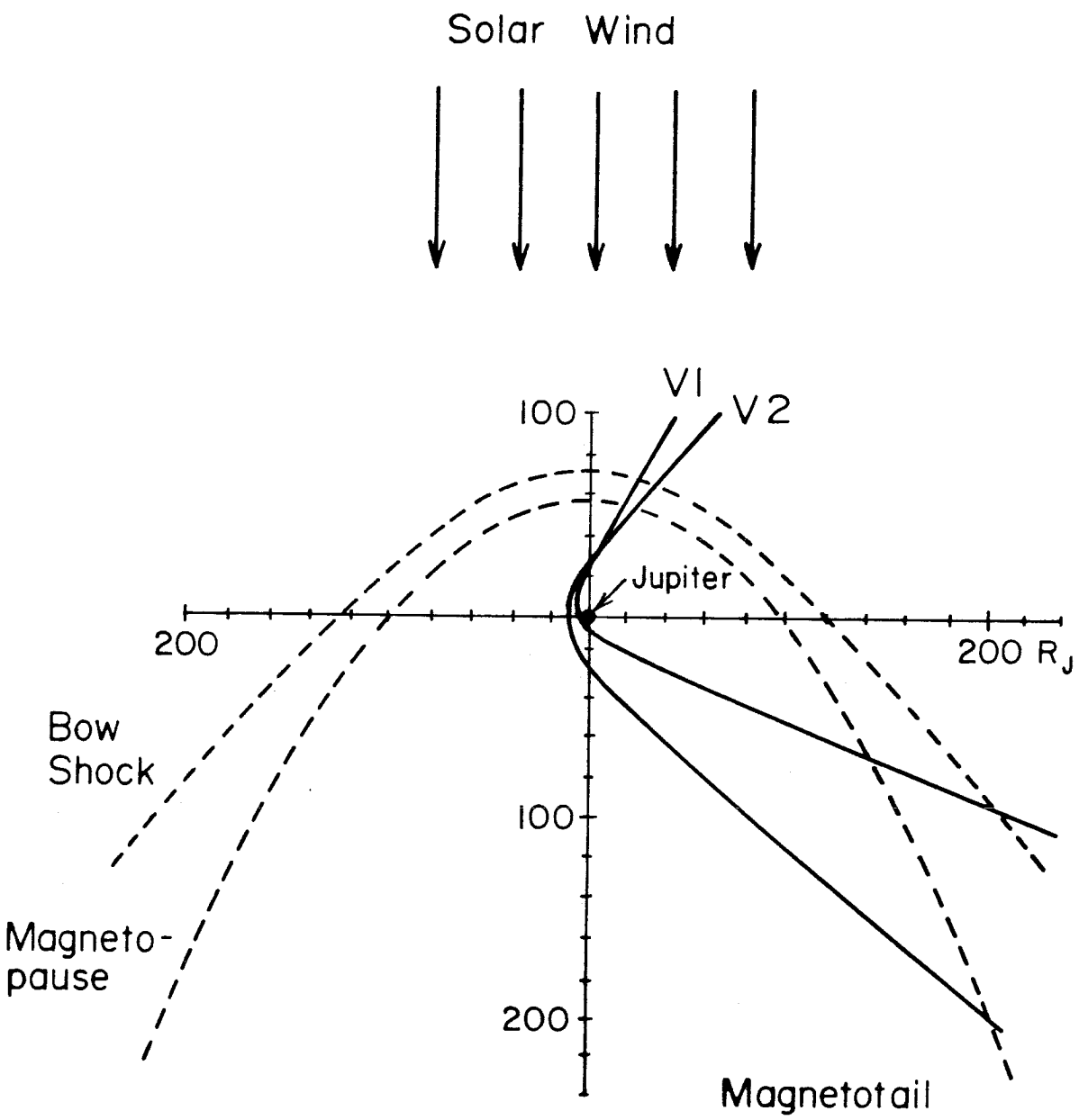
Solar Wind
V1
V2
100
Jupiter
200
200 R_J
Bow
Shock
100
Magneto-
pause
200
Magnetotail

Figure 2.2

Trajectories of a) Voyager 1 and b) Voyager 2 with respect to the orbits of Jupiter's moons, as viewed from the north.

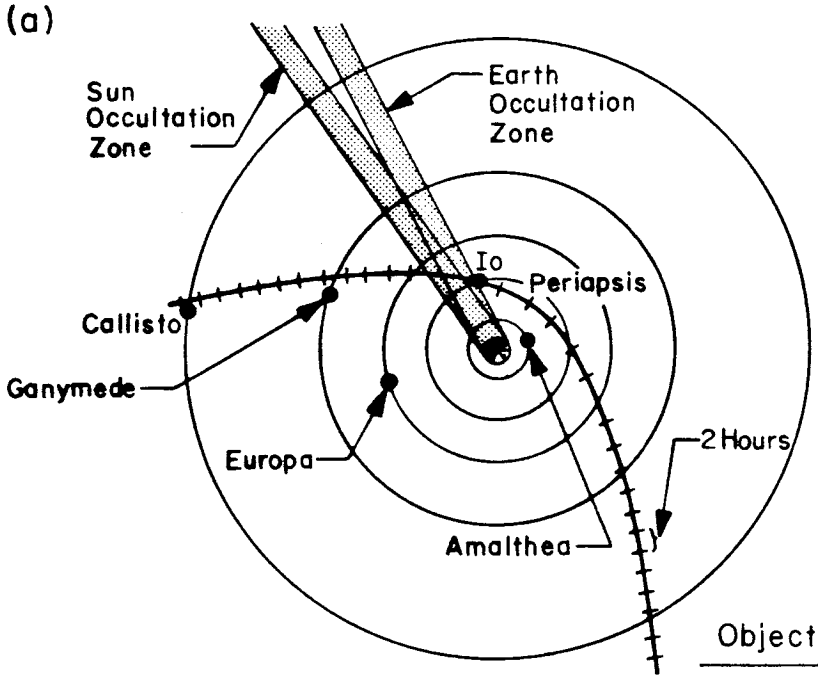

Object	Mean Distance from Jupiter (R_J)
The Ring	~1.8
Amalthea	2.5
Io	5.9
Europa	9.4
Ganymede	15.0
Callisto	26.3

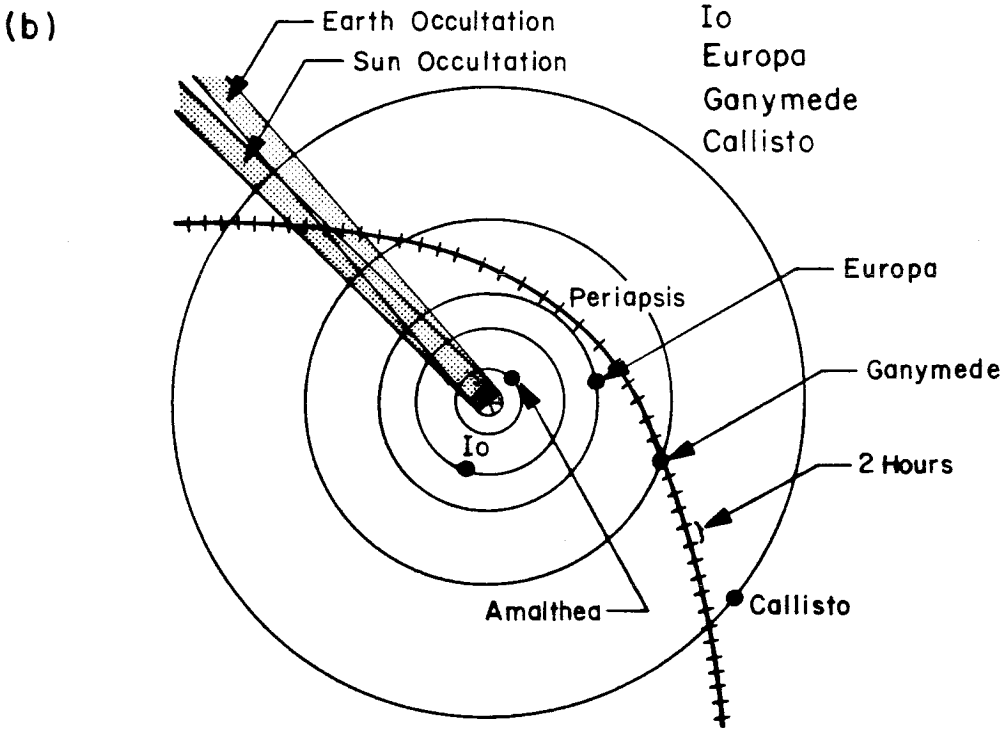

March 15 at a distance of ~160 R_J.

The Voyager 2 bow shock and magnetopause crossings occurred between July 2 and 5, 1979, with final entry into the magnetosphere at 1840 UT on July 5 at a distance of 62 R_J. Closest approach was at 2229 UT on July 9 (day 190) at a distance of 10.1 R_J, just outside the orbit of Europa (Figure 2.2b). The Voyager 2 outbound trajectory was the deepest penetration of the Jovian magnetotail of any spacecraft to date, with the final magnetopause crossing occurring at a distance of ~280 R_J on August 3.

Both spacecraft had inbound and outbound trajectories that were within ~6° latitude of Jupiter's spin equatorial plane. Therefore, since the planet's magnetic dipole axis is tilted 10.8° with respect to its spin axis, the spacecraft passed through the magnetic equatorial plane twice per planetary rotation period of $9^h\ 55^m$ (expect beyond ~80 R_J in the magnetotail where the magnetic equatorial plane is bent toward the spin equatorial plane). This variation in spacecraft magnetic latitude caused a periodic modulation in the measured particle intensities due to the fact that the intensities of trapped energetic particles are organized about the magnetic equatorial plane, which is their bounce symmetry surface.

2.2 The Instrument

This section describes the features of the LETs that are important for the present analysis. General descriptions of the CRS instrument and electronics are given by Stone *et al.* [1977] and Stilwell *et al.* [1979]. Detailed information about the CRS instrument such as discriminator settings, data formats, and rate specifications are in the Voyager Science Requirements Document [Garrard, 1976].

The LET system provides measurements of particle intensities, energies, and elemental composition in the MeV/nucleon energy range. It consists of four nominally identical particle telescopes, LET A, B, C, and D, oriented to allow detection of anisotropies in the particle arrival directions. During the Voyager 1 and 2 Jovian encounters, LET A and C were turned off inside ~20 R_J to reduce the noise level at the input of the pulse-height analyzers shared with LET B and D respectively. Therefore, since the analysis that follows concentrates on the region inside 20 R_J, only data from LET B and D will be used.

A schematic diagram of a LET is shown in Figure 2.3. The telescope is a stack of four solid-state silicon surface-barrier detectors (L1, L2, L3, and L4), each of which is a thin circular disk of ~1 cm radius. A 3 μm thick aluminum window provides light shielding for L1. When adequate bias is applied between the thin (~40 $\mu g/cm^2$) metal contacts on each surface of the detector, the silicon becomes fully depleted.

A charged particle penetrating or stopping in the detector creates electron-hole pairs along its path that collect on the contacts, producing a small current pulse that is fed into a charge sensitive preamplifier and a shaping postamplifier. The height of the resulting output pulse is proportional to the particle energy loss in the detector. The signal from each detector amplifier is then compared with a threshold level in a discriminator circuit, and, if a specified coincidence requirement between the four detectors is met, the signals from L1, L2, and L3 are pulse-height analyzed. Coincidence requirements are specified by sending commands to the instrument.

The data used in the present study were obtained with Voyager 1 in the L1·L2 command state in which a particle is required to exceed the L1 and L2 discriminator thresholds but no requirement is made on L3,

Figure 2.3

Schematic diagram of a LET. The detector areas and thicknesses that are given are nominal values. Laboratory measurements of the flight detector thicknesses and active areas [Gehrels and Cummings, 1980] were used in the analysis.

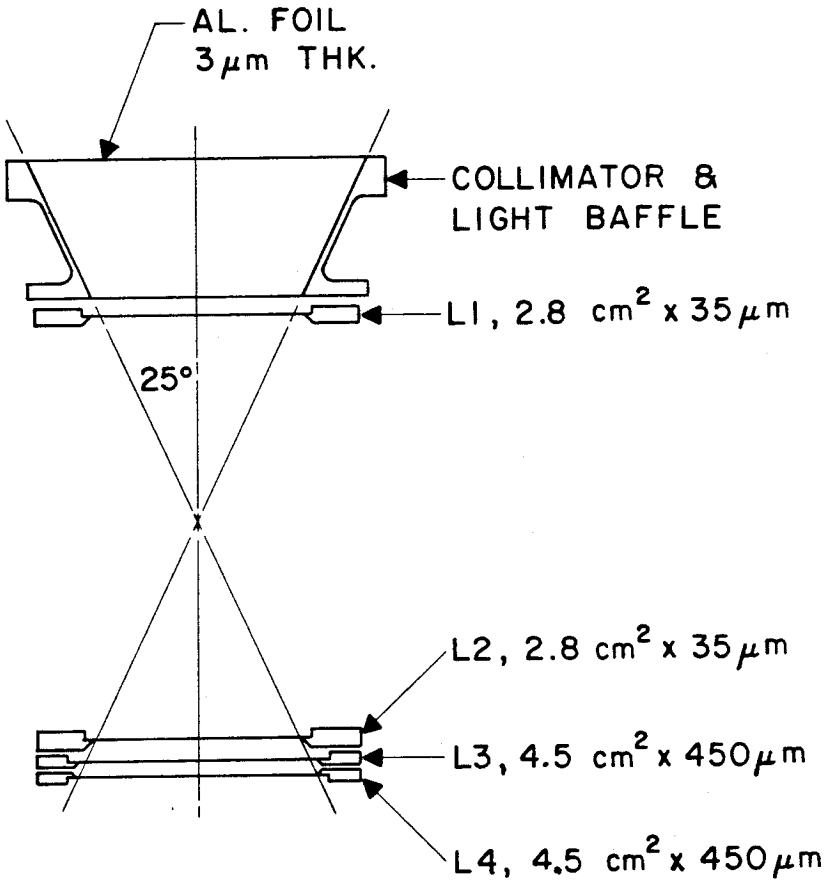

LOW ENERGY TELESCOPE (LET)

and with Voyager 2 in the L1·L2·L3 command state in which a particle is required to exceed the discriminator thresholds in L1, L2, and L3. During the interplanetary cruise parts of the mission, L4 is used in anticoincidence in these two command states to eliminate penetrating particles. However, L4 was turned off inside ~20 R_J in the Jovian magnetosphere to minimize accidental event rejection due to the high radiation environment. The LET geometry factors for pulse-height analyzed events (PHA events), and the energy ranges over which oxygen and sulfur nuclei can be measured are listed in Table 2.1 for both command states.

In addition to pulse heights, the instrument also measures the rates at which discriminator threshold levels are exceeded and coincidence conditions are met. The following rates are used in this study:

1) detector singles rates. The counting rates of the L1, L2, and L3 discriminators; called R_1, R_2, and R_3.

2) Z>2 singles rate. The counting rate of the Z>2 discriminator. The Z>2 discriminator is triggered when a particle has energy losses E1, E2, and E3 in L1, L2, and L3 such that $E1 + 0.42\,E2 + 0.20\,E3 > 9.6\text{MeV}$. It is called the Z>2 discriminator because neither protons nor alpha particles within the acceptance cone of the telescope can satisfy this condition. Note that the Z>2 rate does not require energy loss in all three detectors (i.e. it is not a coincidence rate), and therefore, since the geometry factor defined by the collimator and L1 (4.6 cm^2 sr) is much larger than that defined by the collimator and L2 or L3 (0.5 cm^2 sr), it is primarily the rate of Z>2 nuclei losing more than 9.6 MeV in L1. The geometry factor and oxygen and sulfur energy ranges for the Z>2 rate are listed in Table 2.1.

Table 2.1

Nominal LET Parameters

	Command State	Geometry * Factor (cm^2-sr)	Element	Energy † Range (MeV/nuc)
event analysis	L1•L2	0.44	oxygen	3.6 - ∿23. ¶
			sulfur	4.5 - ∿50.
	L1•L2•L3	0.44	oxygen	6.0 - ∿23.
			sulfur	7.5 - ∿50.
Z>2 rate	-	4.6	oxygen	∿1.1 - 25. §
			sulfur	∿0.9 - 120.

* Each of four telescopes.

† Energy loss in the 3 μm aluminum window has been added to the detector and Z>2 thresholds to give the incident energy of the particle.

¶ Event analysis includes events that penetrate L3 (L4 off). The maximum energies are those at which the track foldback on an E2 vs E3 plot crosses the oxygen track for sulfur and the carbon track for oxygen.

§ The dependence of the low energy threshold of the Z>2 rate on rate and pulse height is given in Table B.2. The oxygen thresholds used in the analysis are listed in Table 3.2.

3) the Z>2 coincidence rate. The counting rate of particles exceeding the discriminator thresholds in L1 and L2 (L1·L2 command state) or in L1, L2, and L3 (L1·L2·L3 command state), and in addition exceeding the Z>2 threshold; called the LZ3 rate. The conditions for this rate are identical to those for pulse-height analysis. During the Jupiter encounters, the spacecraft data rate limited the rate at which Z>2 PHA events were received to approximately one per second (per LET). Since this was a small fraction of the incident rate of these events, the LZ3 rate was used to renormalize the intensities.

2.3 The Analysis Technique

The technique for converting rate and pulse height information into elemental abundances, energy spectra, and absolute intensities will now be discussed.

2.3.1 Element Identification and Energy Determination

A particle entering a LET is stripped of most of its electrons in the 3 μm aluminum window, so that no information is available about its charge state prior to entering the telescope. The LETs employ a $\Delta E - E$ technique to identify the nuclear charge of particles that penetrate L1 and stop in L2 or L3. This technique and its application to the LETs is discussed in detail by Cook [1980], and will be only briefly summarized here.

The energy loss, ΔE, of a nucleus with charge Z and velocity v in L1 or L2 is roughly proportional to Z^2/v^2. Therefore, by measuring a particle's energy loss in L1 or L2 and its residual kinetic energy, E, as it stops in subsequent detectors, its charge can be determined. Figure 2.4a

Figure 2.4

Energy-loss plots of Z>2 PHA events. The energy losses were calculated from the pulse heights returned by the instrument using laboratory calibration data [Povlis, 1980] and gain correction factors obtained from flight data [Cook, 1980].

a) E2 vs E3 for all Voyager 1 LET D events from day 64/0936 to 64/1405 UT (the 4.9 and 5.3 R_J regions in Table 3.1). The oxygen, sodium, and sulfur tracks are indicated. Events in the bottom left-hand corner have not been plotted.

b) E2 vs E3 for all Voyager 2 LET B events from 190/1200 to 191/0600 UT. Events in the bottom left-hand corner have not been plotted.

c) E1 vs E2+E3 for the same events shown in figure a. Events along the E1 axis have not been plotted.

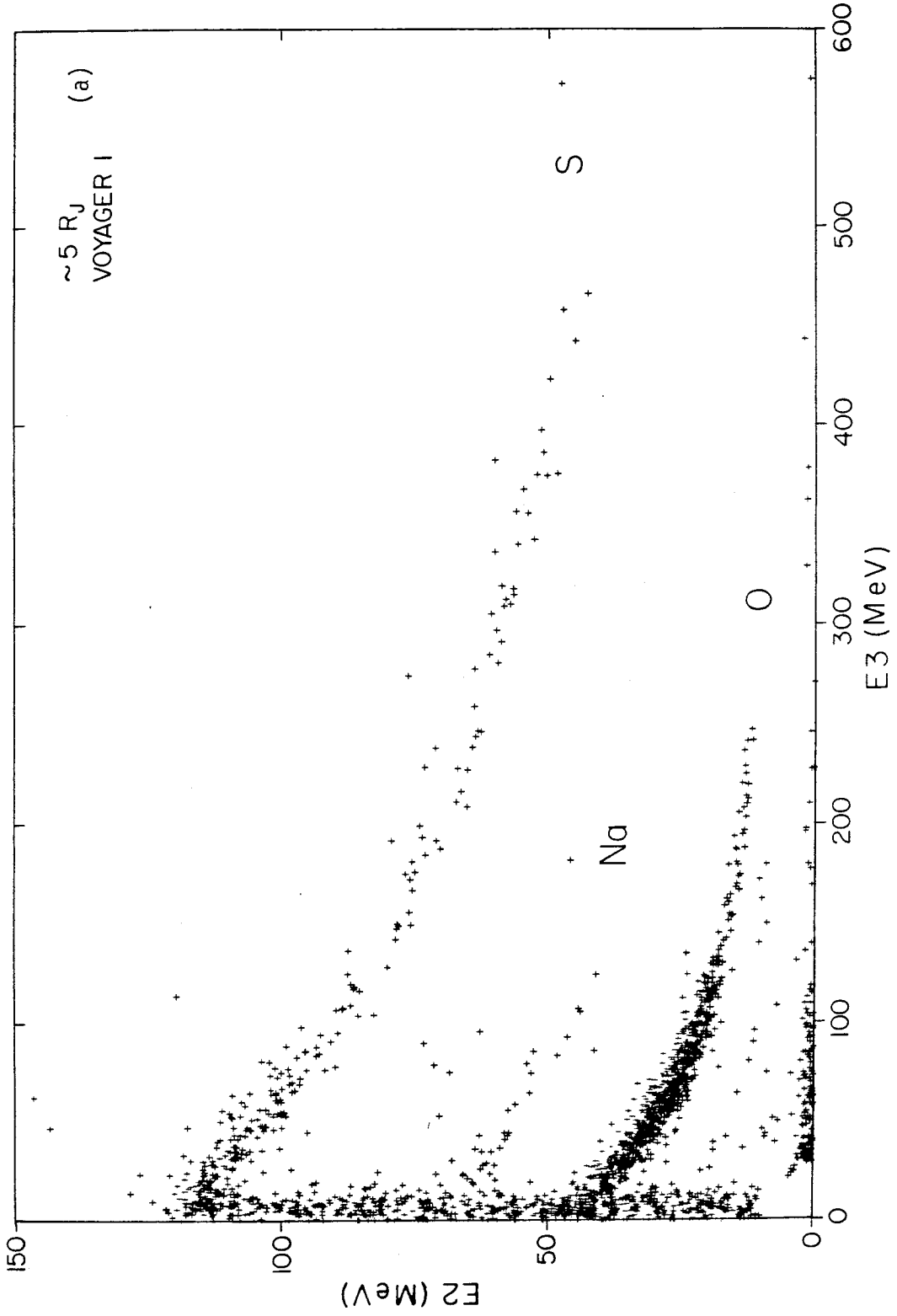
~5 R_J
VOYAGER 1
(a)
S
Na
O
E2 (MeV)
E3 (MeV)
150
100
50
0
0
100
200
300
400
500
600

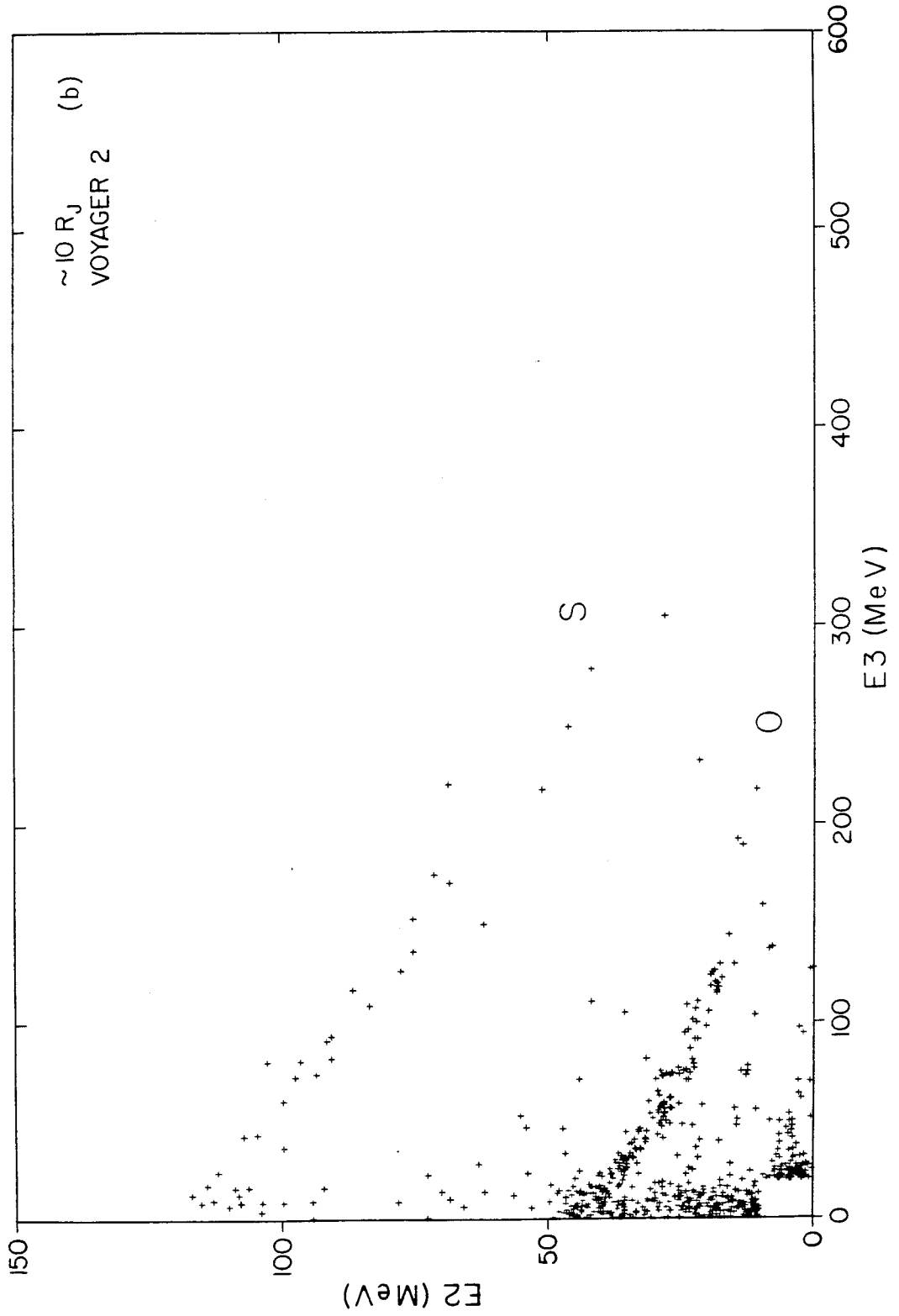
~10 R_J
VOYAGER 2
(b)
S
O
E2 (MeV)
E3 (MeV)
0
50
100
150
0
100
200
300
400
500
600

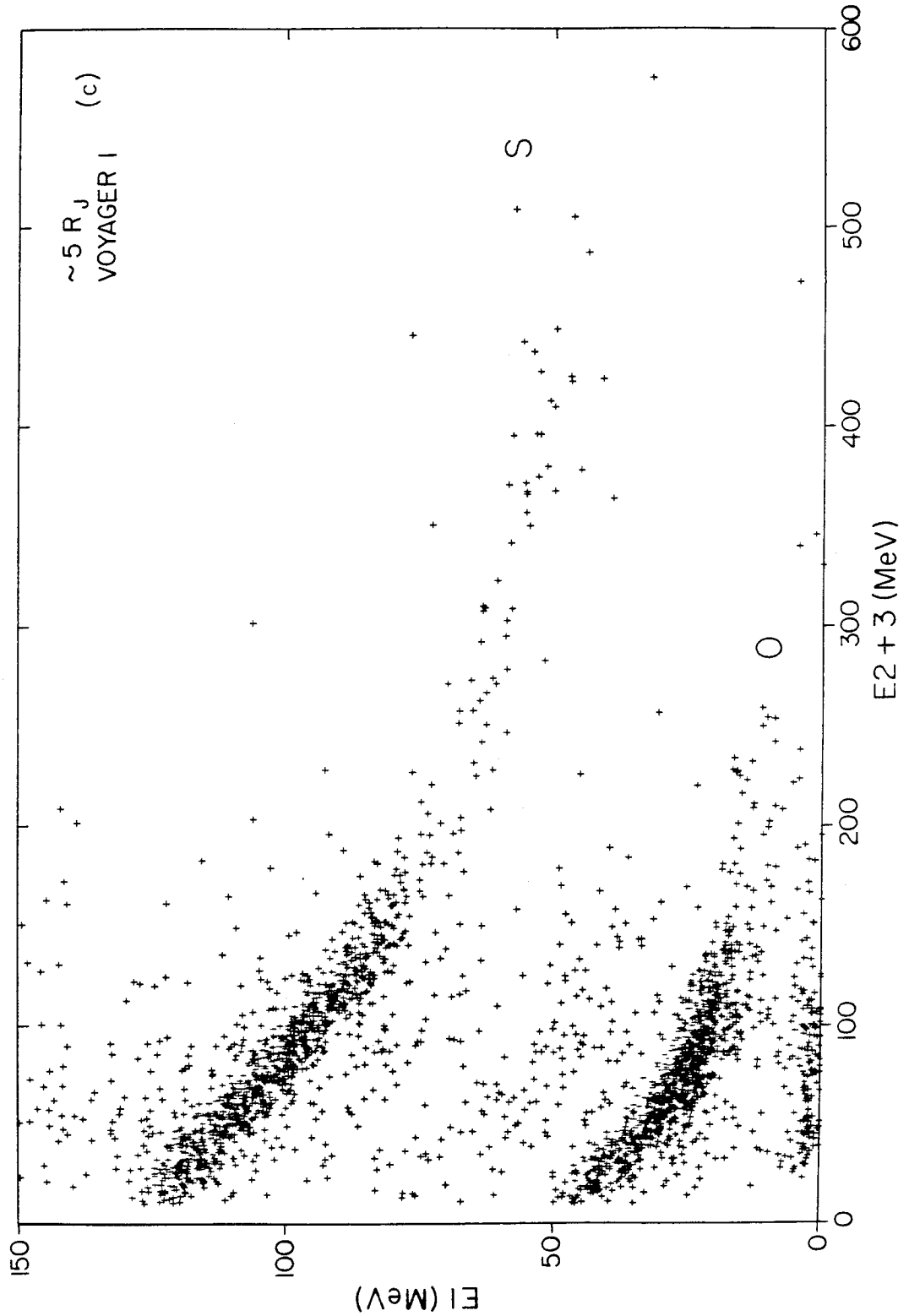
~5 R_J
VOYAGER 1
(c)
S
O
E1 (MeV)
E2 + 3 (MeV)
0
50
100
150
0
100
200
300
400
500
600

shows the L2 and L3 energy losses of Z>2 PHA events detected by LET D near Io. In this case, E2 is the ΔE measurement and E3 is the residual energy. Particles stopping in L3 are seen to form clear tracks corresponding to oxygen, sodium, and sulfur nuclei. The events along the left-hand edge of the figure are due primarily to oxygen and sulfur events stopping in L2 that were in accidental coincidence with a Z=1 particle (a proton or several electrons) that exceeded the L3 discriminator threshold. The charge of these events can be determined using their L1 and L2 pulse heights. There are a substantial number of events in the bottom left-hand corner of the figure that have not been plotted. These corner events are due primarily to oxygen and sulfur nuclei stopping in or penetrating L1 (exceeding the Z>2 threshold), but not hitting L2 or L3. The small pulse heights in L2 and L3 are due to Z=1 particles in accidental coincidence with the heavy event. Figure 2.4b is a similar plot obtained near Voyager 2 closest approach (~10 R_J) by LET B.

The width of the oxygen track in Figure 2.4a is $\sigma_z = 0.2$ charge units, compared with the LET charge resolution of $\sigma_z = 0.1$ charge units (for Z near 8) measured during solar energetic particle events in the interplanetary cruise part of the mission [Cook, 1980]. The poorer charge resolution obtained in the Jovian magnetosphere is due to energy-loss broadening caused by Z=1 particles in coincidence with the heavy ion.

If the heavy ion rate itself becomes large enough in a detector that a significant number of the events are in coincidence with each other, a much larger broadening occurs. In L2 and L3 the spectrum and geometry factor combine to keep the oxygen and sulfur counting rate small ($\lesssim 10^3\ s^{-1}$), so that this effect is not a problem in these detectors. However, as discussed in Appendix B, the oxygen and sulfur rate in L1

(basically the Z>2 rate) is high enough in some regions to cause substantial broadening; for instance, near Io ~30% of the oxygen and sulfur events are in coincidence with another heavy ion and are consequently displaced from their respective tracks. The displaced events form a background of events above the oxygen and sulfur tracks. This background can be clearly seen in Figure 2.4c, which shows the energy losses E1 and E2+E3 for the same data as that shown in Figure 2.4a. Fortunately, this problem can be avoided for events stopping in L3 since element identification can be made using only E2 and E3. Almost all analysis in this study is based on such three-detector events. Only near Io was the analysis extended to lower energies using the events stopping in L2 (two-detector events). For this case a pileup correction factor was applied to the two-detector portion of the spectrum, as described in Appendix B.

For the three-detector events, the particle energy prior to entering the telescope was calculated from E2 and E3 using laboratory measurements of the L1 thickness [Gehrels and Cummings, 1980] and the empirical range-energy relationship that Cook [1980] developed for the LETs. The telescope window thickness was assumed to be 3 μm, as specified by the manufacturer. For the two-detector events, the total energy is the sum of E1 and E2, plus a small term due to energy loss in the window.

2.3.2 Intensity Determinations

There are two sources of information from the LETS concerning the absolute intensities of Z>2 particles; the Z>2 rate and the combination of PHA events and the LZ3 rate. As discussed in the instrument section, the

Z>2 rate is primarily the counting rate of nuclei with nuclear charge greater than two, losing more than 9.6 MeV in L1. Therefore, if the fraction of rate counts due to a certain element can be determined, the Z>2 rate can be used as an integral intensity measurement of that element. (The rate is not strictly speaking an integral measurement since particles above a certain energy are not counted, but spectra of interest in this study are all soft enough in the vicinity of the upper energy limit that the rate is effectively an integral.)

The problem of determining this fraction is made easier in the inner Jovian magnetosphere by the fact that, in the MeV/nuc energy range, oxygen and sulfur are much more abundant than other species. Near Io, the pulse-height histogram of L1, shown in Figure 2.5a, reveals two separate peaks due to penetrating oxygen and sulfur nuclei. The events shown in this figure all have small L2 pulse heights caused, in most cases, by a Z=1 particle in accidental coincidence with the heavy ion. The histogram therefore represents a sample of the Z>2 rate and can be used to directly measure the oxygen and sulfur fractions in the rate. In other regions of the magnetosphere, pulse-height histograms of L1 did not have separate peaks as can be seen in the example from LET B near Voyager 2 closest approach shown in Figure 2.5b. In these regions the oxygen and sulfur fractions of the Z>2 rate were estimated from higher energy spectral data.

The effective threshold level of the Z>2 discriminator can increase in high radiation environments due to baseline shifts at the outputs of the detector amplifiers. As described in Appendix B, this effect has been measured in the laboratory and is taken into account in all analysis. Also measured in the laboratory and described in the appendix is the livetime correction for the Z>2 rate.

Figure 2.5

Histograms of the L1 energy loss for Z>2 PHA events. The time periods and telescopes are the same as for a) Figure 2.4a and b) Figure 2.4b. Only events with E2 and E3 less than 15 MeV have been plotted so that these events correspond to those in the suppressed bottom left-hand corners in the previous figures. The triangles on the E1 axis indicate the Z>2 discriminator threshold level for L1 during the time periods shown.

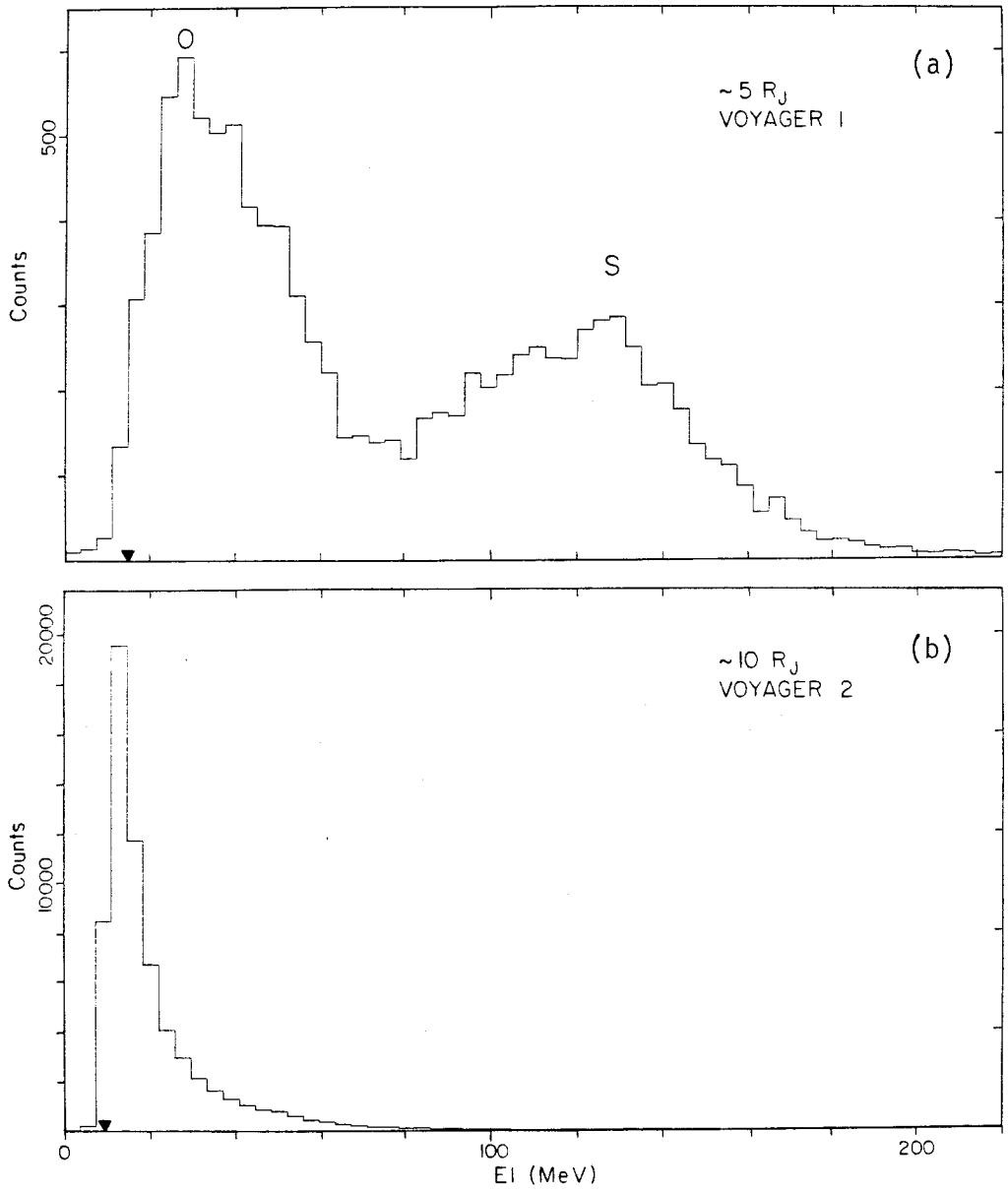
O
S
(a)
~5 R_J
VOYAGER 1
500
Counts
(b)
~10 R_J
VOYAGER 2
20000
10000
Counts
0
100
200
EI (MeV)

The PHA events are in general easier to convert into intensities than the Z>2 rate since the nuclear charge is measured for each event. Also, the energy of each event is measured, so that differential as well as integral intensities can be determined. As discussed in the instrument section (2.2), the LZ3 rate is used to convert the PHA event rate into intensities. The formula for calculating the integral intensity of species k with energy greater than E′ is

$$J_k(E>E') = \frac{n_{pha-k}(E>E')}{n_{pha-tot}\ \ 0.44\ cm^2-sr} \cdot LZ3 \qquad (2.1)$$

where $n_{pha-k}(E>E')$ is the number of PHA events of species k with energy greater than E′ measured in a given time interval, $n_{pha-tot}$ is the total number of PHA events in that time interval, and 0.44 cm^2–sr is the geometry factor for event analysis. The LZ3 rate used in equation (2.1) includes a livetime correction factor that was determined using laboratory measurements (Appendix B).

Chapter 3

Observations

Energetic particle observations made by the CRS instruments in the Jovian magnetosphere are summarized by Vogt *et al.* [1979a,b] and Schardt *et al.* [1981]. This study deals primarily with observations of Z>2 ions inside ~20 R_J. The emphasis will be on oxygen ions, since oxygen was the only species observed with adequate statistics to allow a detailed investigation of the radial dependence of its intensity and energy spectrum. The abundances and spectra of carbon, sodium, and sulfur will, however, also be presented where statistics allow.

3.1 Intensity Profiles

Figure 3.1 shows the measured Z>2 intensities for Voyagers 1 and 2 inside ~20 R_J. The Z>2 intensity is determined from the livetime corrected Z>2 rate and its geometry factor (4.6 cm^2 sr), and therefore, inside 20 R_J, is primarily the intensity of oxygen ions with energies greater than ~1.1 MeV/nuc and sulfur ions with energies greater than ~0.9 MeV/nuc (Table 2.1).

There is a pronounced decrease in the Z>2 intensity inside ~7 R_J on Voyager 1 due to particle losses in the vicinity of Io. The minima that occur in the intensities at 5.6 R_J inbound (day 64 0934 UT) and 5.4 R_J outbound (day 64 1406 UT) indicate an abrupt inner edge of the lossy region. Their location can therefore be compared with that of Io and that of plasma and electromagnetic wave features in the region to determine what the likely loss mechanism is. The electron density in the Io torus [Warwick *et al.*, 1979; Bagenal and Sullivan, 1981] decreases

Figure 3.1

The Z>2 intensities measured by LET B near closest approach for a) Voyager 1 and b) Voyager 2. The Z>2 intensity is primarily the intensity of oxygen and sulfur ions with energies greater than ~1.1 and ~0.9 MeV/nuc respectively. Oxygen spectra have been calculated for regions indicated in the figure. The number associated with each region is the spacecraft−dipole center distance at the time the spacecraft crossed the magnetic equatorial plane in that region.

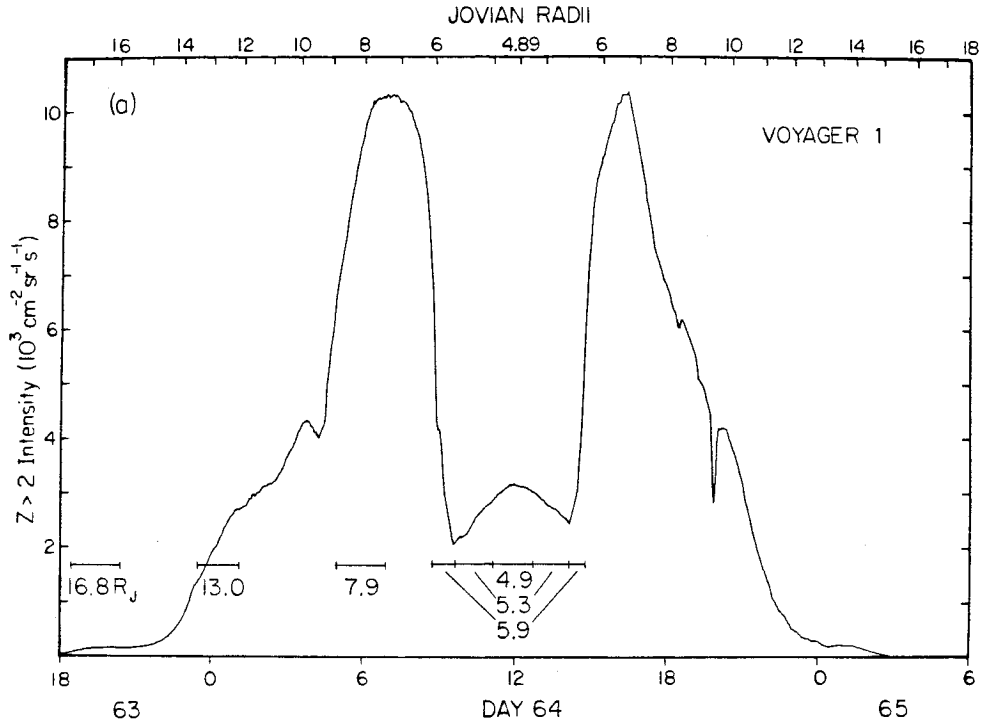
JOVIAN RADII
16 14 12 10 8 6 4.89 6 8 10 12 14 16 18
(a)
VOYAGER 1
Z > 2 Intensity (10^3 cm^{-2} sr^{-1} s^{-1})
16.8 R_J
13.0
7.9
4.9
5.3
5.9
18 0 6 12 18 0 6
63 DAY 64 65

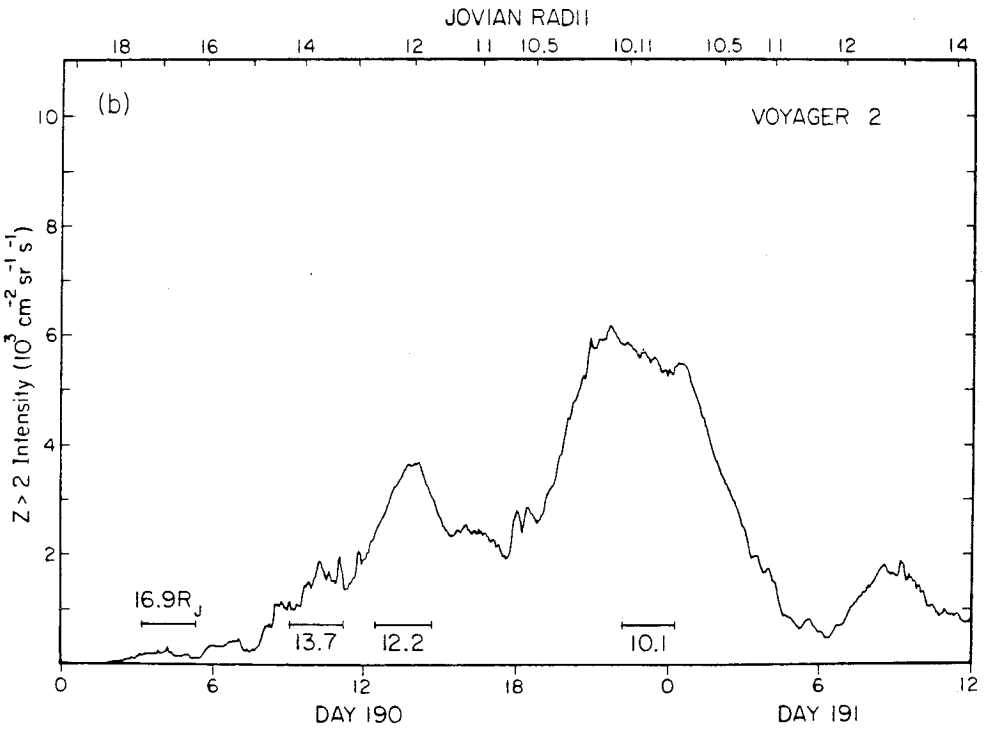
JOVIAN RADII
18 16 14 12 11 10.5 10.11 10.5 11 12 14
(b)
VOYAGER 2
Z > 2 Intensity (10^3 cm^{-2} sr^{-1} s^{-1})
16.9 R_J
13.7
12.2
10.1
0 6 12 18 0 6 12
DAY 190 DAY 191

sharply inside the peak densities at 5.7 R_J inbound (day 64 0924 UT) and 5.5 R_J outbound (day 64 1420 UT). Io's orbit, on the other hand is at 5.9 R_J, and the spacecraft crossed the magnetic field lines that pass through Io's orbit at 5.85 R_J outbound (day 64 1502 UT), as determined from measurements of the Io flux tube [Ness *et al.*, 1979a].

The energetic oxygen and sulfur losses are therefore more closely correlated with plasma features than with Io. Also, it was observed on the Voyager 1 inbound pass that the electromagnetic wave activity associated with the torus stopped abruptly at ~5.6 R_J [Scarf *et al.*, 1979]. Hence, the indication is that the losses are due to wave-particle interactions in the turbulent region outside 5.6 R_J scattering particles into the loss cone. Particle losses and loss mechanisms will be further discussed in Chapter 4. Note that minima in intensity measurements above a fixed energy threshold do not necessarily correspond to minima in the phase space densities of the particles. As will be shown (Figure 3.10), the intensity minima near Io correspond to a change in the radial gradient rather than a minimum in the phase space density profile.

The two decreases at ~9.4 R_J inbound and outbound were caused by Europa. In contrast to Voyager 1, the large scale structure in the Voyager 2 intensities (Figure 3.1b) is due to varying distance of the spacecraft from the magnetic equatorial plane. The peaks at day 190 1400 UT, 2200-2400 UT, and day 191 0900 UT are at times when the spacecraft crossed this plane.

The inbound Z>2 intensities for the two spacecraft are compared as a function of radial distance from Jupiter in Figure 3.2. Inside 17 R_J, the Voyager 1 and 2 intensities were the same to within a factor of two. There is therefore no evidence for major temporal variations in the heavy

Figure 3.2

The measured Z>2 intensities for Voyager 1 and 2 as a function of distance from Jupiter. The triangles indicate magnetic equatorial plane crossings.

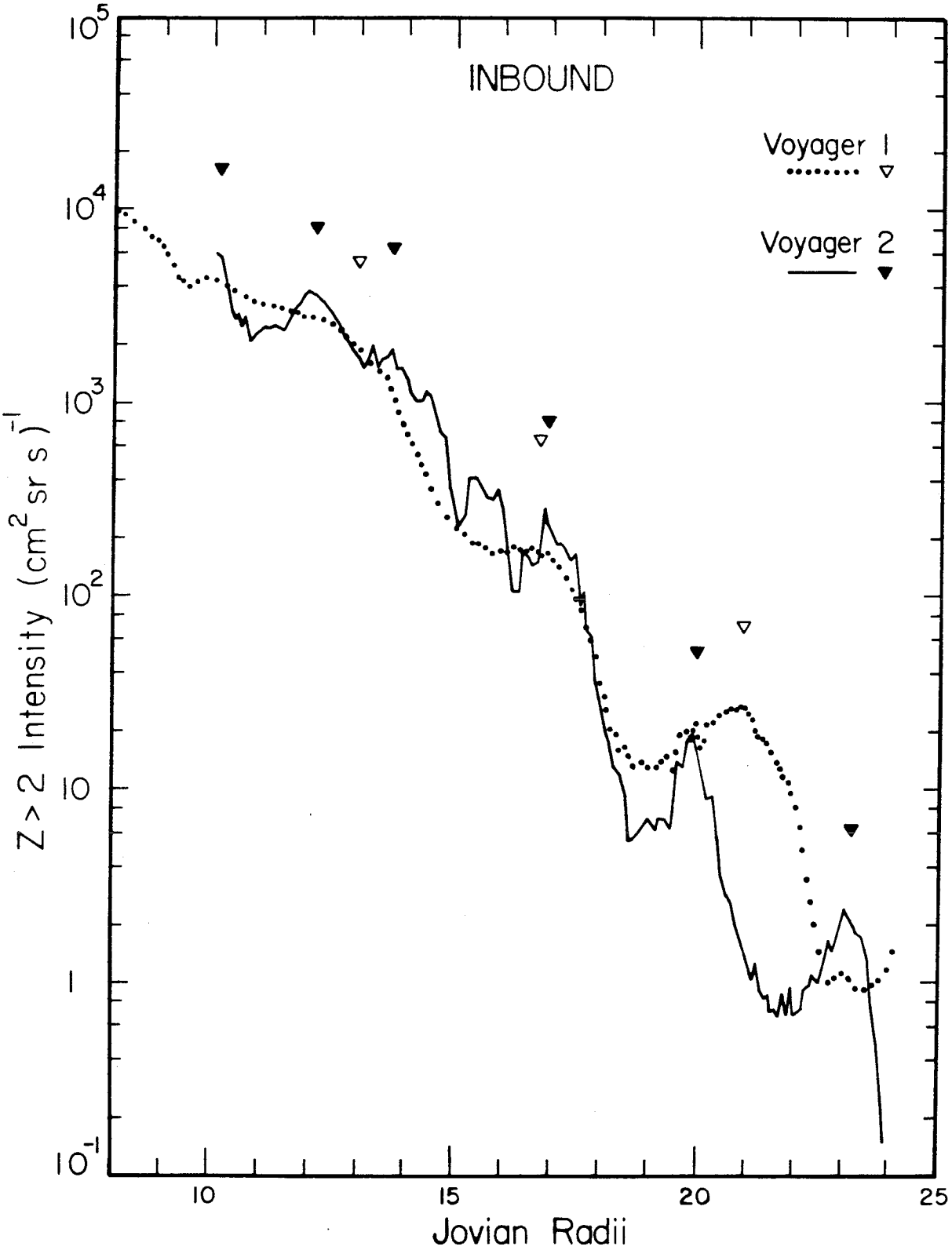
INBOUND
Voyager 1
Voyager 2
10^5
10^4
10^3
10^2
10
1
10^{-1}
Z > 2 Intensity $(cm^2 sr s)^{-1}$
10
15
20
25
Jovian Radii

ion intensities in this region between the two encounters, and in the analysis that follows, both sets of measurements will be considered to be of the same relatively stable population.

3.2 Differential Energy Spectra

Oxygen energy spectra have been calculated from the PHA events observed in the ten regions indicated in Figure 3.1 and listed in Table 3.1. The 5.3 and 5.9 R_J regions are each the combination of inbound and outbound regions symmetrically spaced with respect to the intensity minima near Io. For the regions near Io, sodium and sulfur spectra have also been calculated.

Figure 3.3a shows the 5.3 R_J oxygen and sulfur differential energy spectra. Also shown is the sodium spectrum from the combined 4.9 and 5.3 R_J regions. A striking feature in Figure 3.3a is the flattening of the oxygen and sulfur spectra below ~7 MeV/nuc and the actual decrease in the differential oxygen intensity below 5.5 MeV/nuc. The probable cause of this feature is that particle loss mechanisms near Io are more efficient for lower energy particles. Further evidence of this effect is provided by the observed factor of ~300 decrease in the differential intensity of $Z \geq 2$ ions with 1.0 − 1.8 MeV/nuc between ~7 and 5.6 R_J [Krimigis *et al.*, 1979]. Since the Z>2 integral intensity above ~1.0 MeV/nuc shown in Figure 3.1a decreases by only a factor of ~10, it is clear that the low energy ions are being preferentially lost in this region. Proton observations between 1 and 20 MeV near Io [Trainor *et al.*, 1974; Armstrong *et al.*, 1981] also indicate preferential low energy losses.

The 7.9 and 10.1 R_J differential oxygen spectra in Figure 3.3b show no evidence of flattening below 7 MeV/nuc. However, trapped energetic

Table 3.1

Region Definitions and Magnetic Field Values used in Spectral Analysis

Region* (R_J)	Voyager	Time (UT)	Magnetic Equatorial Plane Crossing Time (UT)	B Field at† Crossing (Gauss)
4.9	1	64/1106 - 64/1235	64/1200	3.26×10^{-2}
5.3	1	64/0936 - 64/1106	64/1034	2.79×10^{-2}
		64/1235 - 64/1405	64/1341	
5.9	1	64/0842 - 64/0936	64/0905	2.08×10^{-2}
		64/1405 - 64/1443	64/1428	
7.9	1	64/0546 - 64/0659	64/0608	7.18×10^{-3}
10.1	2	190/2214 - 191/0016	190/2300	3.34×10^{-3}
12.2	2	190/1235 - 190/1440	190/1338	1.74×10^{-3}
13.0	1	63/2328 - 64/0110	64/0008	1.32×10^{-3}
13.7	2	190/0907 - 190/1109	190/1008	1.20×10^{-3}
16.8	1	63/1818 - 63/2022	63/1920	4.85×10^{-4}
16.9	2	190/0312 - 190/0517	190/0415	6.11×10^{-4}
20.0	2	- ¶	189/2238	3.2×10^{-4}
20.9	1	-	63/1415	2.6×10^{-4}

* Distance between the spacecraft and the dipole center at the time of the magnetic equatorial plane crossing. Exceptions are 5.3 and 5.9 R_J where there were no crossings; the listed values are typical distances and times in these two regions.

† Magnetic field values from N. F. Ness (private communication).

¶ Spectra based on PHA events are not used at 20.0 and 20.9 R_J due to the difference in Voyager 1 and 2 Z>2 intensities at these radial distances and beyond.

Figure 3.3

Differential energy spectra observed in different regions of the magnetosphere (Table 3.1).

a) Oxygen and sulfur spectra from 5.3 R_J and the sodium spectrum from the combined 4.9 and 5.3 R_J regions. Note that the sulfur spectrum is multiplied by 20. The oxygen and sulfur data were obtained with LET B and the sodium data were obtained with LET B and D. The lines drawn through the oxygen and sulfur data become power-laws of indices approximately -6 at energies greater than ~10 MeV/nuc. The best-fit power-law line for the sodium spectrum has an index of -9. The oxygen point with dashed error bars at 2.2 MeV/nuc was derived from the integral spectrum in Figure 3.6.

b) Oxygen spectra from 7.9 and 10.1 R_J. The 7.9 R_J data were obtained with LET B and D (Voyager 1) and those at 10.1 R_J were obtained with LET B (Voyager 2). Power-law lines fit to the spectra have indices of -7.

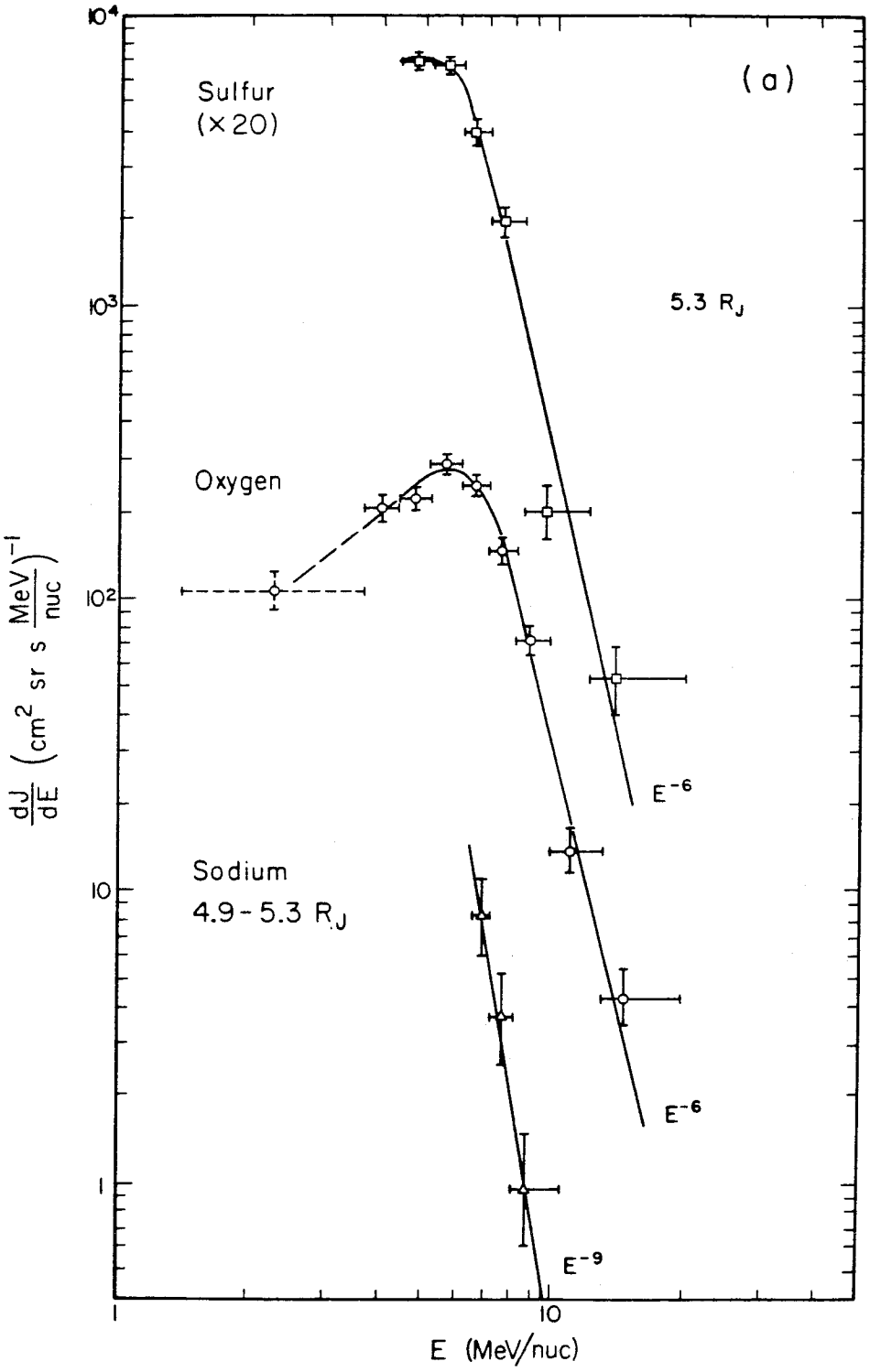
(a)
Sulfur
(×20)
5.3 R_J
Oxygen
Sodium
4.9 - 5.3 R_J
E^{-6}
E^{-6}
E^{-9}
10^4
10^3
10^2
10
1
1
10
E (MeV/nuc)
$\frac{dJ}{dE}$ $\left(\text{cm}^2\ \text{sr}\ \text{s}\ \frac{\text{MeV}}{\text{nuc}}\right)^{-1}$

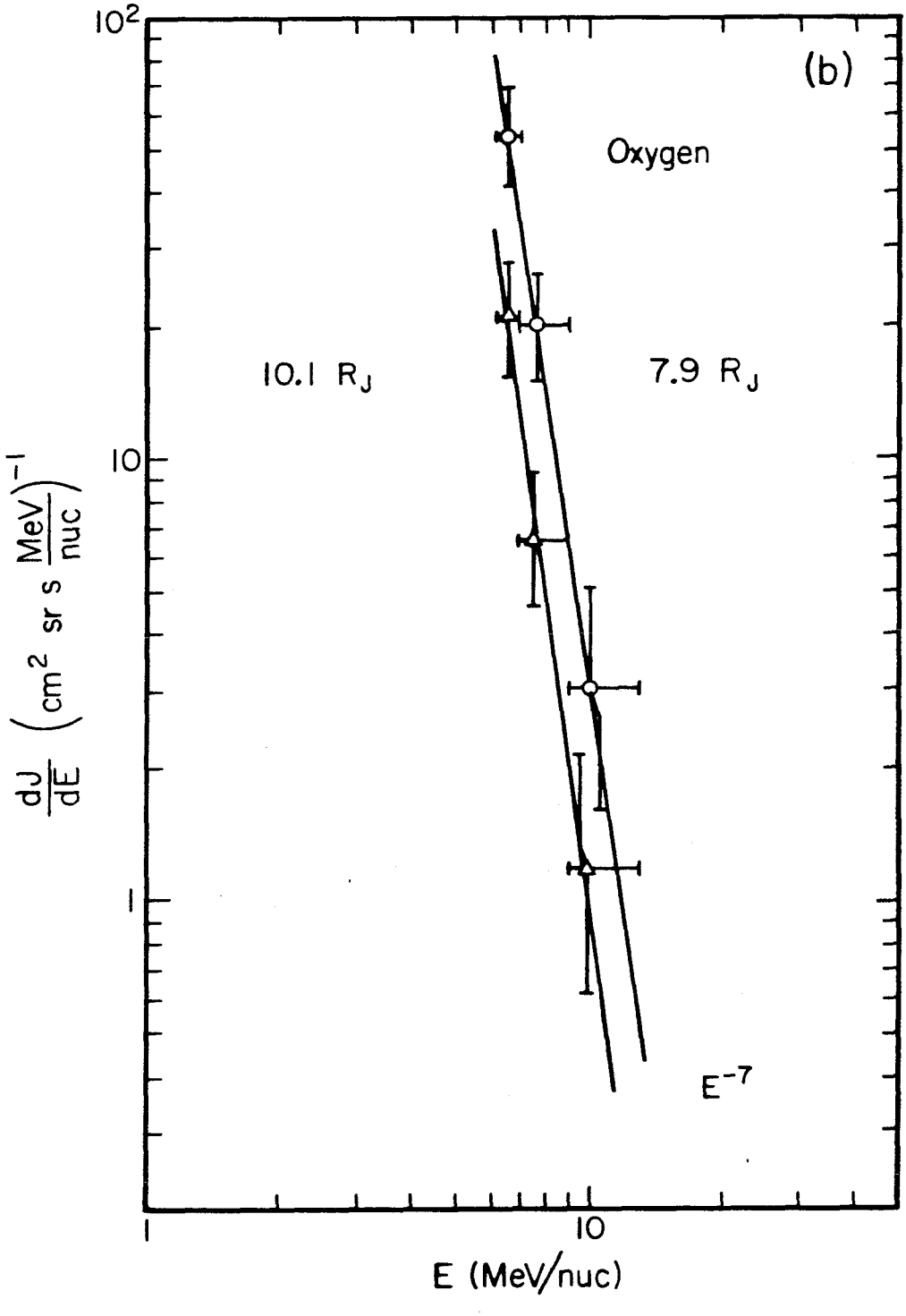
(b)
Oxygen
10.1 R_J
7.9 R_J
E^{-7}
10^2
10
1
1
10
E (MeV/nuc)
$\frac{dJ}{dE}$ $\left(\text{cm}^2\ \text{sr}\ \text{s}\ \frac{\text{MeV}}{\text{nuc}}\right)^{-1}$

particles do not conserve their energy as they diffuse radially in a magnetosphere, so that it is not meaningful to compare spectral features at a given energy from different radial locations.

Spectra can be compared in terms of other parameters such as particle magnetic moments, but before proceeding with such an analysis, we will extend the measured differential oxygen spectra to lower energies by converting to integral spectra and adding a point at ~1 MeV/nuc calculated from the Z>2 rate. To do this, it is necessary to determine the oxygen fraction of the Z>2 rate. In the 4.9 and 5.3 R_J regions the fraction can be directly measured using L1 pulse-height information as discussed in Chapter 2. The separate oxygen and sulfur peaks in Figure 2.5a can now be understood as the L1 energy loss of penetrating 5-6 MeV/nuc oxygen nuclei (E1~30 MeV) and sulfur nuclei (E1~120 MeV). This identification is reasonable since the differential energy spectra near Io have maxima at these energies. In other regions, the fraction must be inferred from elemental abundance measurements made at higher energies, as will now be discussed.

3.3 Elemental Abundances

At 4.9 and 5.3 R_J, the sulfur to oxygen ratio at constant energy per nucleon can be measured with reasonable statistical accuracy between approximately 4 and 20 MeV/nuc. The results are shown in Figures 3.4a and b. In both regions the ratio is seen to increase toward lower energies to values greater than one. The differential energy spectra in Figure 3.3a indicate that this strong energy dependence of the ratio is caused by particle loss effects near Io. In the other regions listed in Table 3.1 there were not enough sulfur events to make a statistically

Figure 3.4

The energy dependence of the sulfur to oxygen ratio at constant energy per nucleon from several regions of the magnetosphere.

a) 4.9 R_J - LET B

b) 5.3 R_J - LET B (the same data as shown in Figure 3.3a)

c) 5.6 - 25. R_J

Voyager 1 63/0854 - 64/0936 UT LET B and D

Voyager 2 189/1408 - 191/0410 UT LET B and D

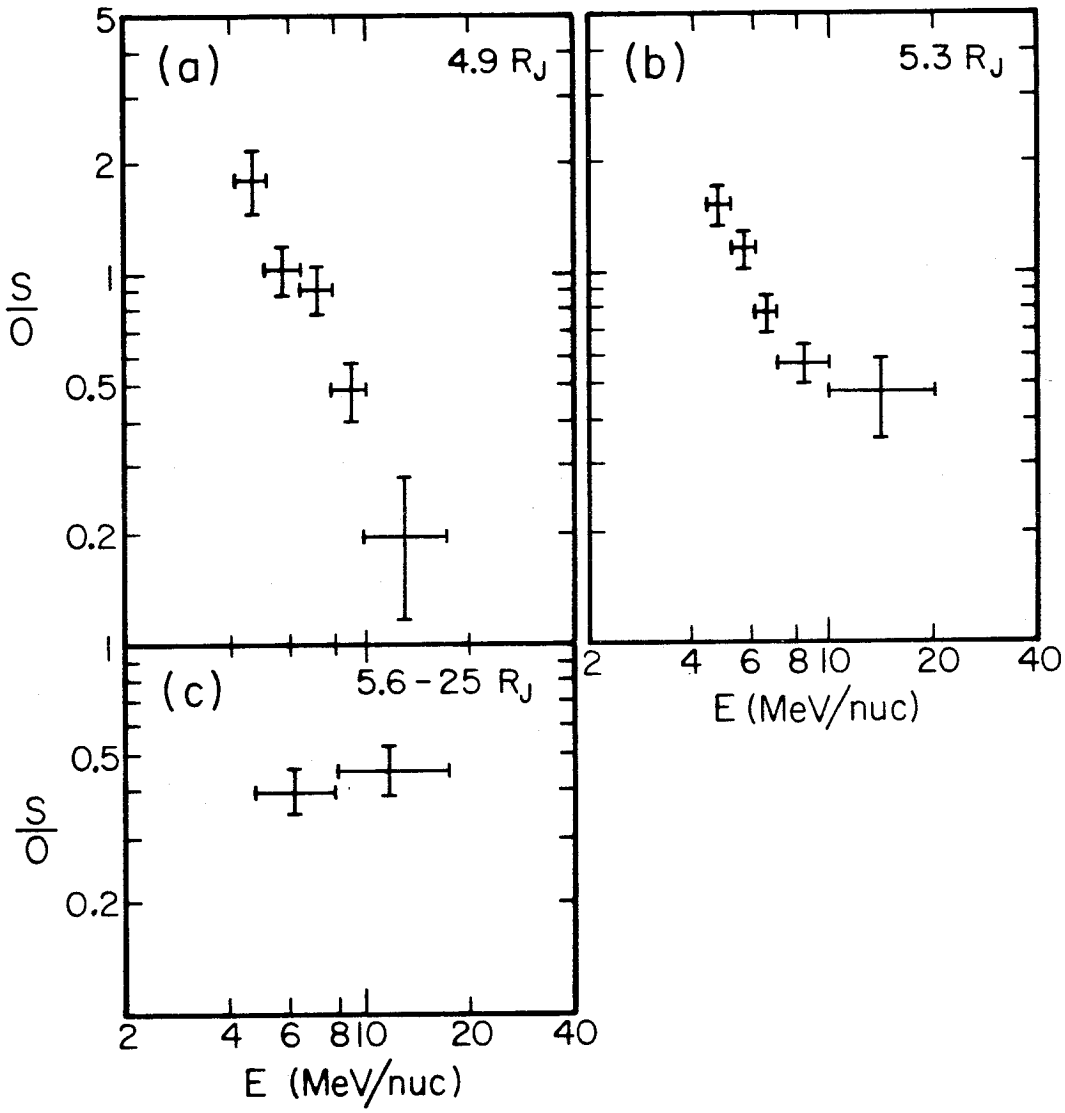
(a)
4.9 R_J
(b)
5.3 R_J
(c)
5.6 - 25 R_J
S/O
E (MeV/nuc)
5
2
1
0.5
0.2
2
4
6
8
10
20
40

significant determination of the energy dependence of the ratio, so instead, all the data from 5.6 to 25 R_J inbound were combined into one measurement. The result, shown in panel c, indicates that the sulfur to oxygen ratio is approximately independent of energy outside the Z>2 intensity minima near Io. In order to compare the observed abundance ratios to those made by other instruments at different energies and in different locations in the magnetosphere, it is useful to relate them to a diffusion theory.

The radial diffusion theory that will be adopted for the present analysis assumes that particles conserve their first and second adiabatic invariants but not their third in the diffusion process (see e.g. Schulz and Lanzerotti [1974]). Conservation of the first invariant or magnetic moment, $M = p_\perp^2 / 2mB$ where m is the particle mass, B is the magnetic field strength and $p_\perp$ is the momentum perpendicular to the B-field direction, gives a linear scaling of energy with magnetic field strength, $E = MB$ (nonrelativistic), for the special case of mirroring particles (pitch angle, $\alpha=90°$).

Since a particle's magnetic moment is a conserved quantity, measurements from different locations in the magnetosphere can be compared as a function of M. If analysis is restricted to observations of $\alpha=90°$ particles, the magnetic moment can be easily calculated from the measured particle energies and the local magnetic field strength. Abundance measurements such as those shown in Figure 3.4 were not restricted in this regard, and, particularly outside 5.6 R_J, represent a mixture of pitch angles. However, as will be seen (Figure 3.7), the Z>2 ions have an equatorial pitch-angle distribution that increases toward 90°, so that the mixture is biased in favor of larger pitch angles. The approximation will therefore be made in the analysis that follows that

M=E/B. The average of the LET B and D pointing directions with respect to the magnetic field between 6 and 20 R_J is ~60°, implying that, even if the pitch-angle distribution were istropic in this region, the approximation would still be good to ~30%.

The observed sulfur to oxygen ratio, S/O, is shown as a function of M in Figure 3.5a. The error bars with no symbols and with solid symbols represent the ratio of the integral sulfur and oxygen measurements between ~6 and ~15 MeV/nuc. (The exact energy ranges for each point are given in the figure caption.). The points with open symbols were calculated using published data from the Low Energy Charged Particle (LECP) instrument on Voyager 2 [Hamilton *et al.*, 1981]. The LECP sulfur to oxygen ratios were measured between 10 and 60 R_J inbound for ions with energies range 0.60 to 1.15 MeV/nuc. The magnetic moment for each measurement (CRS and LECP) was calculated by dividing the lowest energy of the measurement range by the local magnetic field value [Ness *et al.*, 1979a,b and private communication]. Since the sulfur and oxygen spectra outside 6 R_J decrease steeply toward higher energies near ~1 MeV/nuc ($\frac{dJ}{dE} \propto E^{-3}$ for oxygen at 10 R_J), the value plotted at a given M is approximately the integral sulfur to oxygen ratio above that M. The horizontal error bars on the CRS points represent the variation in the magnetic field strength over the measurement region.

Similar plots of the carbon to oxygen ratio, C/O, and the sodium to oxygen ratio, Na/O, are shown in Figures 3.5b and c. The energy dependent data inside 5.6 R_J were not used in these figures except for a S/O point for E>6.6 MeV/nuc at 5.3 R_J where the energy dependence is less pronounced, and a Na/O point for E>6.6 MeV/nuc at 4.9 R_J to make use of the few available sodium events. (These are the points at 2.5×10^2

Figure 3.5

Abundance ratios with respect to oxygen of a) sulfur, b) carbon, and c) sodium as functions of the particle magnetic moments. The data were obtained outside 5.6 R_J, except as noted in the text. The magnetic moment for each observation was calculated by dividing the lowest energy in the measurement energy range by the measured local magnetic field strength. The open symbols were calculated using data from the Low Energy Charged Particle (LECP) instrument on Voyager 2 [Hamilton *et al.*, 1981]. The symbols in the plot are defined as

┼ Voyager 1 6.6-17.3 MeV/nuc

● Voyager 2 7.5-11.0 MeV/nuc

■ Voyager 1 4.7-14.8 MeV/nuc

◆ = ● + ■

○ LECP (VGR 2) 0.60-1.15 MeV/nuc.

The vertical error bars represent statistical uncertainties and the horizontal error bars on the CRS data represent the range of magnetic field strengths in the region. The power-law lines in the figures are fits to the combined CRS and LECP data. The functional forms are $\frac{S}{O} = 1.5\,M^{-0.17}$, $\frac{C}{O} = 2.3\text{x}10^{-3}M^{0.56}$, and $\frac{Na}{O} = 0.1\,M^{-0.12}$.

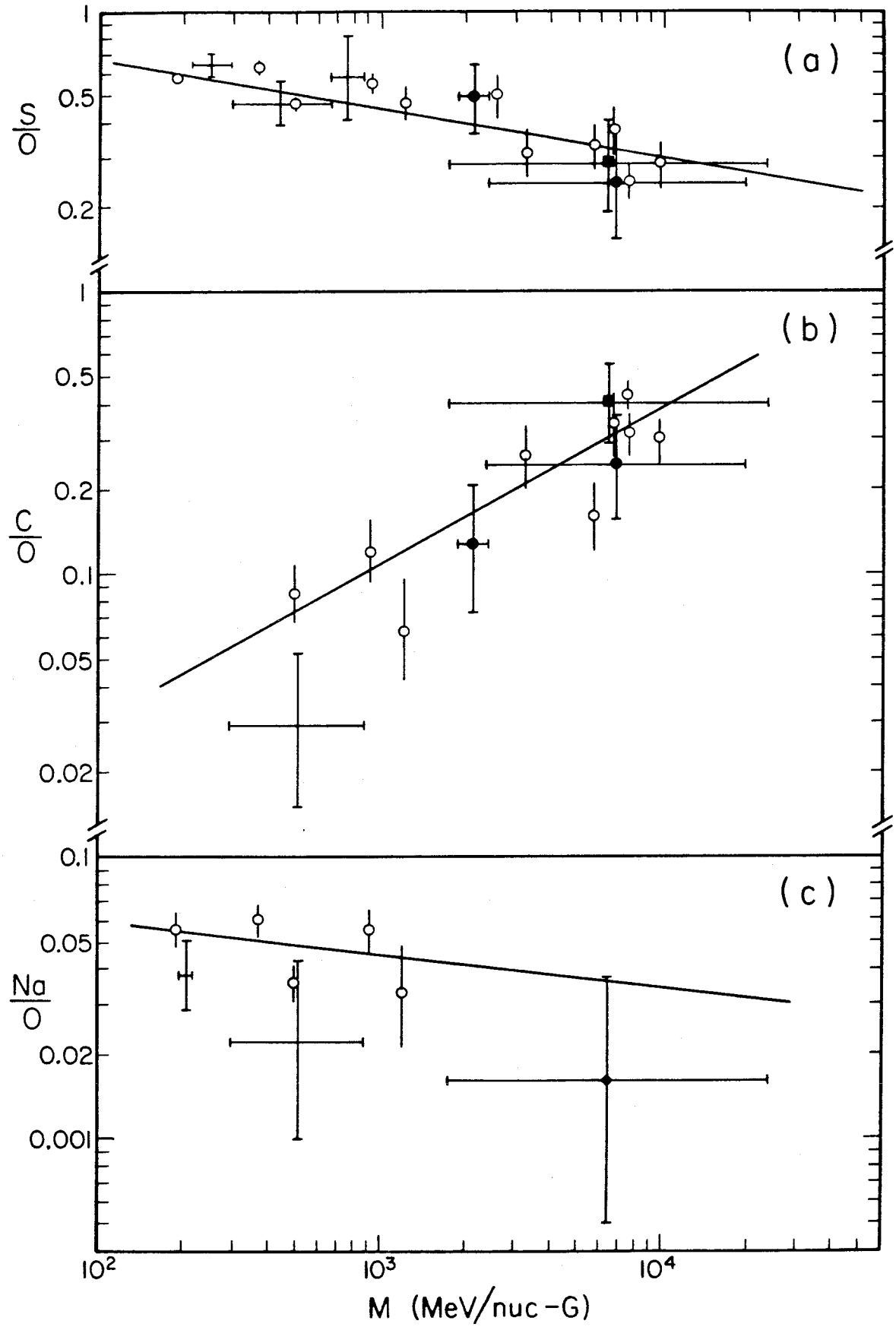
(a)
S/O
1
0.5
0.2
(b)
C/O
1
0.5
0.2
0.1
0.05
0.02
(c)
Na/O
0.1
0.05
0.02
0.001
10²
10³
10⁴
M (MeV/nuc-G)

MeV/nuc-G in the figure.)

The agreement between the CRS and LECP observations in Figure 3.5 demonstrates that M is a reasonable parameter to use when comparing data from different regions of the the magnetosphere outside 5.6 R_J. The lines shown in the figure are power-law fits to the combined data sets. S/O and Na/O are seen to increase toward smaller magnetic moments while C/O decreases. Therefore an instrument measuring abundance ratios in a fixed energy range will detect increasing sulfur and sodium and decreasing carbon abundances relative to oxygen as it moves toward smaller radial distances (larger magnetic fields). Also, an instrument at a fixed radial position will measure a sulfur to oxygen and sodium to oxygen ratio that increases toward lower energies and a carbon to oxygen ratio that decreases, or, in other words, sulfur and sodium spectra that are softer than that of oxygen, and a carbon spectrum that is harder. If the approximation is made that the energy spectra of these elements are proportional to $E^{-\gamma}$, then the fits shown in the figure indicate that $\gamma_S = \gamma_O + 0.2$, $\gamma_C = \gamma_O - 0.6$, and $\gamma_{Na} = \gamma_O + 0.1$.

3.4 Integral Energy Spectra

The data in Figure 3.5 can now be used to calculate the oxygen fraction of the Z>2 rate. The calculation was performed as follows: The L1 effective Z>2 thresholds for carbon, oxygen, and sulfur ions in a given region were determined from the observed Z>2 rate and pulse-height distribution in L1 using the information in Table B.2, and were converted to magnetic moment thresholds M_C, M_O, and M_S, by dividing by the observed magnetic field strength in that region (Table 3.1). It was assumed that the integral intensity of species k above a given M could be

represented by a power law, $J_k(>M)=A_kM^{-\gamma_k}$ where A_k and γ_k are constants. The sulfur to oxygen ratio, for example, is then $\frac{S}{O}(M) = A_SM^{-\gamma_S}/A_OM^{-\gamma_O}$. With this assumption, and the observation that, inside 20 R_J, carbon, oxygen, and sulfur are more abundant than other Z>2 elements, the oxygen fraction of the Z>2 rate is given by

$$\left[\frac{O}{O+C+S}\right]_{Z>2\ rate} \approx \frac{1}{1 + \frac{C}{O}(M_C)\left[\frac{M_C}{M_O}\right]^{-\gamma_O} + \frac{S}{O}(M_S)\left[\frac{M_S}{M_O}\right]^{-\gamma_O}} . \qquad (3.1)$$

The carbon to oxygen and sulfur to oxygen ratios were obtained from Figure 3.5, and γ_O was determined from the measured spectra.

The oxygen fraction of the Z>2 rate in each region is listed in Table 3.2 in addition to other quantities need to calculate the oxygen intensity from the observed Z>2 rate. The oxygen fraction for 4.9 and 5.3 R_J was not calculated in this way, but was directly measured using L1 pulse-height information as previously discussed (see e.g. Figure 2.5).

For each region, an integral oxygen energy spectrum was determined, including a point based on the Z>2 rate. Examples from 5.3 and 10.1 R_J are shown in Figure 3.6, where J(E) is the integral intensity of particles with energy greater than E. The higher energy continuous portions of the spectra correspond to the differential spectra in Figure 3.3, and are joined by dashed curves to the points calculated from the Z>2 rate. The energy at which the Z>2 point is plotted is the effective L1 Z>2 threshold for oxygen ions in the given region, and was determined using the data in Table B.2. The value of the effective threshold in each region is listed in Table 3.2.

Table 3.2

Quantities Used to Calculate Oxygen Intensities from the Z>2 Rate

Region (R_J)	LET	Observed Z>2 Rate (s-1)	Effective Oxygen[§] Z>2 Threshold (MeV/nuc)	Oxygen Fraction* of the Z>2 Rate	Z>2 Livetime[¶] Correction Factor	LZ3 Livetime[†] Correction Factor
4.9	B	1.2×10^4	1.4	0.52**	1.3	1.5
5.3	B	1.0×10^4	1.4	0.53	1.2	1.5
5.9	B	1.3×10^4	1.5	0.51	1.3	1.5
7.9	B	2.7×10^4	1.5	0.48	1.7	1.5
	D	2.5×10^4			1.6	1.5
10.1	B	1.9×10^4	1.3	0.50	1.4	1.6
12.2	B	1.3×10^4	1.2	0.50	1.2	1.6
	D	1.1×10^4			1.2	1.6
13.0	B	8.0×10^3	1.1	0.51	1.1	1.6
	D	6.1×10^3			1.1	1.6
13.7	B	7.1×10^3	1.1	0.50	1.1	1.6
	D	6.3×10^3			1.1	1.6
16.8	B	7.5×10^2	1.1	0.53	1.0	1.6
	D	5.4×10^2			1.0	1.6
16.9	B	1.4×10^3	1.1	0.52	1.0	1.6
	D	1.2×10^3			1.0	1.6
20.0	B	8.5×10^1	1.1	0.53	1.0	-
	D	6.0×10^1			1.0	-
20.9	B	1.2×10^2	1.1	0.53	1.0	-
	D	7.0×10^1			1.0	-

§ Calculated from the observed Z>2 rate and L1 pulse-height distribution using Table B.2. The nominal oxygen threshold is 1.1 MeV/nuc (sulfur is 0.9 MeV/nuc, carbon is 1.2 MeV/nuc). These thresholds include the particle energy loss in the telescope window.

* From equation (3.1) in all regions except 4.9 and 5.3 R_J, where it was directly measured using L1 pulse-height information. Note: this is not an abundance fraction.

¶ From Table B.1. 1.0 implies no correction.

† From Figure B.1. Spectra based on PHA events were not calculated at 20.0 and 20.9 R_J. The 4.9, 5.3, and 5.9 R_J spectra have an additional pulse pileup correction (Appendix B) of magnitude 1.4 for $E \lesssim 7$ MeV/nuc.

** The similarity in these numbers is coincidental, due to an increasing carbon fraction toward larger radial distances offsetting the effect of a decreasing sulfur fraction.

Figure 3.6

Integral energy spectra of oxygen ions at 5.3 and 10.1 R_J. The continuous portions of the spectra are based on PHA events. No binning has been done, so that each event is shown as a step up in integral intensity. The points with error bars were determined from the Z>2 rate. The uncertainty in these points is due primarily to abundance uncertainties. The dashed line joining the two parts of each spectrum represents an interpolation of maximum smoothness [Zmuidzinas, 1981].

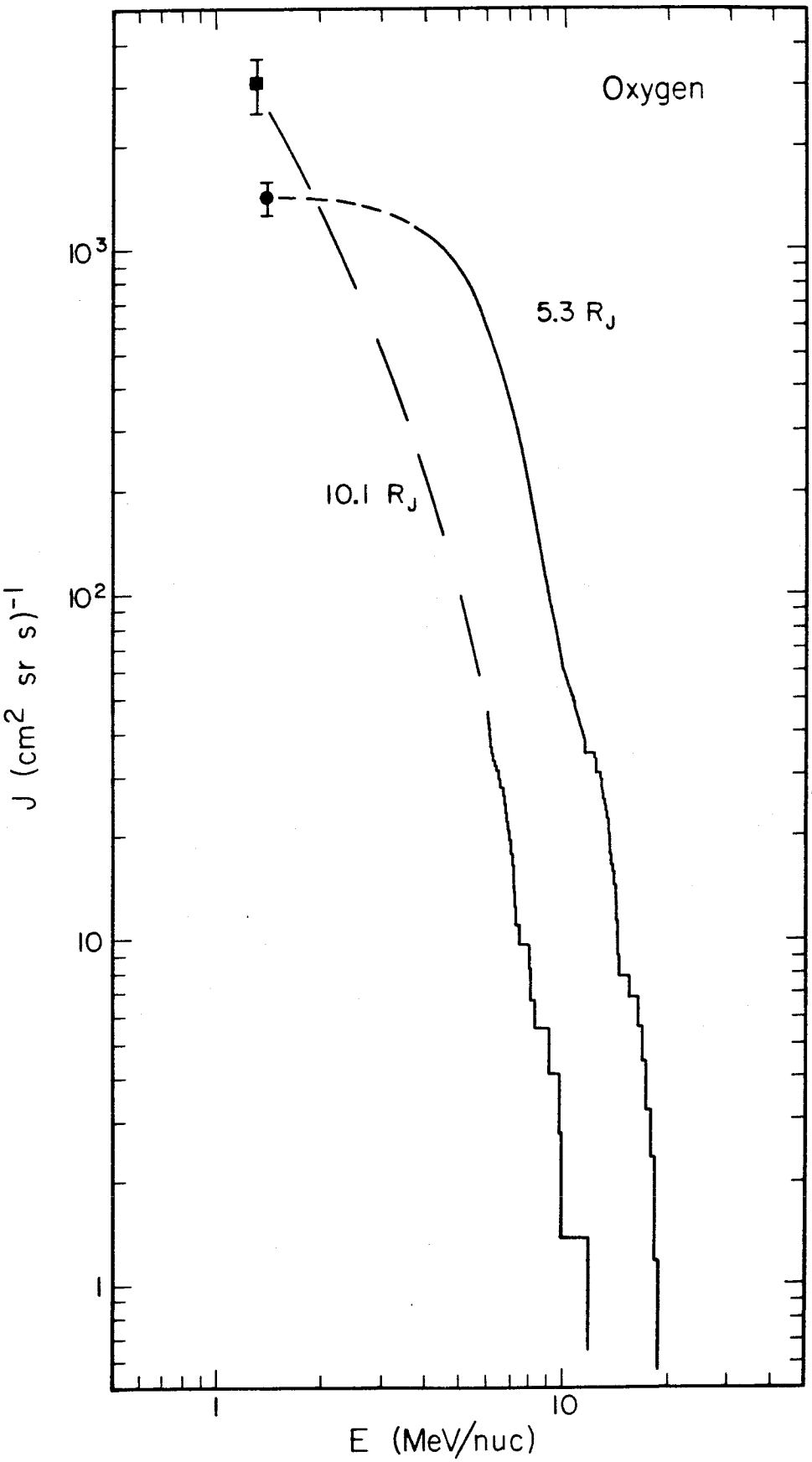
Oxygen
5.3 R_J
10.1 R_J
10^3
10^2
10
1
J (cm^2 sr s)$^{-1}$
1
10
E (MeV/nuc)

The flattening of the 5.3 R_J spectrum below ~5.5 MeV/nuc corresponds to the decrease in differential intensity seen in Figure 3.3a (p. 42). The point with the dashed error bars at 2.2 MeV/nuc in that figure was calculated from the integral spectrum in Figure 3.6, and shows that the differential intensity decreases even further at energies below 3.5 MeV/nuc. The 10.1 R_J spectrum continues rising steeply toward lower energies between 6.0 and 1.3 MeV/nuc although there is some hardening toward lower energies. The spectral index, γ, ($J \propto E^{-\gamma}$) changes from 5 at 6 MeV/nuc to 2 at 1.3 MeV/nuc. The integral spectra from all regions will be presented and compared in the next section.

3.5 The Phase Space Density

3.5.1 Intensity - Phase Space Density Relationships

Since particle energies change in the diffusion process, the radial diffusion theory deals with particle phase space densities at constant magnetic moment rather than three-dimensional space densities at constant energy. The radial diffusion equation is

$$\frac{\partial f}{\partial t} = L^2 \frac{\partial}{\partial L}\left[\frac{D}{L^2}\frac{\partial f}{\partial L}\right] + \mathcal{S}(L) - \mathcal{L}(L) \qquad (3.2)$$

(see e.g. Schulz and Lanzerotti [1974]) where f is the phase space density at a particular M, D is the diffusion coefficient, L is the McIlwain parameter, and $\mathcal{S}(L)$ and $\mathcal{L}(L)$ represent local sources and sinks respectively. Equation (3.2) can be used with measurements of the gradient of f to obtain quantitative information about diffusive flows and particle losses. The objective here will be to determine the radial dependence of the energetic oxygen phase space density for several

values of M.

The relationship between the phase space density and the measured integral intensity, J, is

$$f(p,L,\alpha) = -\frac{1}{p^2}\frac{dJ_\alpha(E,L)}{dE} \qquad (3.3)$$

where α is the particle pitch angle. Specializing to the $\alpha = 90°$ case and changing variables from E and p to M gives

$$f(M,L,\alpha=90°) = \frac{\gamma(M,L)}{2mM^2}\frac{J_\perp(M,L)}{B^2(L)} \qquad (3.4)$$

where $\gamma = -\frac{d\ \log(J_\perp)}{d\ \log(M)}$ and $J_\perp$ is the integral intensity of particles with $\alpha=90°$. The phase space density can therefore be directly calculated from measurements of the magnetic field strength, the integral intensity, and the logarithmic slope of the integral intensity.

Equation (3.4) specifies that the integral intensity measurements be of mirroring particles. Also, implicit in the diffusion equation is the requirement that observations of f at different L values be made at points along the dynamic paths that particles follow in the diffusion process. This means, for example, that measurements made at radial positions L_i of particles mirroring at distances d_i from the magnetic equatorial plane should only be compared with one another if the coordinates (L_i, d_i) all lie on the mirror point trajectory of the radially diffusing particles. In the present study, consideration is restricted to particles mirroring at the magnetic equatorial plane to insure that the measurements are along mirror point trajectories, independent of the magnetic field configuration.

The regions that have been chosen for analysis (Table 3.1) each include a crossing of the magnetic equatorial plane, except the 5.3 and

5.9 R_J regions, where the spacecraft was near the plane ($\lesssim 5°$ dipole latitude). The exact times that the spacecraft crossed the magnetic equatorial plane were identified using magnetic field magnitude and pointing data (N. F. Ness, private communication) and are listed in Table 3.1. The L values assigned to each region are the spacecraft – dipole center distance at the time of the crossing, and are the distances used to name the regions.

3.5.2 Pitch Angle Distribution Corrections

The intensity of mirroring particles at a given location can only be directly measured with a telescope oriented perpendicular to the local magnetic field. At the times of the magnetic equatorial plane crossings, however, LET B and D had pointing directions with respect to the field that were in general not 90° (see Table 3.3), and, in fact, varied considerably from region to region. In order to determine $J_\perp$ from the measured intensities, a study was made of the equatorial pitch-angle distribution of the energetic oxygen ions.

It was assumed that the distribution of particles intensities as a function of their equatorial pitch angle, α_0, could be represented by the Legendre polynominal

$$f(\alpha_0) = a_0 + a_2 \frac{3}{2}(\cos^2\alpha_0 - \frac{1}{3}) \qquad (3.5)$$

where a_0 and a_2 are constants. This distribution was then integrated with the angular response functions of the LET B and D Z>2 rate to yield two linear equations relating a_0 and a_2 to the measured intensities and pointing directions of the telescopes [Gehrels and Chenette, 1981]. The ratio a_2/a_0 was calculated from these equations in thirty-minute

Table 3.3

Telescope Pointing Directions
and Correction Factors

Region (R_J)	Pointing Angle w.r.t. Field Line		Z>2 Pointing† Correction Factor		LZ3 Pointing† Correction Factor	
	LET B	LET D	LET B	LET D	LET B	LET D
4.9	68°	36°	1.2	- ¶	1.1	- ¶
5.3 inbound	60	35	1.3	-	1.2	-
outbound	65	32	1.3	-	1.2	-
5.9 inbound	54	35	1.4	-	1.4	-
outbound	65	30	1.3	-	1.2	-
7.9	55	53	1.3	1.4	1.3	1.4
10.1	65	46	1.2	-	1.2	-
12.2	77	41	1.1	1.5	1.0	1.7
13.0	78	36	1.1	1.7	1.0	1.9
13.7	57	44	1.3	1.5	1.2	1.6
16.8	49	50	1.4	1.4	1.4	1.4
16.9	75	53	1.1	1.4	1.0	1.4
20.0	71	42	1.1	1.6	-	-
20.9	90	48	1.1	1.5	-	-

† A Compton-Getting correction due to the rotation of the magnetosphere is included in these factors. The approximation was made that the rotation speed is 0.8 that of corotation in these regions [McNutt et al., 1981]. The contribution to the total correction is $\lesssim$0.05.
The correction factors for 5.3 and 5.9 R_J take into account the nonzero magnetic latitude of the spacecraft in these regions, as determined from the magnetic field data.

¶ In the 4.9, 5.3, 5.9, and 10.1 R_J regions, only LET B was used because it provided adequate statistics by itself and was more nearly perpendicular to the magnetic field than LET D.

averaging intervals from 20 R_J inbound through closest approach on Voyager 2 and inside 7 R_J on Voyager 1. The ratio was found to be approximately constant in this region with a distribution of values shown in Figure 3.7a. The distribution has a mean value of $a_2/a_0 = -0.7$, which was chosen as the representative value throughout the region, and a standard deviation of 0.2. The shape of a pitch-angle distribution of the form given in (3.5) with $a_2/a_0 = -0.7$ has a maximum at $\alpha_0 = 90°$ as shown in Figure 3.7b. $J_\perp$ at a given crossing of the magnetic equatorial plane is therefore higher than the measured LET B and D intensities.

Using the above pitch-angle distribution and the known telescope pointing directions (Table 3.3), the value of $J_\perp$ at each magnetic equatorial plane crossing was calculated from the LET B and D intensities. The ratio between $J_\perp$ and the measured intensities is called the pointing correction factor, and is listed in Table 3.3. The pointing correction factors for the Z>2 rate are slightly different than those for the LZ3 rate due to their different angular response functions.

The specific procedure followed in determining $J_\perp(M)$ in each region was as follows: Integral energy spectra were calculated for LET B and D (in some regions only LET B) using the values of the Z>2 rate and LZ3 rate (equation 2.1) measured at the magnetic equatorial crossing. The pointing corrections (Table 3.3) were then applied, and the LET B and D spectra combined, to yield a single spectrum of α_0=90° oxygen ions in each region. In the 4.9, 5.3, 5.9, and 10.1 R_J regions, only LET B was used to determine $J_\perp$ because it provided adequate statistics by itself in these regions and was pointed more nearly perpendicular to the magnetic field direction than LET D (Table 3.3). The value of the magnetic field strength used to convert the integral energy spectrum in each region into an

Figure 3.7

a) A histogram of measurements of the pitch-angle distribution parameter ratio a_2/a_0. The distribution of particles intensities as a function of their equatorial pitch angle, α_0, is assumed to be of the form $f(\alpha_0) = a_0 + a_2 \frac{3}{2}(\cos^2\alpha_0 - \frac{1}{3})$. The data shown in the figure represent thirty-minute averages of a_2/a_0 as determined by the LET B and D Z>2 rates measured by Voyager 2 on day 190 and by Voyager 1 between 64/0730 UT and 64/1630 UT. Periods in which the telescope pointing directions relative to the magnetic field direction were within 10° of one another were not included due to the large uncertainties in the calculated ratios during them. The mean value of the ratio for the data shown in the figure is -0.67. It was therefore assumed that $a_2/a_0 = -0.7$ throughout this region.

b) The shape of the pitch-angle distribution for $a_2/a_0 = -0.7$. The ratio, a_2/a_0, was directly measured only for $30° \lesssim \alpha_0 \lesssim 150°$, so that the shape of the actual distribution near $\alpha_0 = 0°$ and 180° is not necessarily as shown.

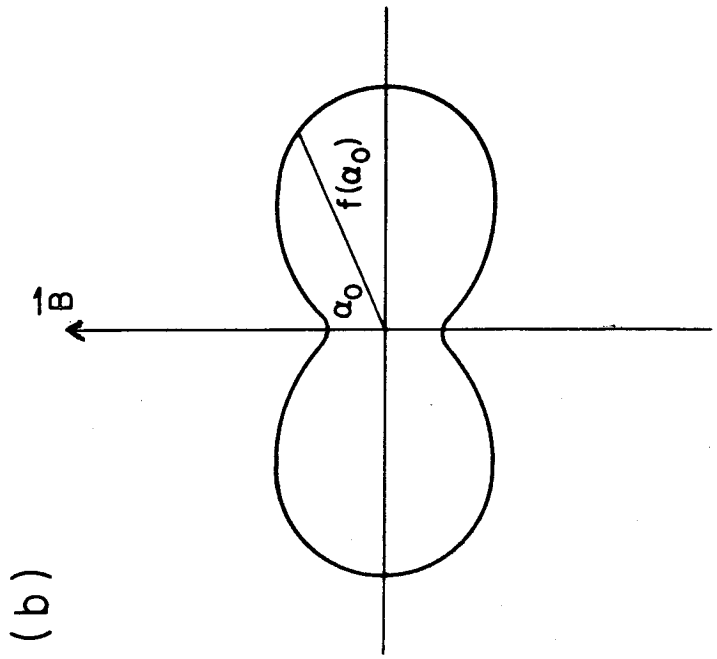
(b)
B
a_0
$f(a_0)$

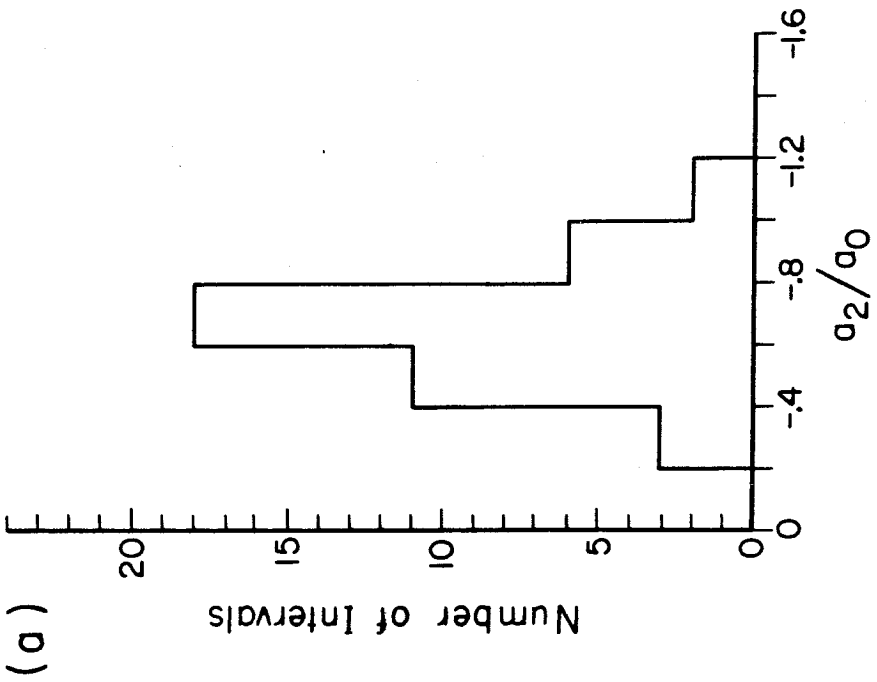
(a)
Number of Intervals
0
5
10
15
20
0
-.4
-.8
-1.2
-1.6
a_2/a_0

integral magnetic moment spectrum was the measured value at the time of the magnetic equatorial plane crossing and is listed in Table 3.1.

3.5.3 Phase Space Density Determination

The phase space density of the energetic oxygen ions can now be determined from the measurements of $J_{\perp}(M,L)$ and $B(L)$ using equation (3.4)

$$f(M,L,\alpha=90°) = \frac{\gamma(M,L)}{2mM^2}\frac{J_{\perp}(M,L)}{B^2(L)}.$$

As a first step, we show in Figure 3.8 the quantity $J_{\perp}/B^2$ as a function of magnetic moment for the measured spectra in all regions. The event portions of the Voyager 1 13.0 and 16.8 R_J spectra are represented by single points instead of by complete spectra due to the few PHA events obtained in these regions. These measurements, as well as the two intensity measurements based on the Z>2 rate, are important, however, because they confirm that, to within a factor of two, the Voyager 1 and 2 intensities of energetic oxygen ions were the same between 12 and 17 R_J. Therefore, inside 17 R_J, spectra from the two spacecraft will be directly compared in the analysis that follows. Outside 17 R_J, the Voyager 1 intensities of energetic Z>2 ions were higher than those of Voyager 2, as can be seen by the two intensity measurements near 20 R_J in this figure and by the radial comparison of the Z>2 intensities in Figure 3.2.

The short-dashed curves in Figure 3.8 are extrapolations of the measured spectra to smaller magnetic moments, while the error bars represent the range of uncertainty in the extrapolations. Except at 10.1 R_J, the upper and lower limits for each error bar were determined by

Figure 3.8

Integral oxygen spectra from all regions listed in Table 3.1 divided by the square of the local magnetic field strengths, as a function of magnetic moment. The spectra are represented in the same way as those in Figure 3.6. The event portion of the 4.9 R_J spectrum is shown as a dotted curve to distinguish it from the 5.3 R_J spectrum. Intensities derived from the PHA events at 13.0 and 16.8 R_J are represented by open symbols rather than by line spectra because few events were obtained in these regions (~10 events in each region), and are shown primarily for comparison with the Voyager 2 spectra. The short-dashed curves and the dash-dotted curve at 10.1 R_J represent extrapolations of the measured spectra as discussed in the text. The error bars without symbols indicate the uncertainties in the extrapolations.

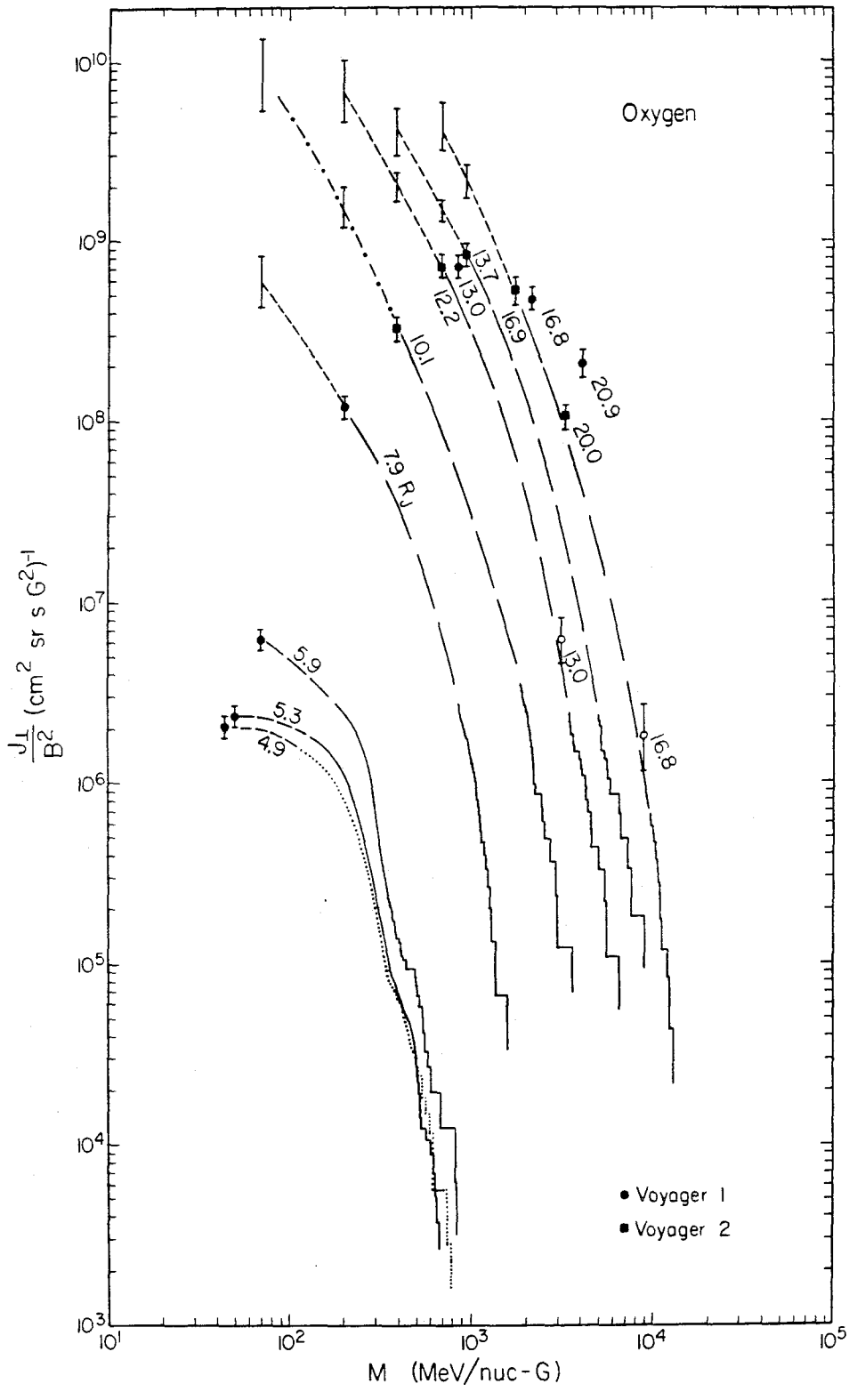
Oxygen
7.9 Rj
10.1
12.2
13.0
13.7
16.9
16.8
20.9
20.0
13.0
16.8
5.9
5.3
4.9
Voyager 1
Voyager 2
$\frac{J_\perp}{B^2}$ (cm^2 sr s G^2)$^{-1}$
M (MeV/nuc-G)

extending the spectra from the Z>2 point with lines of slope $\gamma_{Z>2}$ and $\gamma_{Z>2}/1.4$ respectively, where $\gamma_{Z>2}$ is the slope at the Z>2 point.

At 10.1 R_J, a longer extrapolation was performed than in other regions in order to extend the spectrum to 70 MeV/nuc-G (see section 4.6). In this case, the shape of the spectrum was calculated using the energy per charge spectrum measured at these magnetic moments by LECP at ~16 R_J on Voyager 2 [Hamilton *et al.*, 1981]. Hamilton *et al.* [1981] show that different elements have similar spectral shapes at the same energy per charge, if one assumes reasonable charge states for the different ions. They therefore combine all elements into a single spectrum that covers approximately two orders of magnitude in energy. The lowest energy oxygen measurement in the spectrum is at M≈500 MeV/nuc-G, but the spectral shape is determined by protons and helium ions to magnetic moments as low as ~80 MeV/nuc-G. The integral oxygen intensity profile used to extrapolate the 10.1 R_J spectrum was obtained by converting from energy per charge to energy per nucleon, integrating to obtain J(E), and then converting to J(M) using $B \approx 6 \times 10^{-4}$ G.

LECP observations were also used as a consistency check of the spectral slopes at the Z>2 points in Figure 3.8. Figure 3.9 shows these slopes compared to those measured in the energy range from 0.60 to 3.17 MeV/nuc between 10 and 25 R_J [Hamilton *et al.*, 1981]. The values from the two instruments are the same within statistics, and both show the same trend of softer spectra toward increasing radial distance.

In order to use the diffusion equation (3.2) to understand particle observations, one must determine the radial dependence of the phase space density at a constant value of M. Radial profiles of f at constant magnetic moment can be directly obtained for the energetic oxygen ions

Figure 3.9

A comparison of the slope of the oxygen spectrum at the Z>2 point (~1 MeV/nuc) observed by CRS, with the power-law index between 0.60 and 3.17 MeV/nuc measured by LECP [Hamilton *et al.*, 1981]. Note that the γ plotted is the power-law index for a differential spectrum ($\frac{dJ}{dE} \propto E^{-\gamma}$), so that, for the CRS observations, $\gamma = \gamma_{Z>2} + 1$, where $\gamma_{Z>2}$ is the slope of the integral spectrum at the Z>2 point.

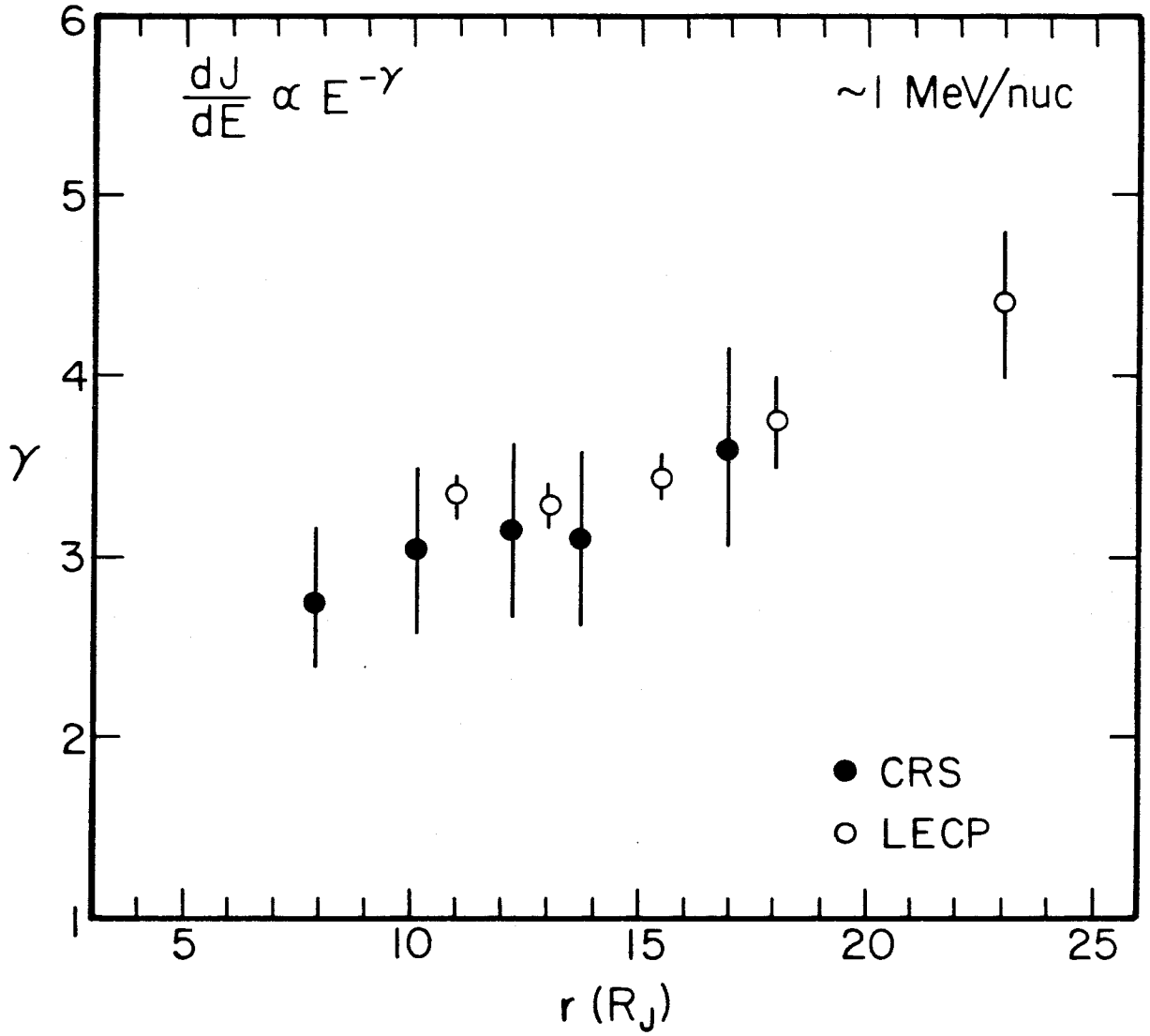
$\frac{dJ}{dE} \propto E^{-\gamma}$
~1 MeV/nuc
γ
r (R_J)
CRS
LECP
1
2
3
4
5
6
5
10
15
20
25

from Figure 3.8 using equation (3.4). The results are shown for several values of M in Figure 3.10. The filled symbols in the figure denote phase space densities determined directly from the spectra in Figure 3.8, while the open symbols are based on the extrapolations of the spectra discussed above.

The uncertainties, σ_f, shown for each measurement of f, represent uncertainties in the magnetic field strength, σ_{1/B^2}, in the oxygen abundance fraction of the Z>2 rate, $\sigma_{abundance}$, in the pulse pileup correction factor for the two-detector portions of the spectra near Io, σ_{2-D}, in γ(M,L), σ_γ, in the pointing correction factor, $\sigma_{pointing}$, and statistical counting uncertainties in the number of events in the event portions of the spectra, σ_{events}. The estimated contribution to σ_f from each of these sources is listed in Table 3.4 for all measurements. An additional ~15% systematic uncertainty in the livetime correction factor applies to all measurements.

The observations at all values of M show a positive radial gradient in the phase space density of the energetic oxygen ions between 5.6 and 17 R_J. The diffusive flow in this region is therefore inward. Inside 5.6 R_J, the phase space density is nearly constant. The discontinuity in the gradient of f at ~5.6 R_J corresponds to the minima in the Z>2 intensities near Io (Figure 3.1).

Figure 3.10

The radial dependence of the phase space density of the energetic oxygen ions at constant magnetic moment, for several values of M. The filled points are derived from the measured portions of the spectra shown in Figure 3.8, while the open points are based on the extrapolations. The 4.9 and 5.3 R_J measurements at 6.9×10^2 MeV/nuc-G were averaged together to improve statistics. Solid lines join the measurements at given magnetic moments between 7.9 and 16.9 R_J. The 5.3, 5.9, and 7.9 R_J measurements are connected by dashed lines to indicate that the radial profile in this region may have discontinuities between the points.

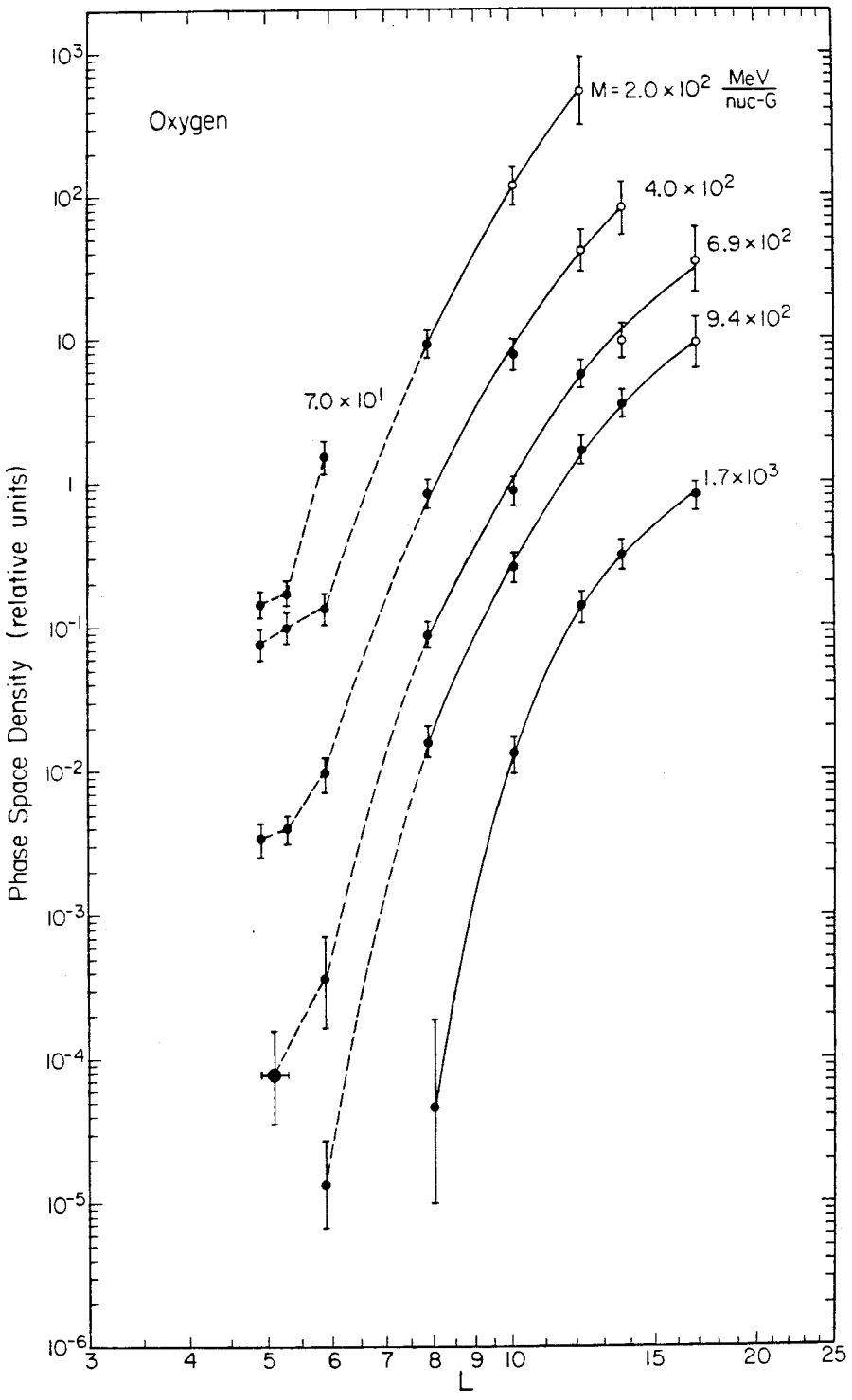
Oxygen
M = 2.0 × 10² MeV/nuc-G
4.0 × 10²
6.9 × 10²
9.4 × 10²
1.7 × 10³
7.0 × 10¹
Phase Space Density (relative units)
L
10³
10²
10
1
10⁻¹
10⁻²
10⁻³
10⁻⁴
10⁻⁵
10⁻⁶
3
4
5
6
7
8
9
10
15
20
25

Table 3.4

Contributions to the Phase
Space Density Uncertainties

M (MeV/nuc-G)	L	σ_{1/B^2} (%)	$\sigma_{abund.}$ (%)	σ_{events} (%)	$\sigma_{2\text{-}D}$ (%)	σ_{γ} (%)	$\sigma_{point.}$ (%)	f (relative)	σ_f (%)
7.0×10^{1}	4.9	6	15	0	0	15	10	1.4×10^{-1}	24
	5.3	"	"	"	"	"	"	1.7×10^{-1}	"
	5.9	"	"	"	"	"	"	1.5×10^{0}	"
2.0×10^{2}	4.9	6	0	7	15	15	10	7.5×10^{-2}	25
	5.3	"	"	5	"	"	"	9.8×10^{-2}	"
	5.9	"	"	7	"	"	"	1.3×10^{-1}	"
	7.9	"	15	0	0	"	"	9.1×10^{0}	24
	10.1	-	-	extrapolation		-	-	1.3×10^{2}	36
	12.2	-	-	extrapolation		-	-	5.3×10^{2}	72
4.0×10^{2}	4.9	6	0	27	0	20	10	3.3×10^{-3}	36
	5.3	"	"	21	"	"	"	3.9×10^{-3}	31
	5.9	"	"	30	"	"	"	9.4×10^{-3}	38
	7.9	"	15	0	"	15	"	8.4×10^{-1}	24
	10.1	"	"	"	"	"	"	7.7×10^{0}	"
	12.2	-	-	extrapolation		-	-	4.1×10^{1}	40
	13.7	-	-	extrapolation		-	-	8.0×10^{1}	54
6.9×10^{2}	<4.9,5.3>	6	0	100	0	20	10	7.8×10^{-5}	103
	5.9	"	"	"	"	"	"	3.6×10^{-4}	"
	7.9	"	15	0	"	15	"	8.7×10^{-2}	24
	10.1	"	"	"	"	"	"	8.8×10^{-1}	"
	12.2	"	"	"	"	"	"	5.7×10^{0}	"
	13.7	-	-	extrapolation		-	-	9.6×10^{0}	30
	16.9	-	-	extrapolation		-	-	3.5×10^{1}	67
9.4×10^{2}	5.9	6	0	150	0	50	10	1.3×10^{-5}	160
	7.9	"	"	18	"	20	"	1.6×10^{-2}	29
	10.1	"	15	0	0	15	"	2.6×10^{-1}	24
	12.2	"	"	"	"	"	"	1.7×10^{0}	"
	13.7	"	"	"	"	"	"	3.5×10^{0}	"
	16.9	-	-	extrapolation		-	-	9.3×10^{0}	49
1.7×10^{3}	7.9	6	0	300	0	50	10	4.7×10^{-5}	304
	10.1	"	"	21	"	15	"	1.3×10^{-2}	28
	12.2	"	15	0	"	"	"	1.4×10^{-1}	24
	13.7	"	"	"	"	"	"	3.1×10^{-1}	"
	16.9	"	"	"	"	"	"	8.1×10^{-1}	"

Chapter 4

Discussion

4.1 Overview

The measurements of the phase space density of the energetic oxygen ions (Figure 3.10) can be used both to learn more about the ions themselves and to place limits on parameters that control the energy and particle budget of the magnetosphere. Concerning the ions, the specific objectives of this chapter are to 1) establish their overall flow pattern and the location of their acceleration region, 2) calculate the total inward diffusive flow between 5 and 17 R_J, and 3) determine the magnitude and cause of the losses in the region. Objectives 2 and 3 require knowledge of the diffusion coefficient. The energetic oxygen data can be used to place limits on this parameter that are adequate for the analysis, and that are also interesting in that they specify limits on the total plasma outflow from the torus and thereby on the rate at which oxygen and sulfur ions are produced near Io.

The radial dependence of the inward diffusive flow rate of the oxygen ions, calculated using the diffusion coefficient limits, indicates that almost all of the ions are lost between 12 and 5 R_J. In order to determine the cause of these losses, we calculate in the fifth section of the chapter the relative importance of several possible loss processes. The only viable loss mechanism is found to be pitch-angle scattering into the loss cone. This implies that most of the energy delivered to the inner magnetosphere by the oxygen and sulfur ions ends up in the Jovian atmosphere. It is of particular interest to compare this power input into the atmosphere with the total power required to produce the observed auroral activity [Broadfoot *et al.*, 1979; Sandel *et al.*, 1979], which is the

most energetic phenomenon associated with the inner magnetosphere.

4.2 The Oxygen Flow Pattern and Acceleration Process

The positive radial gradient in the phase space density of the energetic oxygen ions between 6 and 17 R_J causes an inward diffusive flow in this region, and indicates that the acceleration region is outside 17 R_J. Oxygen ions with magnetic moments in the range 10^2–10^4 MeV/nuc–G have also been observed throughout the magnetosphere by the LECP instrument [Krimigis *et al.*, 1979; Hamilton *et al.*, 1981; Krimigis *et al.*, 1981]. In addition to the ~16 R_J measurement discussed in the last chapter, LECP observations in two other regions are of particular interest in this study; one was made just inside the magnetopause at 65 R_J on Voyager 1 [Krimigis *et al.*, 1979] and the other in the magnetospheric wind region (r>150 R_J outbound) on both Voyager 1 and 2 [Krimigis *et al.*, 1981]. The J/B^2 calculated from the 65 R_J measurement is two to three orders of magnitude larger, at the same value of M, than that at 16.9 R_J in Figure 3.8. This observation does not necessarily imply particle flow directly in from 65 to 17 R_J since there may be a maximum in the phase space density at some intermediate distance, but it does confirm that the acceleration region is outside 17 R_J. The magnetospheric wind observation shows that ions flow outward as well as inward from the acceleration region.

The oxygen and sulfur rich composition of the energetic ions indicates that their original source is the Io torus. The observations therefore suggest that plasma ions diffuse outward from the Io torus, are nonadiabatically accelerated in some region outside 17 R_J, and then diffuse inward and outward from the acceleration region. The radial

diffusion process will change particle energies, but is assumed to conserve magnetic moments. The LECP measurements just described and the CRS measurements reported here both require an acceleration mechanism that is capable of increasing particle magnetic moments from that of the plasma near Io, $\sim 10^{-4}$ MeV/nuc–G, up to $\sim 10^{4}$ MeV/nuc–G.

One possible mechanism is that proposed by Eviatar *et al.* [1976] to predict the observed energetic sodium component in the magnetosphere. In that model, fast neutral particles, possibly produced by charge exchange between neutrals and corotating plasma near Io, escape the magnetosphere and become ionized in the solar wind. The ions are then accelerated to the ~400 km/s solar wind speed and re-enter the magnetosphere. This mechanism will, however, result in magnetic moments of not more than ~20 MeV/nuc–G. Two other possibilities are stochastic acceleration by cyclotron waves in the plasma of the outer magnetosphere [Papadopoulos *et al.*, 1980], or the application of magnetic pumping models [Sentman *et al.*, 1975; Goertz, 1978; Borovsky *et al.*, 1981] to heavy ions.

4.3 Diffusion Coefficient Determinations

In order to use the observed oxygen spectra and phase space density profiles to determine the diffusive flow rate at which particles and energy enter the inner magnetosphere, it is necessary to know the diffusion coefficient. The objective of this section is to place limits on the value of the diffusion coefficient between 5.3 and 17 R_J based on limiting assumptions concerning the magnitude of the losses in the region.

The diffusion equation (3.2) for a steady-state condition in a region in which there are no sources and where the loss term is of the form

$\mathcal{L} = f/\tau$, where τ is the particle lifetime, is

$$L^2 \frac{\partial}{\partial L}\left[\frac{D}{L^2}\frac{\partial f}{\partial L}\right] = \frac{f}{\tau} . \qquad (4.1)$$

We first consider the extreme case in which there are no losses ($\tau \to \infty$) between 5 and 17 R_J.

4.3.1 Lossless Diffusion

For the case of no losses, equation (4.1) gives

$$D = \frac{c\, L^2}{\partial f/\partial L} \qquad (4.2)$$

where c is a constant. Relative diffusion coefficients can therefore be directly calculated from the phase space density measurements. For ease of calculation, the radial dependence of f at a given magnetic moment is approximated as a series of power-law lines connecting the measured points at different values of L. Comparison with the smoothed curves in Figure 3.10 indicates that this is a reasonable approximation.

Figure 4.1 shows the values of the diffusion coefficient at five radial positions calculated using equation (4.2). The points are normalized to D=1.0 at L=11.4, and have errors that represent the uncertainties in the measured phase space densities. The relative diffusion coefficients for different magnetic moments are seen to be the same within statistics. Also shown in the figure are two lines of the form $D=D_0L^n$, where D_0 and n are constants. The radial dependence of the calculated points can be adequately represented by n=−7 between ~7 and ~12 R_J and n=0 between ~12 and ~15 R_J. This analysis shows that it is possible to obtain radial profiles of f between 7 and 15 R_J similar to those measured, without

Figure 4.1

Relative values of the lossless diffusion coefficient between 6 and 17 R_J at several oxygen magnetic moments; calculated using equation (4.2). The gradient in the phase space density was determined from the measured values of f (Figure 3.10) assuming $f \propto L^q$ between measurements. The points are normalized to D=1.0 at L=11.4, and have errors that represent the uncertainties in f. Power-law lines of the form $D = D_0 L^n$ with n=−7 and n=0 are shown for comparison.

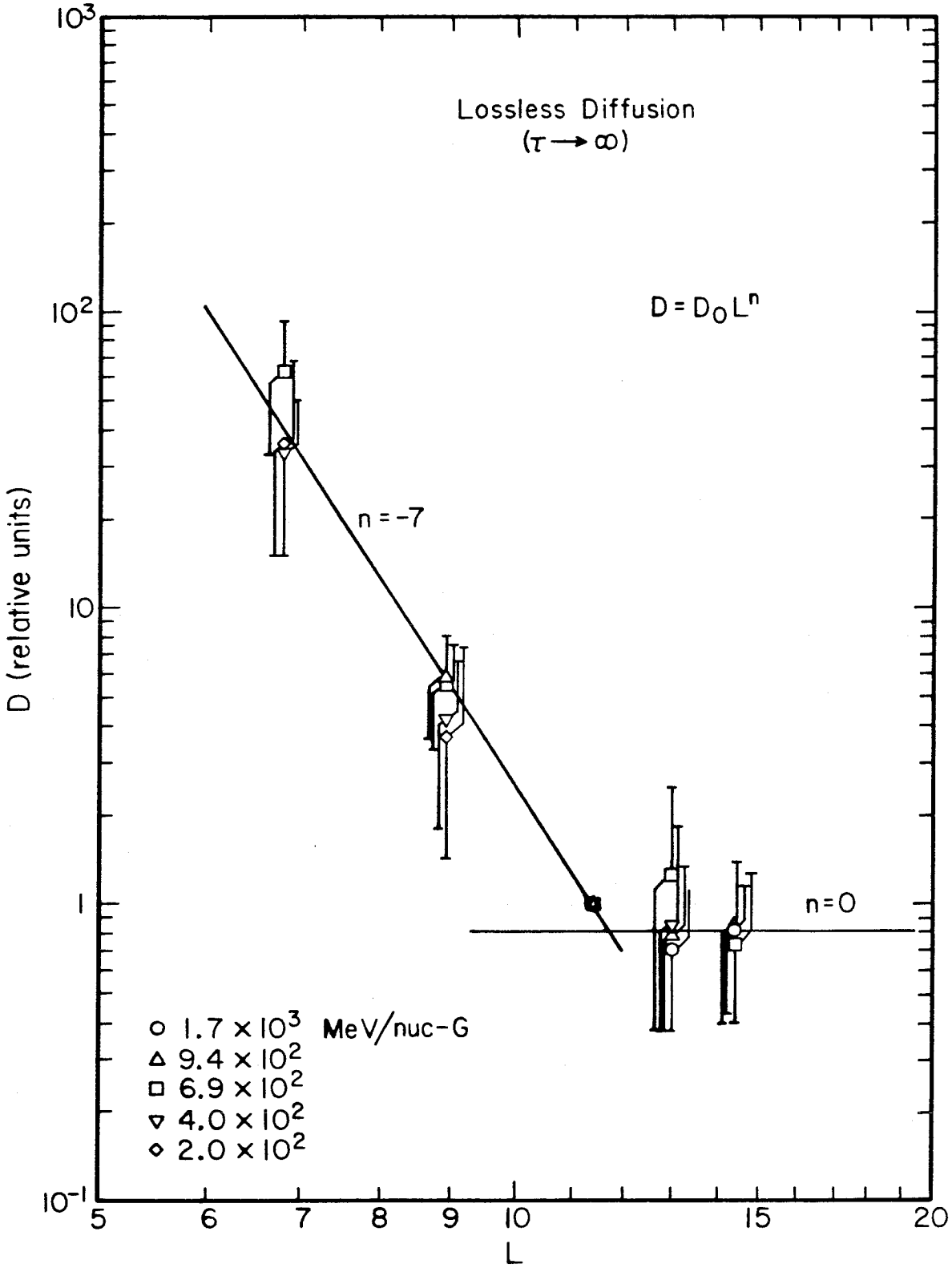
Lossless Diffusion
(τ → ∞)
D = D0 L^n
n = -7
n = 0
D (relative units)
L
10^3
10^2
10
1
10^-1
5
6
7
8
9
10
15
20
o 1.7 × 10^3 MeV/nuc-G
Δ 9.4 × 10^2
□ 6.9 × 10^2
▽ 4.0 × 10^2
◇ 2.0 × 10^2

invoking any particle losses. The resulting radial dependence of D, however, does not satisfy a desired constraint that will now be discussed.

The radial dependence of the diffusion coefficient in the inner magnetosphere can be independently determined using Voyager measurements of the plasma density profile [Froidevaux, 1980; Richardson *et al.*, 1980, Richardson and Siscoe, 1981; Siscoe *et al.*, 1981]. In particular, the recent analysis by Siscoe *et al.* [1981] between 5.8 and 9 R_J gives

$$\begin{aligned} D &= 2.6\times10^{-38}\ S\ L^{4.5}\ \ s^{-1} && 5.8<L\leq7.12 \\ D &= 1.7\times10^{-45}\ S\ L^{12}\ \ s^{-1} && 7.12<L\leq8 \\ D &= 2.6\times10^{-37}\ S\ L^{4}\ \ s^{-1} && 8<L\leq9 \end{aligned} \qquad (4.3)$$

where S (in ions/s) is the Io source strength of oxygen and sulfur ions. As discussed in the introduction, S is probably in the range from 10^{27} to 10^{28} ions/s, but may be as large as 10^{29} ions/s. The most likely diffusion mechanism between 6 and 9 R_J is flux tube interchange driven by centrifugal forces on the plasma created near Io [Siscoe and Summers, 1981], and therefore, since the mechanism involves magnetic field motion, the diffusion coefficient is the same for the plasma and the energetic ions.

The diffusion coefficient in (4.3) is not adequate by itself for the present analysis because of its limited radial range (L<9), and because of the uncertainty in S, but it does indicate that the n=−7 radial dependence of the lossless diffusion coefficient between ~7 and ~12 R_J in Figure 4.1 is inconsistent with the plasma measurements. Therefore, diffusion with non-zero losses will now be considered.

4.3.2 Lossy Diffusion

As an opposite limit to the case of no losses, it is assumed in this section that strong pitch-angle diffusion is occurring. This means that there is sufficient pitch-angle scattering to refill the loss cone with particles as quickly as it empties, and therefore that the lifetime of the particles to pitch-angle scattering is a minimum. The loss cone solid angle at the magnetic equatorial plane (both directions) is approximately $2\pi\alpha_{0l}^2$ where α_{0l} is the equatorial loss cone angle, and the time required to empty it of particles is approximately one quarter of the bounce period, τ_b, [Kennel and Petschek, 1966], so that

$$\tau_{strong} = \frac{\tau_b/4}{\alpha_{0l}^2/2} . \qquad (4.4)$$

For nonrelativistic particles at constant M, assuming a dipolar Jovian magnetic field of 4 G–R_J^3,

$$\tau_{strong} \approx 5\ M^{-1/2}\ L^{11/2}\ [4-3/L]^{1/2} \quad s \qquad (4.5)$$

where [M]=MeV/nuc-G. The deviation of the measured magnetic field from a dipole [Connerney *et al.*, 1981] tends to decrease α_{0l} and thereby increase τ_{strong}. The difference, however, is estimated to be less than ~50% between 6 and 17 R_J, and in the analysis that follows, equation (4.5) will be used to calculate τ_{strong}.

The objective now is to calculate the diffusion coefficient using $\tau = \tau_{strong}$. Inside 9 R_J, the radial dependence of D is specified by Voyager plasma measurements and is given explicitly by equation (4.3). In this region therefore, the diffusion coefficient can be fully determined by obtaining a value for S. Between 7 and 8 R_J there are two discontinuities

in the plasma diffusion coefficient representing observed discontinuities in the radial gradient of the plasma density [Siscoe *et al.*, 1981]. This implies that there are also discontinuities in the radial gradient of the energetic oxygen phase space density between the 5.9 and 7.9 R_J measurements, and therefore that the radial resolution of the energetic oxygen measurements is insufficient in this region to independently determine the gradient in f for a comparison with the plasma observations. Between 8 and 9 R_J, however, a comparison can be made and a value obtained for the diffusion coefficient. Outside 9 R_J, a numerical solution of the diffusion equation relates the diffusion coefficient to the one calculated between 8 and 9 R_J.

The radial dependence of f in this analysis is again approximated as a series of power-law lines connecting the measured points in Figure 3.10. Specifically, assuming $f \propto L^q$ and $D=2.6\times10^{-37} S L^4$ between 8 and 9 R_J, the diffusion coefficient at 8.9 R_J is

$$D(8.9) = \frac{8.9^2}{q(q+1)\tau_{strong}(8.9,M)} . \qquad (4.6)$$

For a given M, the values of the diffusion coefficient at larger radial distances were determined from the value at 8.9 R_J using a finite difference solution of the diffusion equation (4.1). For instance, D(11.4 R_J) was calculated using

$$10.1^2\left(\frac{D(11.4)\frac{\partial f}{\partial L}(11.4)/11.4^2 - D(8.9)\frac{\partial f}{\partial L}(8.9)/8.9^2}{11.4-8.9}\right) = \frac{f(10.1)}{\tau_{strong}(10.1)} . \qquad (4.7)$$

Figure 4.2 shows the values of D obtained in this way at several

Figure 4.2

Values of the lossy diffusion coefficient between 9 and 17 R_J for the case of strong pitch-angle diffusion ($\tau = \tau_{strong}$; τ_{strong} given by equation (4.5)). The points at 8.9 R_J were calculated using equation (4.6), where q is the power-law index of the phase space density between 7.9 and 10.1 R_J. This equation was derived assuming that $D \propto L^4$ between 8 and 9 R_J as indicated by Voyager plasma data [Siscoe *et al.*, 1981]. The solid lines in the figure show the dependence of the plasma diffusion coefficient on the Io source strength, S, of oxygen and sulfur ions. The points at 11.4, 13.0, and 14.4 were calculated using equations like (4.7). The dashed lines are the diffusion coefficient limits (D_u – upper, D_l – lower) that will be used in the analysis that follows, with the range of values at 5.3 R_J determined from Pioneer measurements of energetic protons and electrons [Goertz *et al.*, 1978; Thomsen *et al.*, 1977].

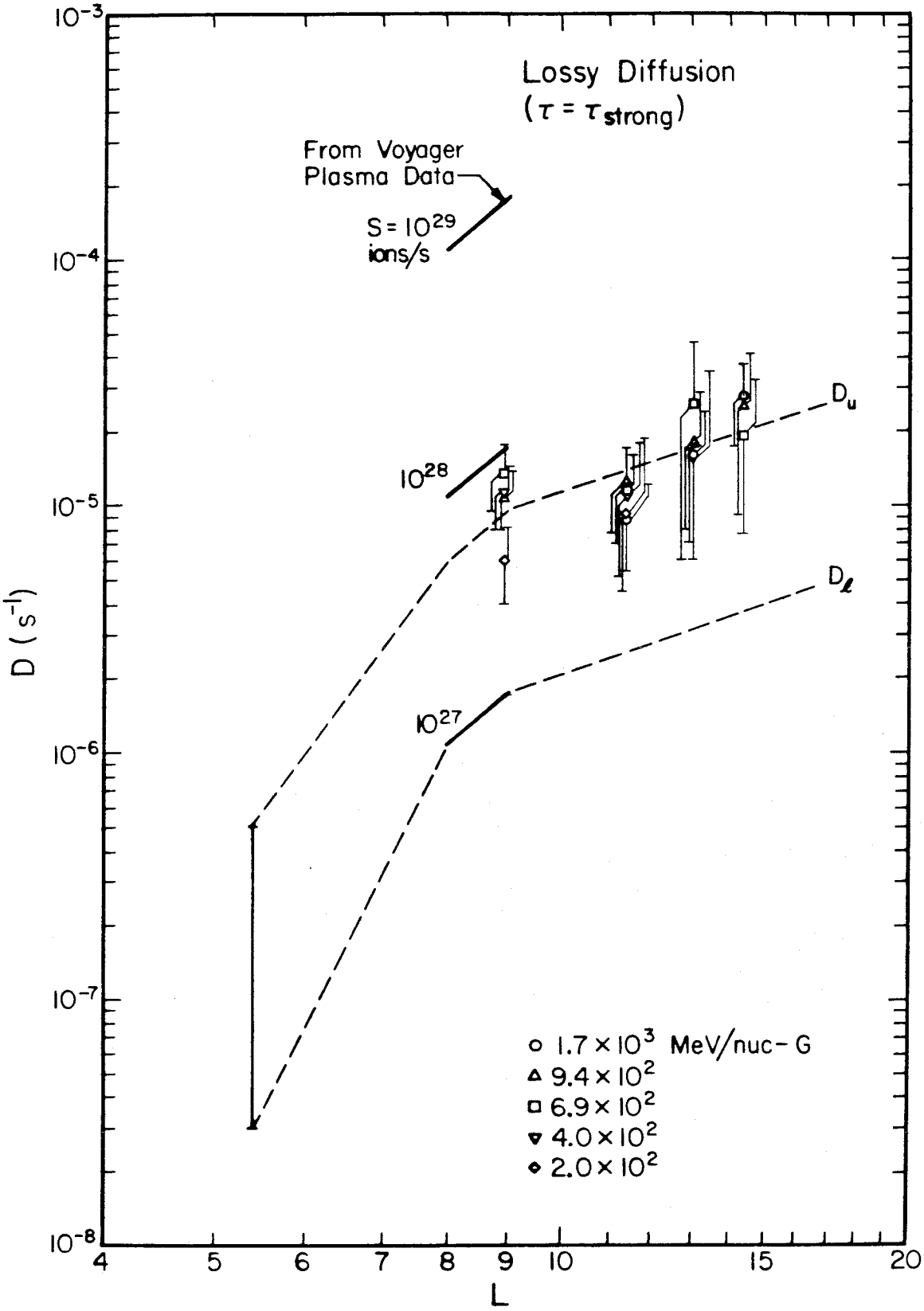
Lossy Diffusion
(τ = τ strong)
From Voyager
Plasma Data
S = 10^29
ions/s
10^28
10^27
D_u
D_ℓ
D (s^-1)
L
10^-3
10^-4
10^-5
10^-6
10^-7
10^-8
4
5
6
7
8
9
10
15
20
o 1.7 × 10^3 MeV/nuc-G
Δ 9.4 × 10^2
□ 6.9 × 10^2
▽ 4.0 × 10^2
◇ 2.0 × 10^2

radial positions for different values of M. The diffusion coefficient at a given radial position and the general radial dependence of D are seen to be the same within statistics for all magnetic moments. It is important to note that, since the diffusion coefficient was calculated using τ_{strong}, it represents an upper limit (assuming losses are caused by pitch-angle scattering). Also shown in the figure is the plasma diffusion coefficient of equation (4.3) between 8 and 9 R_J for S= 10^{27}, 10^{28}, and 10^{29} ions/s. A comparison of these lines and the upper limits obtained above indicate that the Io source strength of oxygen and sulfur ions is less than $\sim 10^{28}$ ions/s.

As discussed in Chapter 1, S is most likely greater than 10^{27} ions/s, which places a lower limit on the diffusion coefficient of approximately one tenth the value of the upper limit. This implies that the lifetime of the energetic oxygen ions between 8 and 17 R_J is within an order of magnitude of τ_{strong}. The range of diffusion coefficient that will be used in further analysis is represented by the dashed lines in Figure 4.2. The limits shown at 5.3 R_J were not determined from the energetic oxygen data, but represent the range of values determined from energetic proton and electron measurements (Goertz *et al.*, 1979; Thomsen *et al.*, 1977).

4.4 Diffusive Flow Rates

The diffusion coefficient limits shown in Figure 4.2 can now be used with measurements of the energetic oxygen number density and phase space density gradient to determine the inward flow rate. The diffusive flow, I, of ions with magnetic moment greater than M across radius r is given by

$$I_{>M} = n_{>M} \cdot 2\pi r \cdot 2h \cdot v_D \cdot R_J^3 \quad \text{ions/s} \qquad (4.8)$$

where $n_{>M}$ is the number density (cm^{-3}) of oxygen ions with magnetic moment greater than M calculated from the measured spectra, h is the scale height (R_J) of the particle distribution relative to the magnetic equatorial plane, and v_D is the average radial diffusion velocity (R_J/s) given by $v_D = D \cdot (\frac{1}{f}\frac{\partial f}{\partial L})$ (see e.g. Schulz and Lanzerotti [1974]).

In a dipolar magnetic field, the value of h for a particle population with a constant pitch-angle distribution depends on radial distance, increasing with increasing r. The scale height calculated for the energetic oxygen pitch-angle distribution (Figure 3.7b) using the actual magnetic field measurements was found, however, to be approximately constant between 6 and 17 R_J, equal to ~3 R_J. This is due to the distortion of the magnetic field at larger radial distances caused by currents that flow in the plasma disk near the magnetic equatorial plane. The magnetic field strength increases more rapidly as one moves away from the plane than for a dipole field, and, therefore, at larger r, the scale height of the energetic particles is reduced.

Figure 4.3b shows values of $I_{>M}$ obtained from equation (4.8) for oxygen ions with magnetic moment greater than 4.0×10^2 and 1.7×10^3 MeV/nuc-G between 5.3 and 17 R_J. The error bars represent all uncertainties in Table 3.4 (except σ_γ), a 15% uncertainty in $\frac{1}{f}\frac{\partial f}{\partial L}$, and a 50% uncertainty in the relative values of D at different radial locations. (Larger uncertainties in D and $\frac{1}{f}\frac{\partial f}{\partial L}$ were used at 5.3 R_J.) An additional factor of 3 absolute uncertainty in D applies to all measurements. The charge density profile of the plasma in this region, measured by the plasma instrument on Voyager 1 [Bagenal and Sullivan, 1981], is shown

Figure 4.3

a) The charge density of the plasma in the inner magnetosphere as measured by the Voyager plasma instrument [Bagenal and Sullivan, 1981]. b) The inward flow rate of energetic oxygen ions of magnetic moment greater than 4.0×10^2 and 1.7×10^3 MeV/nuc-G calculated using equation (4.8). In addition to the uncertainties shown in the figure (discussed in the text) there is an absolute uncertainty of a factor of ~3 that applies to all measurements.

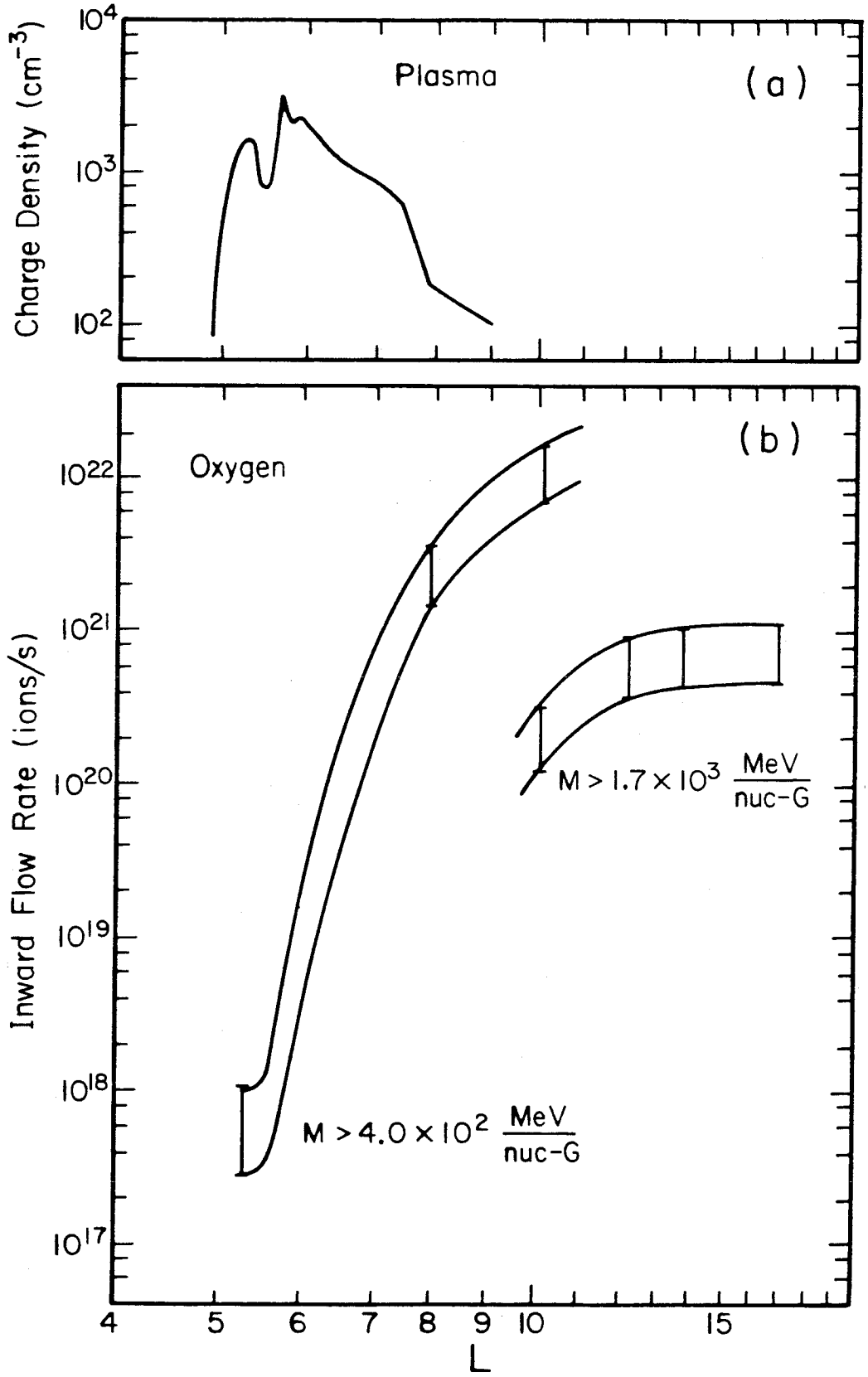
Charge Density (cm^{-3})
10^4
10^3
10^2
Plasma
(a)
Inward Flow Rate (ions/s)
10^{22}
10^{21}
10^{20}
10^{19}
10^{18}
10^{17}
Oxygen
(b)
$M > 1.7 \times 10^3$ MeV / nuc-G
$M > 4.0 \times 10^2$ MeV / nuc-G
4
5
6
7
8
9
10
15
L

for comparison in panel a and will be discussed in section 4.5.1.

It is evident from the figure that the total number of energetic oxygen ions flowing into the inner magnetosphere is small ($\lesssim 10^{23}$ ions/s at 10 R_J for M=4.0x10^2 MeV/nuc-G) compared with Io's source strength of $10^{27}-10^{28}$ ions/s. Another observation is that almost all of the ions flowing into this region are lost between 6 and 12 R_J. The region with the largest losses in terms of total number of particles is 8 to 12 R_J. The profile of the inward flow rate for M>4.0x10^2 MeV/nuc-G ions between 5.3 and 5.6 R_J is drawn approximately flat to indicate that the losses are most likely much less in this region than between 5.6 and 7.9 R_J.

An estimate of the average lifetime, τ, between 5.6 and 7.9 R_J can be obtained from the measured values of I using $\tau = -t / \log_e\left[I(5.6)/I(7.9)\right]$, where t is the time spent diffusing from 5.6 to 7.9 R_J. For $D \approx 10^{-6}\ s^{-1}$ and $\frac{1}{f}\frac{\partial f}{\partial L} \approx 2$, one finds $t \approx 1.2\text{x}10^6$ s and $\tau \approx 1.4\text{x}10^5$ s, to be compared with $\tau_{strong}(6.5\,R_J) = 1.4\text{x}10^4$ s. The average lifetime is therefore approximately an order of magnitude longer than the strong pitch-angle scattering lifetime in this region. Note that, even though there are relatively few particles lost outside 12 R_J, the lifetime is still close to τ_{strong} in this region. For instance, repeating the above calculation between 12.2 and 13.7 R_J for M>1.7x10^3 MeV/nuc-G ions gives $\tau \approx 1.7\text{x}10^6$ s compared with $\tau_{strong}(13\,R_J) = 3.5\text{x}10^5$ s. The reason fewer particles are lost in this region is that the ions are diffusing more rapidly (D is larger), the loss cone is smaller, and the bounce time is longer than at smaller radial distances.

Although the energetic ions that flow into the inner magnetosphere are small in number relative to the number of ions produced near Io, they do bring a significant amount of energy into the region as will be

discussed in section 4.6. It is therefore important to understand what the loss mechanism is in order to determine where the energy is delivered.

4.5 Particle Loss Mechanisms

It has been implicitly assumed in several previous sections of this thesis that the predominant loss mechanism for the energetic oxygen ions inside 20 R_J is pitch-angle scattering into the loss cone. In this section, the lifetime for several other possible loss mechanisms is estimated to see if they are significant in this region. The particular processes considered are geometric absorption by Io, absorption by micron-sized dust grains, and energy loss in the plasma of the inner magnetosphere. Energy-loss processes produce losses by shifting particle energies below analysis thresholds. They also represent real losses in the sense that energy is transferred from the particle to the medium. In order to calculate the energy loss in the plasma, information concerning the charge state of the energetic ions is needed, and therefore, charge state limits will also be determined. The observed losses indicate that the effective lifetime for the energetic ions is at most ten times the strong pitch-angle diffusion lifetime, so that calculated lifetimes for 1 MeV/nuc ions should be compared with ~9 days at 8 R_J ($10 \cdot \tau_{strong}$ for 128 MeV/nuc-G particles) and ~3 days at 6 R_J ($10 \cdot \tau_{strong}$ for 54 MeV/nuc-G particles).

4.5.1 Geometric Absorption by Io

In section 3.1 it was seen that the minima in the Z>2 rate near Io occurred at 5.6 R_J inbound and 5.4 R_J outbound, well inside Io's orbital

position of 5.9 R_J. The locations of the minima, which specify the inner edge of the lossy region, were found to be correlated with the locations of discontinuities in plasma density and wave activity. Figure 4.3 gives further evidence that the losses are not caused by Io. The total number of inflowing ions begins to decrease already at 12 R_J and falls steeply between 10 and 8 R_J. The plasma charge density profile, shown in panel a, indicates that the region of high plasma density extends well beyond the orbit of Io, to ~9 R_J. Also, significant wave activity was observed by the plasma wave instrument on Voyager 1 and 2 [Scarf *et al.*, 1979; Gurnett *et al.*, 1979; Scarf *et al.*, 1981] out to at least 20 R_J, with particularly intense activity between 5.6 and 10 R_J. It is therefore found once again that the lossy region is better correlated with regions of enhanced wave activity and plasma density than with the orbit of Io, and that certainly, since most of the energetic ions are lost between 12 and 8 R_J, Io does not absorb a significant fraction of the total oxygen energy flow into the inner magnetosphere.

4.5.2 Absorption by Dust

It is postulated that SO_2 dust grains of ~0.1 μm radius escape from Io's volcanic plumes into the Jovian magnetosphere [Johnson *et al.*, 1980]. The number density of the grains near Io is estimated to be $n_{dust} \approx 10^{-6}$ cm^{-3} [Morfill *et al.*, 1980]. Therefore, the collision lifetime, τ, of a particle of velocity v (=1.4x10^9 cm/s for E=1 MeV/nuc) in this regions is

$$\tau = \frac{1}{\sigma \, v \, n_{dust}} \approx 10 \text{ years} \qquad (4.9)$$

where σ is the cross-sectional area of a dust grain ($\sim 3 \times 10^{-10}$ cm^2). A 1 MeV/nuc oxygen ion can penetrate approximately ten grains before losing 100 keV/nuc, but the lifetime for collision with even one grain is so long that it is clear absorption by dust is an insignificant loss mechanism.

4.5.3 Oxygen Charge State

An estimate of the charge state of the energetic oxygen ions is needed to calculate the rate at which the ions lose energy in a plasma (section 4.5.4). The estimate is made assuming that the only process altering the charge state of the oxygen ions as they diffuse through the inner magnetosphere is electron-impact ionization due to free plasma electrons. Since ionization due to plasma ions and neutral gas in the region is not included, the calculated charge state represents a lower limit. It is also a lower limit because the assumption is made that the ions are singly ionized when they cross 10 R_J. If the energetic ions outside 10 R_J have the same charge state composition as the plasma ions in the hot torus, then they are a mix of O^+ and O^{++} [Bagenal and Sullivan, 1981].

An approximation made in the calculation is that the electron-capture cross sections are negligible compared with the ionization cross sections. The average charge state that an ion with velocity β (=v/c) acquires after undergoing a large number of interactions with a medium is given by

$$Z^* = Z\left[1 - \exp(-125\beta / Z^{2/3})\right] \qquad (4.10)$$

[Barkas, 1963] where Z is the nuclear charge, and represents the charge state at which ionization and electron-capture cross sections are equal.

Therefore, since $Z^* > 6$ for >1 MeV/nuc oxygen ions, electron capture can certainly be neglected for ions of charge state less than ~5.

The ionization lifetimes were calculated as a function of radius between 5.6 and 10 R_J using experimental and theoretical electron-impact ionization cross sections [Lotz, 1967] and electron densities inferred from plasma wave observations [Gurnett *et al.*, 1981]. The measured diffusion coefficient and phase space density gradient were used to determine the length of time the energetic ions spend at each radial distance. The resulting ionization state lower limit for 400 MeV/nuc-G oxygen ions is shown in Figure 4.4a as a function of position. Since the calculation was performed using average ionization lifetimes, the figure represents the average position at which a given ionization state occurs. The results indicate that the plasma is dense enough in the inner magnetosphere to strip the energetic ions of most of their electrons.

The oxygen gyrofrequency, which is a parameter of importance for studies of wave-particle interactions, is shown in Figure 4.4b for 400 MeV/nuc-G ions with charge states given by panel a. Particle gyrofrequencies are proportional to QB, where Q is their charge state, and therefore the increase seen in the figure between 10 and 5 R_J is due both to increasing magnetic field strength and charge state.

4.5.4 Energy Loss in Plasma

Figure 4.4a shows that the oxygen charge state is at least Q=4 in the region of the plasma torus, and therefore, in order to determine an upper limit to the energy loss of the energetic ions in the plasma of the inner magnetosphere, it will be assumed that the ions have reached their equilibrium charge state, $Q=Z^*$. Again ions with 1 MeV/nuc are

Figure 4.4

a) The calculated lower limit of the oxygen ionization state as a function of radial distance from Jupiter. The values plotted represent the average distance at which a given ionization state is reached. The approximation was made in the calculation that the only process affecting the oxygen charge state is electron-impact ionization due to free electrons in the plasma of the inner magnetosphere. It was assumed that the oxygen ions entering the region are singly ionized.

b) The oxygen gyrofrequency for ions with the ionization state shown in panel a. A dipolar magnetic field was assumed.

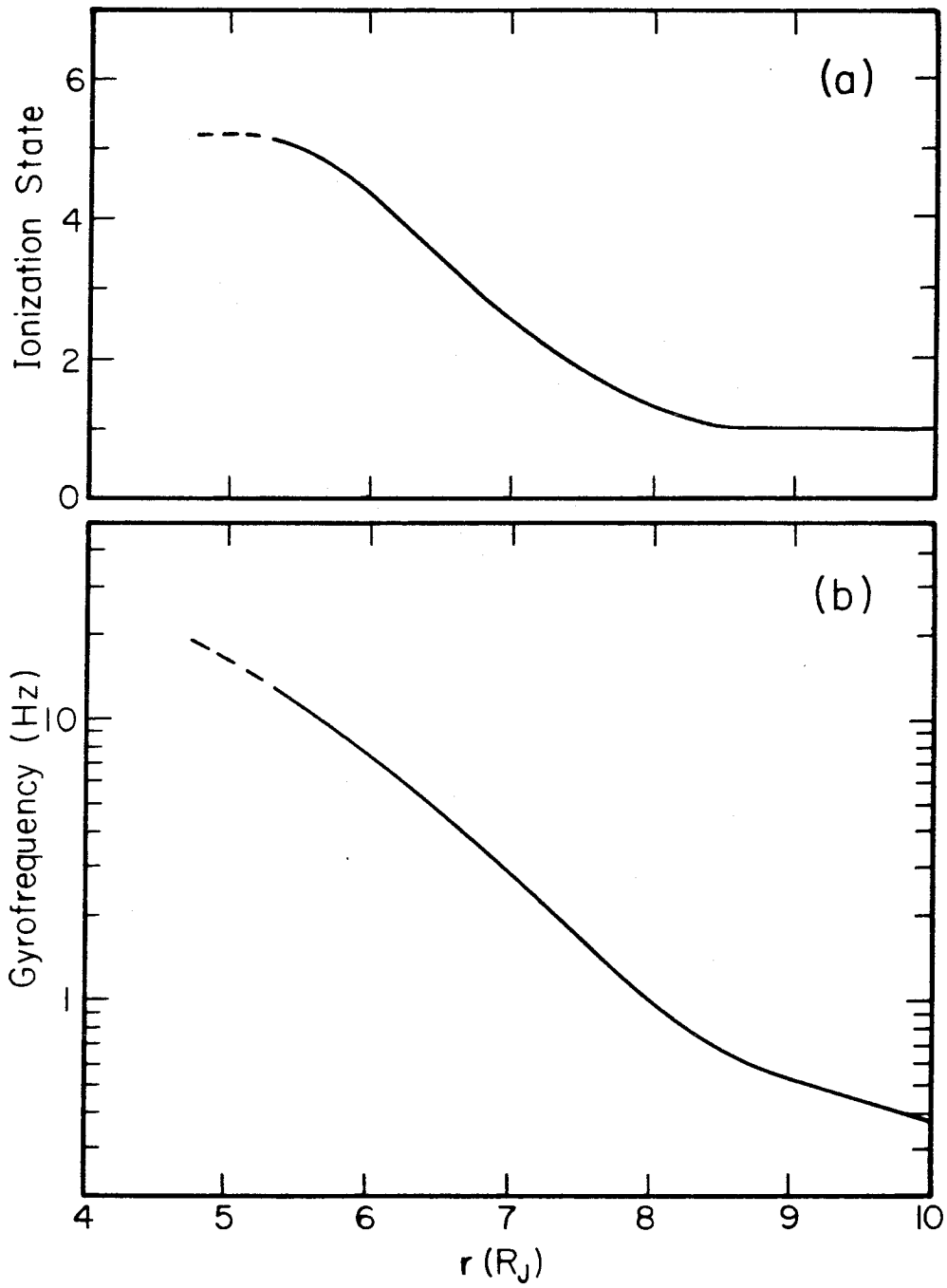
(a)
Ionization State
0
2
4
6
(b)
Gyrofrequency (Hz)
1
10
4
5
6
7
8
9
10
r (R_J)

considered (the energy loss is less for higher energies), so that Q≈6 (4.10). The equation for the energy loss in a plasma is

$$\frac{dE}{dx} = -2.4\text{x}10^{-22}\,\frac{n_e}{E}\,\frac{Q^2}{A}\left\{\log_e\left[\frac{T_e^{\,3}}{n_e Q^2}\right]^{1/2} + 9.13\right\} \qquad (4.11)$$

(see e.g. Gloeckler *et al.* [1975]) where E is in MeV/nuc, x is the path length (cm), n_e is the electron density (cm^{-3}), and T_e is the electron temperature (°K). Two regions will be considered; one near 8 R_J where $n_e \approx 10^2$ cm^{-3} [Warwick *et al.*, 1979] and $T_e \approx 4\text{x}10^5$ K [Scudder *et al.*, 1981], and one near 6 R_J (in the hot torus) where $n_e \approx 2\text{x}10^3$ cm^{-3} and $T_e \approx 10^5$ K (same references). Using equation (4.11) with the above assumptions and measurements gives a lower limit to the time for a 1 MeV/nuc oxygen ion to lose 0.1 MeV/nuc near 8 R_J of ~2 years compared with $10 \cdot \tau_{strong} \approx 9$ days. In the hot torus, the lower limit is ~35 days compared with $10 \cdot \tau_{strong} \approx 3$ days. Therefore, it is clear that the energetic ions do not lose a significant amount of their energy to the plasma in the inner magnetosphere.

It has been shown in this section that the observed losses of the energetic ions inside 12 R_J can not be explained by geometric absorption by Io, absorption by dust, or energy loss in plasma. Hence, it is assumed that pitch-angle scattering into the loss cone is the dominant loss mechanism in this region.

4.6 Energy Flow Rates

The ultimate sink of particles that are pitch-angle scattered into the loss cone is the Jovian atmosphere. The total power that the energetic oxygen and sulfur ions deliver to the atmosphere will now be

calculated and compared with the power required to excite the aurora.

The energy flow rate, or power, P, delivered by energetic oxygen ions with magnetic moment greater than M across radius r is given by

$$P_{>M} = \rho_{>M} \cdot 2\pi r \cdot 2h \cdot v_D \cdot R_J^3 \quad W \tag{4.12}$$

where $\rho_{>M}$ is the energy density of the oxygen ions (joules/ cm^3), and the other quantities are defined following equation (4.8). In order to calculate $P_{>M}$ at as low a magnetic moment as possible and still be outside the region in which most particles are lost, we have determined $P_{>M}$ at 10.1 R_J. The quantity $\rho_{>M}$ was calculated from the 10.1 R_J spectrum in Figure 3.8, using the dash-dotted portion of the spectrum for magnetic moments less than 4.0×10^2 MeV/nuc-G. As discussed in section 3.5.3, the shape of this extrapolated curve was derived from the energy per charge spectrum, at the same M, measured by LECP at ~16 R_J [Hamilton *et al.*, 1981].

Figure 4.5 shows the values of $P_{>M}(10.1\,R_J)$ calculated with equation (4.12) for several magnetic moment thresholds. The open symbols represent measurements based on the extrapolated portion of the spectrum. The uncertainties included in the error bars are those due to uncertainties in abundance, event number, $\frac{1}{f}\frac{\partial f}{\partial L}$, and D. The uncertainty in the value of D at 10.1 R_J for different magnetic moments was estimated to be 50% (see Figure 4.2). An additional factor of 3 absolute uncertainty in D applies to all measurements. The power due to sulfur ions is represented by the X symbols in Figure 4.5, and was determined from the oxygen $P_{>M}$ values using the S/O ratios in Figure 3.5 and the relationship between the oxygen and sulfur spectral shapes ($\gamma_S = \gamma_O + 0.2$) implied by that figure. The sulfur power is approximately equal to the oxygen power

Figure 4.5

The inward energy flow rate across 10 R_J due to oxygen and sulfur ions with magnetic moments greater than M; calculated using equation (4.12). The oxygen energy density at 10 R_J used in the calculation was determined from the 10.1 R_J spectrum in Figure 3.8. The points with open circles were obtained using the extrapolated portion of the spectrum derived from LECP measurements. The energy flow rate due to sulfur ions was determined from the oxygen values using the sulfur to oxygen ratio in Figure 3.5 and the relationship between the oxygen and sulfur spectral shapes ($\gamma_S = \gamma_O + 0.2$) implied by that figure. The energy flow rate across 10 R_J is approximately the power delivered to the Jovian atmosphere by ions lost between 10 and 8 R_J. The dotted curve represents the power delivered to the atmosphere by all oxygen and sulfur ions lost from the magnetosphere inside 12 R_J. Also shown is the power required to produce the observed ultraviolet auroral emissions [Broadfoot *et al.*, 1981].

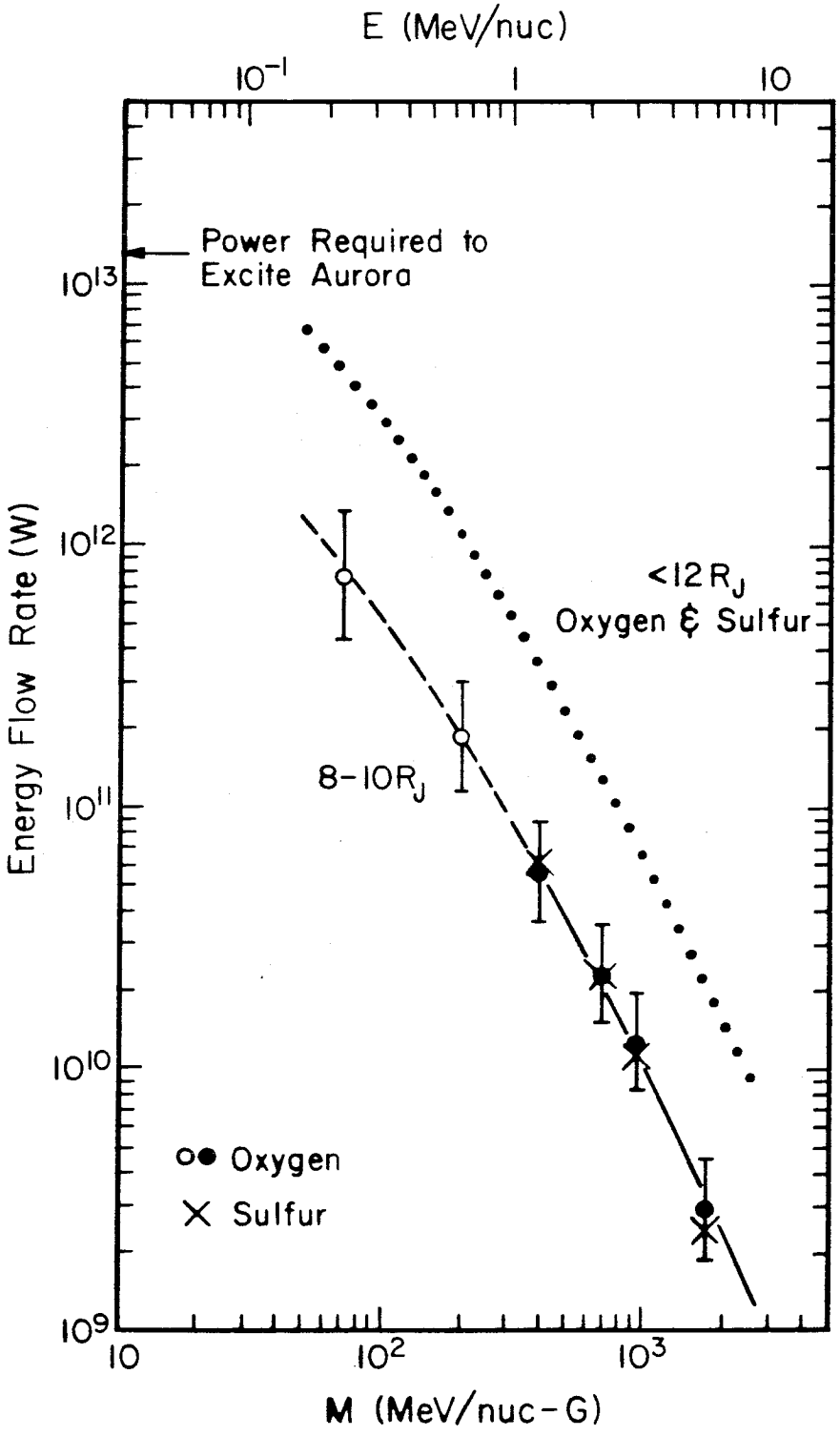
E (MeV/nuc)
10⁻¹
1
10
Power Required to Excite Aurora
10¹³
10¹²
10¹¹
10¹⁰
10⁹
Energy Flow Rate (W)
<12 R_J
Oxygen & Sulfur
8-10R_J
Oxygen
Sulfur
10
10²
10³
M (MeV/nuc-G)

due to the fact that the sulfur ions are approximately half as abundant as oxygen ions, but have twice as much total energy (twice as many nucleons) at a given magnetic moment.

The inward energy flow across 10 R_J due to >70 MeV/nuc-G oxygen and sulfur ions is seen to be $\sim 1.5 \times 10^{12}$ W. An interesting number to compare this with is the total outward energy flow due to the plasma ions. The number of plasma oxygen and sulfur ions diffusing outward across 10 R_J is $\sim 5 \times 10^{27}$ ions/s, and their average total energy is approximately the corotation energy of an ion with mass 21 amu (the mean atomic mass of the dissociation products of SO_2) which is 1.7 keV. The outward energy flow is therefore $\sim 1.4 \times 10^{12}$ W. Hence, the inward flow of >70 MeV/nuc-G oxygen and sulfur ions is comparable to the outward energy flow of the plasma ions. The energetic oxygen and sulfur inward energy flow increases toward lower magnetic moments, so that, including the lower energy ions and the energetic protons and electrons that also diffuse inward in this region, there is a substantial net energy flow into the inner magnetosphere.

Since most of the ions crossing 10 R_J are lost before reaching 8 R_J (Figure 4.3), the energy flow rate shown in the Figure 4.5 is, to first order, the power delivered to the atmosphere by ions lost between 10 and ~8 R_J. However, ions gain energy as they diffuse inward, so that the power from inside 8 R_J is not necessarily negligible. An estimate of the ratio of the energy flow crossing 8 R_J to that crossing 10 R_J is given by

$$\frac{P_{>M}(8\,R_J)}{P_{>M}(10\,R_J)} \approx \frac{I_{>M}(8\,R_J)}{I_{>M}(10\,R_J)} \frac{\bar{E}(8\,R_J)}{\bar{E}(10\,R_J)} \qquad (4.13)$$

where $\bar{E}(r) \propto M \cdot B(r)$ is the average energy of ions with magnetic moment greater than M. Based on the inward flow rates of $>4.0 \times 10^2$ MeV/nuc-G

oxygen ions in Figure 4.3 and the measured magnetic field strengths at 8 and 10 R_J, $P_{>M}(8R_J)/P_{>M}(10R_J) \approx 0.5$. The ion flow rate drops off steeply inside 8 R_J, implying that most of the power, $P_{>M}(8R_J)$, is delivered to the atmosphere by ions lost between ~7.5 and 8 R_J, and that a relatively small amount is delivered from inside ~7.5 R_J. Similarly for 12 R_J, based on the inward flow rate of $>1.7 \times 10^3$ MeV/nuc-G ions in Figure 4.3, $P_{>M}(12R_J)/P_{>M}(10R_J) \approx 1.5$. Outside 12 R_J losses are small. Hence, it is estimated that the total power delivered by sulfur and oxygen ions inside ~12 R_J to the atmosphere is a factor of $6 = 2 \times (1+1.5+0.5)$ larger than the oxygen energy flow rate across 10 R_J. This power is shown as the dotted curve in Figure 4.5.

As discussed in Chapter 1, the most energetic phenomenon related to the inner magnetosphere is the aurora. The extreme ultraviolet auroral emission observed by the Voyager ultraviolet spectrometer requires a continuous power input of 1.2×10^{13} W into the auroral zone [Broadfoot *et al.*, 1981]. This number is likely a lower limit because it was calculated assuming that all emission occurred high enough in the atmosphere to neglect extinction, whereas there is evidence that some of the emission originates deeper in the atmosphere where extinction is non-negligible [D. Shemansky, private communication]. The measurements shown in Figure 4.5 indicate that, if the required power is not substantially greater than 1.2×10^{13} W, oxygen and sulfur ions with energies of ~100 keV/nuc are contributing a reasonable fraction of it. The figure also shows that lower energy ions are likely depositing additional power. As seen above, the bulk of the power delivered by the energetic oxygen and sulfur ions comes from ions lost between ~7.5 and ~12.5 R_J, which, using the Voyager magnetic field models of Connerney *et*

al. [1981], maps into a latitudinal zone in the atmosphere of ~67° – ~71°. This is consistent with the observed auroral zone width of roughly 5° (see Chapter 1), and is within the range of latitudes at which aurorae are seen [Broadfoot *et al.*, 1981].

As a final point, we note that the atmospheric penetration depths of heavy ions and electrons of equal energies are quite different as illustrated in Figure 4.6. Therefore, further analysis of the depth structure of the optical and ultraviolet auroral emission may help distinguish between excitation caused by electrons lost from the torus, and that caused by energetic oxygen and sulfur ions lost between 7.5 and 12.5 R_J.

Figure 4.6

The column depth of penetration of electrons, protons, oxygen ions, and sulfur ions in H_2 (the most abundant species in the upper Jovian atmosphere), as a function of their incident energies, assuming the particles are incident normal to the atmosphere. The electron curve represents the extrapolated range given by

$$R = \frac{A}{Z}\frac{13}{27} 412\ E^{1.265-0.0954\log_e E}$$

[Koral and Cohen, 1965]. The proton, oxygen, and sulfur curves were calculated using the range-energy tables of Northcliffe and Schilling [1970].

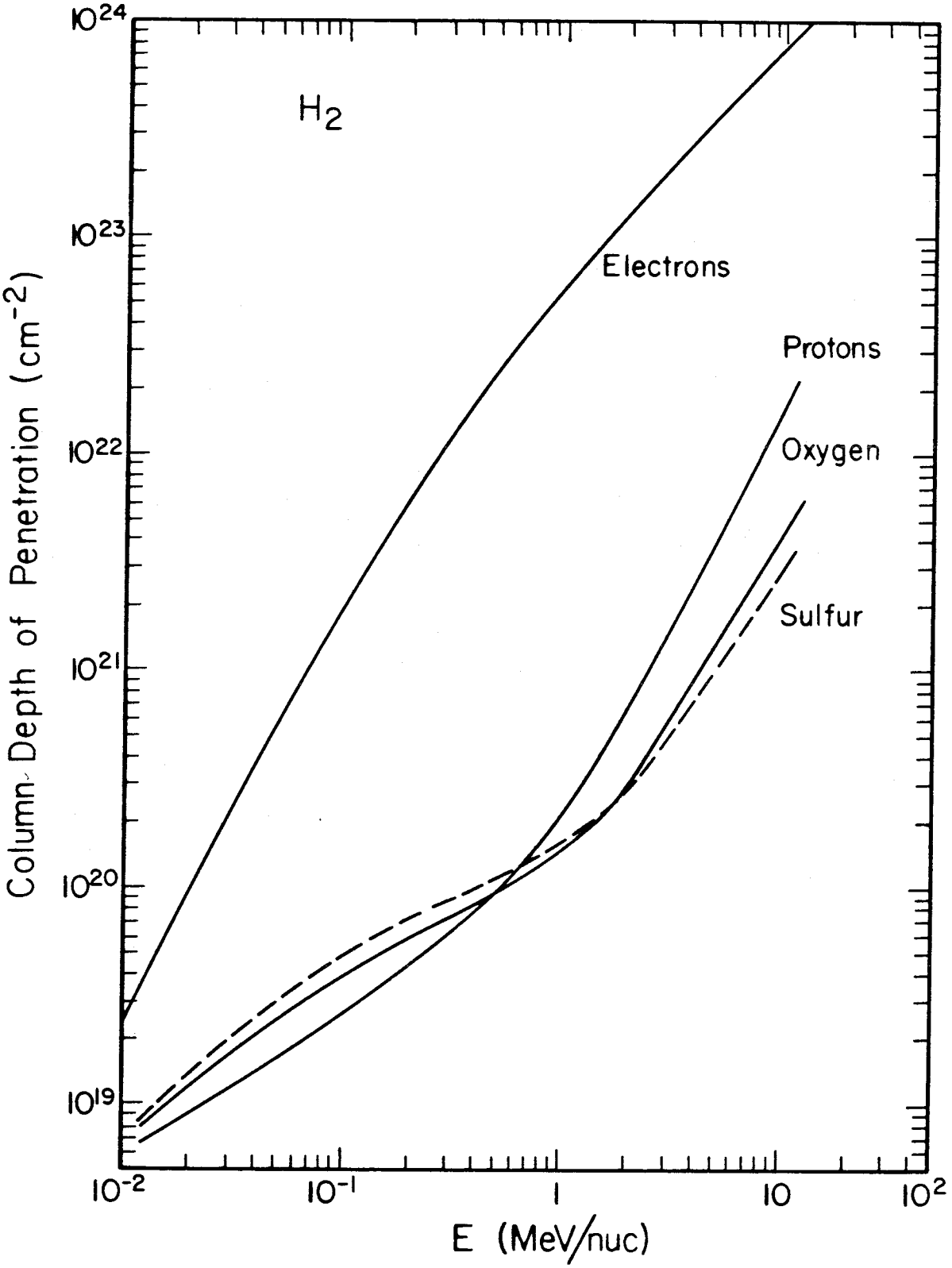
H_2
Electrons
Protons
Oxygen
Sulfur
Column Depth of Penetration (cm^{-2})
10^{24}
10^{23}
10^{22}
10^{21}
10^{20}
10^{19}
10^{-2}
10^{-1}
1
10
10^{2}
E (MeV/nuc)

Chapter 5

Conclusions

The principal conclusions of this study of Z>2 ions with energies in the range 1 to 20 MeV/nuc between 5 and 20 R_J in the Jovian magnetosphere are as follows:

1) The elemental abundances of carbon, sodium, and sulfur relative to oxygen vary as a function of particle magnetic moment, M ($\propto p_\perp^2/B$), but are to first order the same throughout the magnetosphere at a given M. For 10^3 MeV/nuc-G ions (E≈4 MeV/nuc at 10 R_J) the following abundance ratios are found: S/O=0.5, C/O=0.1, and Na/O≈0.05. The sulfur to oxygen and sodium to oxygen ratios increase toward smaller M implying that the sulfur and sodium energy spectra are softer than that of oxygen, whereas the carbon to oxygen ratio decreases toward smaller M implying a harder carbon spectrum than that of oxygen.

2) Between 6 and 17 R_J, there is a positive radial gradient in the phase space density of energetic oxygen ions with magnetic moments in the range $2x10^2$ to $2x10^3$ MeV/nuc-G. The diffusive flow of the energetic ions is therefore inward in this region.

3) The diffusion coefficient upper limit at 9 R_J is $\sim10^{-5}$ s^{-1}. This limit, combined with the analysis of Voyager plasma observations by Siscoe *et al.* [1981], specifies an upper limit to the mass loading rate near Io of $\sim10^{28}$ ions/s.

4) A substantial fraction of the energetic oxygen ions are lost as they diffuse from 17 to 6 R_J, with the largest total number of particles lost between 8 and 12 R_J. The particle lifetime throughout the region is

within an order of magnitude of the strong pitch-angle diffusion lifetime. The location of the maximum losses (8-12 R_J) indicates that geometric absorption by Io (5.9 R_J) is not the primary loss mechanism for energetic oxygen ions. Also, order of magnitude estimates show that absorption by dust grains and energy loss in the plasma of the inner magnetosphere can not produce the observed losses. The loss mechanism is therefore postulated to be pitch-angle scattering into the loss cone.

5) The total number of >70 MeV/nuc-G oxygen and sulfur ions diffusing inward across 10 R_J is $\sim 10^{24}$ ion/s. This is a small number compared with Io's source strength of $10^{27} - 10^{28}$ ions/s. The energy flow inward across 10 R_J due to the same energetic ions, however, is $\sim 10^{12}$ W, which is approximately equal to the total outward energy flow at 10 R_J due to plasma ions. The energetic oxygen and sulfur inward energy flow increases toward lower magnetic moments, so that, including the lower energy ions and the energetic protons and electrons that also diffuse inward, there is a substantial net energy flow into the inner magnetosphere.

6) The energetic oxygen and sulfur ions that are scattered into the loss cone during the diffusion process deposit their energy in the Jovian atmosphere. Based on the observed losses between 6 and 17 R_J, it is estimated that oxygen and sulfur ions with magnetic moments greater than 70 MeV/nuc-G ($E \gtrsim 0.3$ MeV/nuc at 10 R_J) deliver $\sim 5 \times 10^{12}$ W to the Jovian atmosphere; a power comparable to the $\sim 1.2 \times 10^{13}$ W required to produce the observed ultraviolet auroral emission. Additional power is likely contributed by oxygen and sulfur ions with magnetic moments less than 70 MeV/nuc-G. Since most of the particles are lost between 7.5 and

12.5 R_J, the latitudinal zone in which the most energy is deposited in the atmosphere is ~67° to ~71°.

Appendix A

Definition of Terms

Brief definitions of several magnetospheric terms used in this thesis are given below. More details can be found in Roederer [1970] and in Schulz and Lanzerotti [1974].

bow shock – the shock-wave surface on the sunward side of the magnetopause where the solar wind changes from a supersonic to a subsonic plasma.

loss cone – the cone formed at any point along a magnetic field line by rotating a line at angle α_l with respect to the field line about the field line. The angle α_l is defined such that all particles with pitch angles less than α_l will propagate far enough along the field line to encounter Jupiter's atmosphere before mirroring back toward the magnetic equatorial plane. The particles that encounter the atmosphere are absorbed and therefore lost from the magnetosphere. At 10 R_J, the loss cone at the magnetic equatorial plane has $\alpha_l \approx 1°$.

magnetopause – the surface that bounds the magnetosphere, separating the domain of the interplanetry magnetic field and plasma from that of the Jovian magnetic field.

magnetosphere – the region of space in which Jupiter's magnetic field is dominant.

McIlwain L parameter (or simply L parameter) – a coordinate often used in magnetospheric physics to order observations of trapped

particles. Defined for a dipolar magnetic field as the distance from the center of the dipole that a particle's guiding center field line crosses the magnetic equatorial plane. L is defined in units of R_J, and is therefore dimensionless. In this thesis, L values were assigned only to observations made at or near the magnetic equatorial plane, and were therefore defined as the spacecraft - dipole center distance. (Jupiter's dipole center is offset ~0.1 R_J from the planet's center of mass).

phase space density – the particle density in coordinate - momentum space (six dimensions).

pitch angle – the angle between a particle's momentum vector and the magnetic field direction (i.e., pitch angles of 0° or 180° imply field-aligned flow).

zenocentric – with respect to Jupiter's center of mass. zeno- comes from Zeus. A table of the commonly used prefix and genitive forms of the planetary names is in Allen [1973, p.139].

Appendix B

High Counting Rate Calibrations

The high radiation levels of Jupiter's inner magnetosphere cause several instrumental problems in the LET system for which corrections must be made before absolute particle fluxes and energies can be determined. These include discriminator threshold changes due to baseline shifts at the output of the detector amplifiers, discriminator deadtime effects, and pulse pileup effects. In order to correct for the deadtime and threshold effects, a spare CRS instrument was calibrated using light pulses from randomly triggered light emitting diodes to simulate the ionization energy loss of charged particles in the detectors. The calibration and its results are described in detail elsewhere [Gehrels, 1981]. This appendix summarizes the calibration results that are relevant to the present study and describes the pulse pileup effect.

B.1 Discriminator Deadtimes

Finite retrigger times for discriminator circuits cause a dead time in the instrument response that results in observed rates that are lower than the true rates. For the CRS instrument, the effect becomes noticeable above rates of $\sim 10^3$ s^{-1} and significant above rates of 10^4 s^{-1}.

The standard livetime correction formula for rate R is

$$R_{true} = \frac{R_{observed}}{(1 - \tau R_{observed})} \qquad (B.1)$$

where τ is the retrigger time of the discriminators, often assumed to be a constant. During the calibration it was determined, however, that, for the Z>2 rate and the detector singles rates, τ is a function of both the

rate and pulse height of the particles exceeding the discriminator threshold. It was therefore necessary to measure τ, or equivalently $R_{observed}$ as a function of R_{true}, for all rates and conditions of interest.

In Table B.1, measurements of $Z>2_{obs}$ as a function of $Z>2_{true}$ are listed for 15, 30, and 90 MeV pulses in L1. In Figure 2.5 it is seen that 15 MeV pulses are typical of those exceeding the Z>2 discriminator threshold outside of Io's orbit, and 30 and 90 MeV correspond to oxygen and sulfur events respectively, inside Io's orbit. Although not shown in the figure, the L1 pulse-height histogram at ~8 R_J has a single maximum at 30 MeV. The Z>2 livetime correction listed in Table 3.2 is the ratio $Z>2_{true} / Z>2_{obs}$ for the observed L1 pulse-height distribution in each region.

The livetime correction formula for a coincidence rate such as LZ3 is approximately given by

$$LZ3_{true} = \frac{LZ3_{obs}}{(1 - \tau_1 R_{L1})(1 - \tau_2 R_{L2})(1 - \tau_3 R_{L3})(1 - \tau_{Z>2} R_{Z>2})} \qquad (B.2)$$

where R_i and τ_i are the singles rate and retrigger time of detector Li, and $R_{Z>2}$ and $\tau_{Z>2}$ are the Z>2 discriminator rate and retrigger time. Equation (B.2) is exact only in high flux environments where all of these rates are much larger than the observed coincidence rate. During the calibration, the livetime correction factor, $\lambda_i = 1/(1-\tau_i R_i)$, for each discriminator in the LZ3 coincidence equation (L1·L2·L3 command state; L4 off) was measured for the case where the particles of interest are oxygen and sulfur nuclei (large pulses) and the predominant events are protons (small pulses).

Figure B.1 shows fits to the measured λ_1 for 30 MeV (oxygen) and 90 MeV (sulfur) pulses as a function of the rate, R_1, of ~1 MeV (proton)

Table B.1

Observed vs True Z>2 Rate
for Several L1 Pulse Heights †

$Z>2_{true}$	$Z>2_{obs}$		
	E1=15 MeV	E1=30 MeV	E1=90 MeV
$(10^3\ s^{-1})$	$(10^3\ s^{-1})$	$(10^3\ s^{-1})$	$(10^3\ s^{-1})$
5	4.7	4.7	4.7
7	6.5	6.5	6.3
10	8.9	8.8±0.2¶	8.6
15	12.6	12.3	11.6
20	15.9	15.5	14.0
25	18.8	18.3	15.8
30	20.3	21.0±1.0	17.5

† E2=0, E3=0.

¶ Typical standard deviation of the measured $Z>2_{obs}$ in LET A, B, C, and D.

Figure B.1

Fits to the measured L1 livetime correction factor, λ_1, for the LZ3 rate for 30 Mev (oxygen) and 90 MeV (sulfur) pulses as a function of the rate, R_1, of ~1 MeV (proton) pulses. The error bars at the end of the curves represent the typical spread in the data about the fit. Also shown are lines of constant of constant τ_1 in the equation $\lambda_1 = 1/(1-\tau_1 R_1)$.

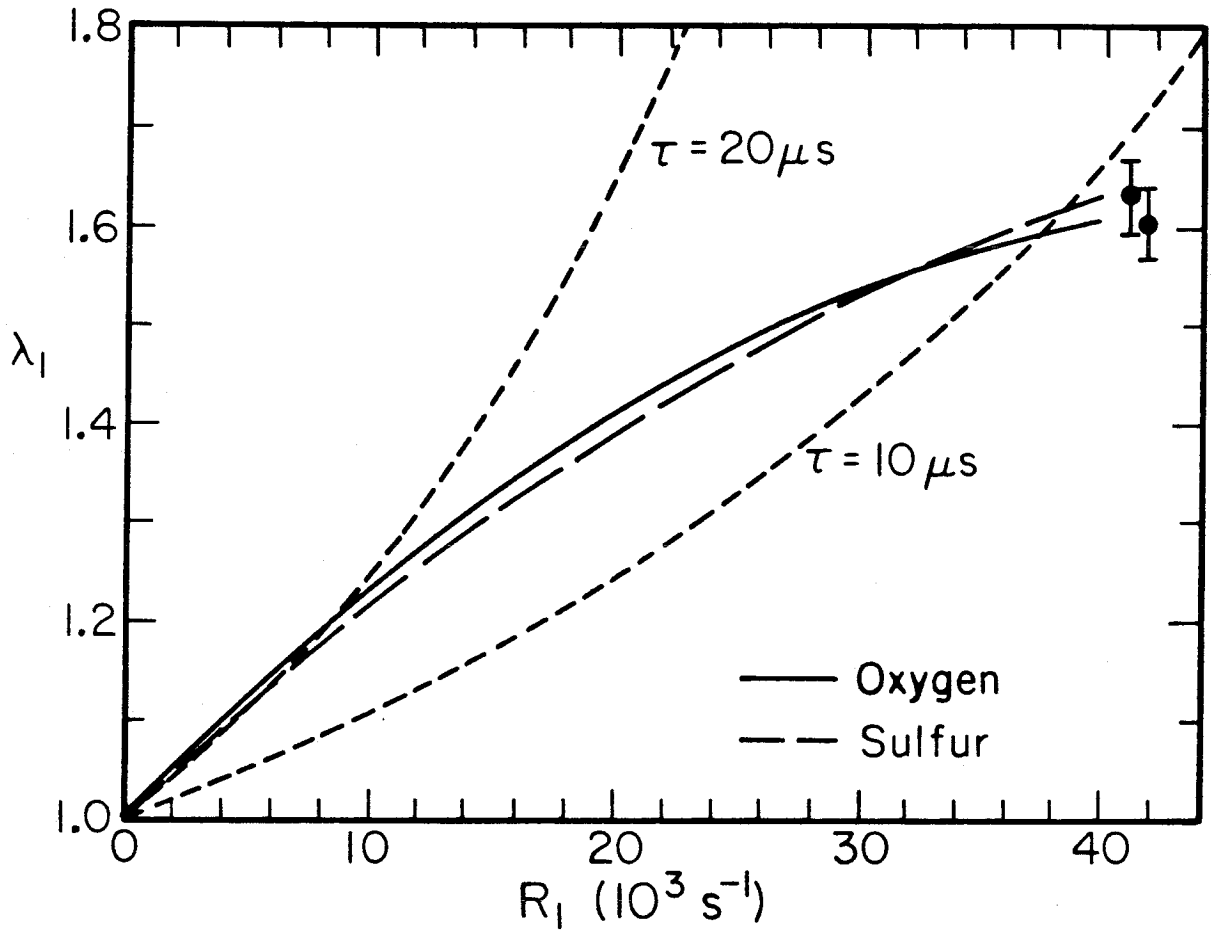
1.8
1.6
1.4
1.2
1.0
λ_1
$\tau = 20\mu s$
$\tau = 10\mu s$
Oxygen
Sulfur
0
10
20
30
40
R_1 (10^3 s^{-1})

pulses. The error bars indicate the typical spread in the data about the fit, and the dashed lines are lines of constant τ_1. The oxygen and sulfur curves are seen to be the same to within the measurement uncertainty, so that, for a given R_1, the same L1 correction factor will be applied to both event types. The results deviate significantly from lines of constant τ, indicating the importance of directly measuring the correction factors.

The measured λ_2 and λ_3 for the above case were found to be consistent with $\lambda_2 = \lambda_3 = 1.0$ to within ~2% for all L2 and L3 rates. This is due primarily to the fact that the LETs use a strobed coincidence logic triggered by L1 (see e.g. Gehrels [1981]). An event that exceeds the L1 threshold and produces a strobe is counted in the LZ3 rate if it either triggers the L2 and L3 discriminators itself or comes at a time when these discriminators are up from a previous event. Hence, the L2 and L3 discriminators cause very little deadtime in the LZ3 rate. It was also determined that $\lambda_{Z>2} \approx 1.0$, due both to the above effect and to the fact that approximately half of the events that exceed the Z>2 discriminator also cause an L1 singles rate count and are therefore already included in the λ_1 correction. With these measurements and considerations, equation (B.2) simplifies to

$$LZ3_{true} = \lambda_1(R_1)\ LZ3_{observed}\ . \qquad (B.3)$$

The values of λ_1 in the regions used in the analysis are listed in Table 3.2 (the LZ3 livetime correction).

B.2 Discriminator Threshold Shifts

High counting rates cause negative shifts in the baseline voltage level at the output of the detector amplifiers. Since discriminator

thresholds are set for a specified level above the nominal baseline, the baseline shift produces an increase in the effective threshold, so that, for instance, at high counting rates it takes a larger energy deposit to exceed a given threshold than at low counting rates. During the calibration, the shift in the L1 Z>2 threshold was measured as a function of the L1 pulse height and Z>2 rate. The effective carbon, oxygen, and sulfur Z>2 thresholds, E_{t-eff}, including energy loss in the window, were then calculated from the measured thresholds and are listed in Table B.2. The effective oxygen thresholds used in the analysis are listed in Table 3.2

B.3 Pulse pileup

As fluxes increase, the probability that two particles are coincident in a detector within the instrumental resolving time increases, degrading the pulse-height data from that detector. For large oxygen pulses in the detector, the effect of a high rate of coincident small proton pulses is to broaden the oxygen pulse-height distribution. Oxygen events in coincidence with other large pulses, however, will be displaced completely out of the normal oxygen distribution. The fraction displaced is τ_{pha} $Z>2_{true}$, where τ_{pha} is the effective resolving time for pulse-height analysis (~20 μs). In all regions, particles stopping in L3 were analyzed using only their L2 and L3 pulse-height information. The maximum counting rate of large oxygen and sulfur pulses in these two detectors is on the order of 10^3 s^{-1} (L2 near Io), so that pulse pileup affects <2% of the Z>2 particles stopping in L3. In the 4.9, 5.3, and 5.9 R_J regions however, particles stopping in L2 were used to calculate the lower energy portions of the spectra, and for these events the L1 pulse height is

Table B.2

Effective Z>2 Discriminator Thresholds

$Z>2_{obs}$ (10^3 s^{-1})	Pulse Height (MeV)	$E_{t\text{-}eff}$ ¶ Carbon (MeV/nuc)	Oxygen (MeV/nuc)	Sulfur (MeV/nuc)
6.6	7.5	1.2	1.1	0.9
11.6	7.5	1.3	1.1	0.9
19.7	7.5	1.3	1.1	0.9
6.6	15.4	1.3	1.1	0.9
11.6	15.4	1.4	1.2	0.9
19.7	15.4	1.5	1.3	1.0
6.6	30.8	1.3	1.2	0.9
11.6	30.8	1.5	1.3	1.0
19.7	30.8	1.7	1.4	1.1
6.6	92.3	1.4	1.2	1.0
11.6	92.3	1.7	1.4	1.1

¶ The nominal thresholds for carbon, oxygen, and sulfur are 1.2, 1.1, and 0.9 MeV/nuc respectively.

required for elemental identification. The counting rate of large pulses in L1 is $Z>2_{true}$, which is $\sim 1.5 \times 10^4$ s^{-1} in these regions, so that pulse pileup affects approximately 30% of the Z>2 events. A more precise estimate of the amount of pulse pileup in each region can be determined from the data by comparing the energy spectrum of particles stopping in L3 obtained using L1 in the elemental identification process with one in which only L2 and L3 were used. The ratio between the resulting spectra is energy independent over the three-detector energy range and indicates the fraction of the events in L1 displaced out of the oxygen distribution. The ratio was therefore used as the pulse pileup correction factor for the two-detector part of the spectrum.

References

Allen, C. W., *Astrophysical Quantities*, 3rd edition, The Athlone Press, London, 1973.

Armstrong, T. P., M. T. Paonessa, S. T. Brandon, S. M. Krimigis, and L. J. Lanzerotti, Low energy charged particle observations in the 5-20 region of the Jovian magnetosphere, *J. Geophys. Res.*, *86*, September, 1981.

Bagenal, F. and J. D. Sullivan, Direct plasma measurements in the Io torus and inner magnetosphere of Jupiter, *J. Geophys. Res.*, *86*, September, 1981.

Baker, D. N. and C. K. Goertz, Radial diffusion in Jupiter's magnetosphere, *J. Geophys. Res.*, *81*, 5215, 1976.

Barbosa, D. D. and F. V. Coroniti, Lossy radial diffusion of relativistic Jovian electrons, *J. Geophys. Res.*, *81*, 4553, 1976.

Barkas, W. H., *Nuclear Research Emulsions*, Academic Press, New York, 1963.

Berge, G. L. and S. Gulkis, Earth-based radio observations of Jupiter: Millimeter to meter wavelengths, in *Jupiter*, ed. by T. Gehrels, University of Arizona Press, 1976.

Bigg, E. K., Influence of the satellite Io on Jupiter's decametric emission, *Nature*, *203*, 1008, 1964.

Borovsky, J. E., C. K. Goertz, and G. Joyce, Magnetic pumping of particles in the outer Jovian magnetosphere, *J. Geophys. Res.*, *86*, 3481, 1981.

Broadfoot, A. L., M. J. S. Belton, P. Z. Takacs, B. R. Sandel, D. E. Shemansky, J. B. Holberg, J. M. Ajello, S. K. Atreya, T. M. Donahue, H. W. Moos, J. L. Bertaux, J. E. Blamont, D. F. Strobel, J. C. McConnell, A. Dalgarno, R. Goody, and M. B. McElroy, Extreme ultraviolet observations from Voyager 1 encounter with

Jupiter, *Science*, *204*, 979, 1979.

Broadfoot, A. L., B. R. Sandel, D. E. Shemansky, J. C. McConnell, G. R. Smith, J. B. Holberg, S. K. Atreya, T. M. Donahue, D. F. Strobel, and J. L. Bertaus, Overview of the Voyager ultraviolet spectrometry results through Jupiter encounter, *J. Geophys. Res.*, *86*, September, 1981.

Brown, R. A., Optical emission from Io, *IAU Symposium No. 65*, p. 527, 1974.

Burke, B. F. and K. L. Franklin, Observations of a variable radio source associated with the planet Jupiter, *J. Geophys. Res.*, *60*, 213, 1955.

Carbary, J. F., T. W. Hill, and A. J. Dessler, Planetary-spin-period acceleration of particles, *J. Geophys. Res.*, *81*, 5189, 1976.

Connerney, J. E. P., M. H. Acuña, and N. F. Ness, Modeling the Jovian current sheet and inner magnetosphere, *J. Geophys. Res.*, *86*, September, 1981.

Cook, A. F., III, and A. V. Jones, Aurora in Jupiter's Atmosphere?, preprint, 1981.

Cook, W. R., Elemental composition of solar energetic particles, Thesis, California Institute of Technology, 1980.

Coroniti, F. V., Denouement of Jovian radiation belt theory, *Space Sci. Rev.*, *17*, 837, 1975.

Drake, F. P. and H. Hvatum, Non-thermal microwave radiation from Jupiter, *Astron. J.*, *64*, 329, 1959.

Eviatar, A., Yu. Mekler, and F. V. Coroniti, Jovian sodium plasma, *Astrophys. J.*, *205*, 622, 1976.

Eviatar, A. and G. L. Siscoe, Limit on rotational energy available to excite Jovian

aurora, *Geophys. Res. Lett.*, *7*, 1085, 1980.

Field, G. B., The source of radiation from Jupiter at decimeter wavelengths, *J. Geophys. Res.*, *64*, 1169, 1959.

Fillius, R. W. and C. E. McIlwain, Measurements of the Jovian radiation belts, *J. Geophys. Res.*, *79*, 3589, 1974.

Fillius, W., C. McIlwain, A. Mogro-Campero, and G. Steinberg, Evidence that pitch angle scattering is an important loss mechanism for energetic electrons in the inner radiation belt of Jupiter, *Geophys. Res. Lett.*, *3*, 33, 1976.

Frank, L. A., K. L. Ackerson, J. H. Wolfe, and J. D. Mihalov, Observations of plasmas in the Jovian magnetosphere, *J. Geophys. Res.*, *81*, 457, 1976.

Froidevaux, L., Radial diffusion in Io's torus: Some implications from Voyager 1, *Geophys. Res. Lett.*, *7*, 33, 1980.

Garrard, T. L., MJS CRS science requirements document, Space Radiation Laboratory Technical Report 76-1, California Institute of Technology, 1976.

Gehrels, N., Calibrations of the Voyager Low Energy Telescopes' response to high counting rate, Space Radiation Laboratory Internal Report #80, California Institute of Technology, 1981.

Gehrels, N. and A. C. Cummings, CRS LET detector thickness, area and geometry factor measurements, Space Radiation Laboratory Internal Report #77, 1980.

Gehrels, N. and D. L. Chenette, A technique for determining particle anisotropies using the Voyager Low Energy Telescopes, Space Radiation Laboratory Internal Report #84, California Institute of Technology, 1981.

Gehrels, N., E. C. Stone, and J. H. Trainor, Energetic oxygen and sulfur in the Jovian magnetosphere, *J. Geophys. Res*, submitted, 1981.

Gehrels, T. (editor), *Jupiter*, University of Arizona press, Tucson, 1976.

Gloeckler, G., R. Sciambi, C. Y. Fan, and D. Hovestadt, Abundances, charge states, and energy spectra of helium and heavy ions during solar particle events, *Proc. 14th International Cosmic Ray Conf.*, *5*, 1576, 1975.

Goertz, C. K., Energization of charged particles in Jupiter's outer magnetosphere, *J. Geophys. Res.*, *83*, 3145, 1978.

Goertz, C. K., Proton aurora on Jupiter's nightside, *Geophys. Res. Lett.*, *7*, 365, 1980.

Goertz, C. K. and M. F. Thomsen, The Dynamics of the Jovian Magnetosphere, *Rev. Geophys. Space Phys.*, *17*, 731, 1979.

Goertz, C. K., J. A. Van Allen, and M. F. Thomsen, Further observational support for the lossy radial diffusion model of the inner Jovian magnetosphere, *J. Geophys. Res.*, *84*, 87, 1979.

Goldreich, P. and D. Lynden-Bell, Io, a Jovian unipolar inductor, *Astrophys. J.*, *156*, 59, 1969.

Gurnett, D. A., W. S. Kurth, and F. L. Scarf, Plasma wave observations near Jupiter: Initial results from Voyager 2, *Science*, *206*, 987, 1979.

Gurnett, D. A., F. L. Scarf, W. S. Kurth, R. R. Shaw, and R. L. Poynter, Determination of Jupiter's electron density profile from plasma wave observations, *J. Geophys. Res.*, *86*, September, 1981.

Hamilton, D. C., G. Gloeckler, S. M. Krimigis, and L. J. Lanzerotti, Composition of non-thermal ions in the Jovian magnetosphere, *J. Geophys. Res.*, *86*,

September, 1981.

Hill, T. W. and F. C. Michel, Heavy ions from the Galilean satellites and the centrifugal distortion of the Jovian magnetosphere, *J. Geophys. Res.*, *81*, 4561, 1976.

Intriligator, D. S. and W. D. Miller, Detection of the Io plasma torus by Pioneer 10, *Geophys. Res. Lett.*, *8*, 409, 1981.

Johnson, T. V., A. F. Cook II, C. Sagan, and L. A. Soderblom, Volcanic resurfacing rates and implications for volatiles on Io, *Nature*, *280*, 746, 1979.

Johnson, T. V., G. E. Morfill, and E. Grün, Dust in Jupiter's Magnetosphere: An Io Source?, *Geophys. Res. Lett.*, *7*, 305, 1980.

Kennel, C. F. and H. E. Petschek, Limit on stably trapped particle fluxes, *J. Geophys. Res.*, *71*, 1, 1966.

Kennel, C. F. and F. V. Coroniti, Jupiter's magnetosphere, *Ann. Rev. Astron. Astrophys.*, *15*, 389, 1977.

Koral, K. F. and A. J. Cohen, Empirical equations for electron backscattering coefficients, NASA report TN D-2909, 1965.

Krimigis, S. M., T. P. Armstrong, W. I. Axford, C. O. Bostrom, C. Y. Fan, G. Gloeckler, L. J. Lanzerotti, E. P. Keath, R. D. Zwickl, J. F. Carbary, and D. C. Hamilton, Low-energy charged particle environment at Jupiter: A first look, *Science*, *204*, 998, 1979.

Krimigis, S. M., J. F. Carbary, E. P. Keath, C. O. Bostrom, W. I. Axford, G. Gloeckler, L. J. Lanzerotti, and T. P. Armstrong, Characteristics of hot plasma in the Jovian magnetosphere: Results from the Voyager spacecraft, *J. Geophys.*

Res., *86*, September, 1981.

Kupo, I., Yu. Mekler, and A. Eviatar, Detection of ionized sulfur in the Jovian magnetosphere, *Astrophys. J. Lett.*, *205*, L51, 1976.

Lepping, R. P., L. F. Burlaga, and L. W. Klein, Jupiter's magnetopause, bow shock, and 10-hour modulated magnetosheath: Voyagers 1 and 2, NASA Report TM-82033, October 1980.

Lotz, W., Electron-impact ionization cross-sections and ionization rate coefficients for atoms and ions, *Astrophys. J. Supp.*, *14*, 207, 1967.

McIlwain, C. E. and R. W. Fillius, Differential spectra and phase space densities of trapped electrons at Jupiter, *J. Geophys. Res.*, *80*, 1341, 1975.

McNutt, R. L., Jr., J. W. Belcher, and H. S. Bridge, Positive ion observations in the middle magnetosphere of Jupiter, *J. Geophys. Res.*, *86*, September, 1981.

Moos, H. W. and J. T. Clarke, Ultraviolet observations of the Io torus from the IUE observatory, *Astrophys. J.*, *247*, 354, 1981.

Morfill, G. E., E. Grün, and T. V. Johnson, Dust in Jupiter's Magnetosphere: Effect on Magnetospheric Electrons and Ions, *Planet. Space Sci.*, *28*, 1115, 1980.

Ness, N. F., M. H. Acuña, R. P. Lepping, L. F. Burlaga, K. W. Behannon, and F. M. Neubauer, Magnetic field studies at Jupiter by Voyager 1: Preliminary results, *Science*, *204*, 982, 1979a.

Ness, N. F., M. H. Acuña, R. P. Lepping, L. F. Burlaga, K. W. Behannon, and F. M. Neubauer, Magnetic field studies at Jupiter by Voyager 2: Preliminary results, *Science*, *206*, 966, 1979b.

Northcliffe, L. C. and R. F. Schilling, Range and stopping-power tables for heavy

ions, *Nuclear Data Tables*, *A7*, 233, 1970.

Papadopoulos, K., J. D. Gaffey, Jr., and P. J. Palmadesso, Stochastic acceleration of large M/Q ions by hydrogen cyclotron waves in the magnetosphere, *Geophys. Res. Lett.*, *7*, 1014, 1980.

Pilcher, C. B. and D. F. Strobel, Emissions from neutrals and ions in the Jovian magnetosphere, preprint, 1981.

Povlis, J., Space Radiation Laboratory Technical Report 80-2, California Institute of Technology, 1980.

Richardson, J. D. and G. L. Siscoe, Factors governing the ratio of inward-to-outward diffusing flux of satellite ions, *Geophys. Res. Lett.*, submitted, 1981.

Richardson, J. D., G. L. Siscoe, F. Bagenal, and J. D. Sullivan, Time dependent plasma injection by Io, *Geophys. Res. Lett.*, *7*, 37, 1980.

Roederer, J. G., *Dynamics of Geomagnetically Trapped Radiation*, Springer, New York, 1970.

Sandel, B. R., D. E. Shemansky, A. L. Broadfoot, J. L. Bertaux, J. E. Blamont, M. J. S. Belton, J. M. Ajello, J. B. Holberg, S. K. Atreya, T. M. Donahue, H. W. Moos, D. F. Strobel, J. C. McConnell, A. Dalgarno, R. Goody, M. B. McElroy, and P. Z. Takacs, Extreme ultraviolet observations from Voyager 2 encounter with Jupiter, *Science*, *206*, 962, 1979.

Scarf, F. L., D. A. Gurnett, and W. S. Kurth, Jupiter plasma wave observations: An initial Voyager 1 overview, *Science*, *204*, 991, 1979.

Scarf, F. L., D. A. Gurnett, and W. S. Kurth, Measurements of plasma wave spectra in Jupiter's magnetosphere, *J. Geophys. Res.*, *86*, September, 1981.

Schardt, A. W., F. B. McDonald, and J. H. Trainor, Energetic particles in the pre-dawn magnetotail of Jupiter, *J. Geophys. Res.*, *86*, September, 1981.

Schulz, M., Jupiter's radiation belts, *Space Sci. Rev.*, *23*, 277, 1979.

Schulz, M. and L. J. Lanzerotti, *Particle Diffusion in the Radiation Belts*, Springer, New York, 1974.

Scudder, J. D., E. C. Sittler, Jr., and H. S. Bridge, Survey of the plasma electron environment of Jupiter: A view from Voyager, *J. Geophys. Res.*, *86*, September, 1981.

Sentman, D. D., J. A. Van Allen, and C. K. Goertz, Recirculation of energetic particles in Jupiter's magnetosphere, *Geophys. Res. Lett.*, *2*, 465, 1975.

Shemansky, D. E., Radiative cooling efficiencies and predicted spectra of species of the Io plasma torus, *Astrophys. J.*, *236*, 1043, 1980a.

Shemansky, D. E., Mass-loading and the diffusion-loss rates of the Io plasma torus, *Astrophys. J.*, *242*, 1266, 1980b.

Simpson, J. A., D. C. Hamilton, R. B. McKibben, A. Mogro-Campero, K. R. Pyle, and A. J. Tuzzolino, The protons and electrons trapped in the Jovian dipole magnetic field region and their interaction with Io, *J. Geophys. Res.*, *79*, 3522, 1974.

Simpson, J. A., D. C. Hamilton, G. A. Lentz, R. B. McKibben, M. Perkins, K. R. Pyle, A. J. Tuzzolino, and J. J. O'Gallagher, Jupiter revisited: First results from the University of Chicago charged particle experiment on Pioneer 11, *Science*, *188*, 455, 1975.

Siscoe, G. L. and D. Summers, Centrifugally driven diffusion of Iogenic plasma,

Geophys. Res. Lett., submitted, 1981.

Siscoe, G. L., A. Eviatar, R. M. Thorne, J. D. Richardson, F. Bagenal, and J. D. Sullivan, A dynamic coupling between the Io plasma formation and the ring current, *J. Geophys. Res.*, *86*, September, 1981.

Smith B. A., L. A. Soderblom, T. V. Johnson, A. P. Ingersoll, S. A. Collins, E. M. Shoemaker, G. E. Hunt, H. Masursky, M. H. Carr, M. E. Davies, A. F. Cook III, J. Boyce, G. E. Danielson, T. Owen, C. Sagan, R. F. Beebe, J. Veverka, R. G. Strom, J. F. McCauley, D. Morrison, G. A. Briggs, and V. E. Suomi, The Jupiter system through the eyes of Voyager 1, *Science*, *204*, 951, 1979.

Smith, E. J., L. Davis, Jr., D. E. Jones, P. J. Coleman, Jr., D. S. Colburn, P. Dyal, C. P. Sonett, and A. M. A. Frandsen, The planetary magnetic field and magnetosphere of Jupiter: Pioneer 10, *J. Geophys. Res.*, *79*, 3501, 1974.

Stilwell, D. E., W. D. Davis, R. M. Joyce, F. B. McDonald, J. H. Trainor, W. E. Althouse, A. C. Cummings, T. L. Garrard, E. C. Stone, and R. E. Vogt, The Voyager cosmic ray experiment, *IEEE Trans. on Nuclear Science*, *NS-26*, 513, 1979.

Stone, E. C., R. E. Vogt, F. B. McDonald, B. J. Teegarden, J. H. Trainor, J. R. Jokipii, and W. R. Webber, Cosmic ray investigation for the Voyager missions; Energetic particle studies in the outer heliosphere - and beyond, *Sp. Sci. Rev.*, *21*, 355, 1977.

Sullivan, J. D. and G. L. Siscoe, In situ observations of Io torus plasma, in *The Satellites of Jupiter*, ed. by D. Morrison, University of Arizona Press, 1981.

Thomsen, M. F., Jovian magnetosphere-satellite interactions: Aspects of energetic charged particle loss, *Rev. Geophys. Space Phys.*, *17*, 369, 1979.

Thomsen, M. F., C. K. Goertz, and J. A. Van Allen, A determination of the L

dependence of the radial diffusion coefficient for protons in Jupiter's inner magnetosphere, *J. Geophys. Res.*, *82*, 3655, 1977.

Thorne, R. M., Jovian auroral secondary electrons and their influence on the Io plasma torus, *Geophys. Res. Lett.*, *8*, 509, 1981.

Thorne, R. M. and B. T. Tsurutani, Diffuse Jovian aurora influenced by plasma injection from Io, *Geophys. Res. Lett.*, *6*, 649, 1979.

Trainor, J. H., F. B. McDonald, B. J. Teegarden, W. R. Webber, and E. C. Roelof, Energetic particles in the Jovian magnetosphere, *J. Geophys. Res.*, *79*, 3600, 1974.

Van Allen, J. A., D. N. Baker, B. A. Randall, and D. D. Sentman, The magnetosphere of Jupiter as observed with Pioneer 10, 1. Instrument and principal findings, *J. Geophys. Res.*, *79*, 3559, 1974.

Vogt, R. E., W. R. Cook, A. C. Cummings, T. L. Garrard, N. Gehrels, E. C. Stone, J. H. Trainor, A. W. Schardt, T. Conlon, N. Lal, and F. B. McDonald, Voyager 1: Energetic ions and electrons in the Jovian magnetosphere, *Science*, *204*, 1003, 1979a.

Vogt, R. E., A. C. Cummings, T. L. Garrard, N. Gehrels, E. C. Stone, J. H. Trainor, A. W. Schardt, T. F. Conlon, and F. B. McDonald, Voyager 2: Energetic ions and electrons in the Jovian magnetosphere, *Science*, *206*, 984, 1979b.

Warwick, J. W., J. B. Pearce, A. C. Riddle, J. K. Alexander, M. D. Desch, M. L. Kaiser, J. R. Thieman, T. D. Carr, S. Gulkis, A. Boischot, C. C. Harvey, and B. M. Pedersen, Voyager 1 planetary radio astronomy observations near Jupiter, *Science*, *204*, 995, 1979.

Zmuidzinas, J., The maximum smoothness method of spectrum reconstruction,

Space Radiation Laboratory Internal Report #85, California Institute of Technology, 1981.